POLITECNICO DI MILANO

School of Civil, Environmental and Land Planning Engineering

Master’s Degree Course in Environmental and Land Planning Engineering

ASSESSMENT OF AN ADVANCED OXIDATION PROCESS REACTOR WITH UV/H_2O_2 FOR THE REMOVAL OF CONTAMINANTS OF EMERGING CONCERN

Supervisor
Prof. Andrea Turolla

Master’s Degree Thesis of

Sabrina Belén Ramírez

885098

Academic year
2022

ACKNOWLEDGMENTS

First of all, I would like to express my deepest and most sincere gratitude to my supervisor, Prof. Andrea Turolla. These past years have been particularly challenging and full of ups and downs, but his support, encouragement and patience have helped me pull through. Words cannot begin to describe how grateful I am for his dedication, guidance, hard work and for not giving up on me, in spite all the difficulties. I am very thankful for the vastly knowledge he shared with me and he will always have my deepest admiration.

I would like to thank Prof. Manuela Antonelli for being an incredible inspiration and example and for letting me be a part of this project. I aspire to become as knowledgeable and wise one day. I appreciate all her advice and consideration throughout my journey at Politecnico di Milano.

I am also thankful for the Double Degree program at Politecnico di Milano for the opportunity to fulfill a longtime dream of studying abroad. An additional thanks to the Catalan Institute for Water Research for their contributions to data collection.

I would also like to thank Dr. Adriana Rohr for the constant support and counseling. I am very lucky to have her in my life as my physician, mentor and, most importantly, my friend.

To my dearest friend Cris, with whom I spent countless hours studying together at the library. Although far away, having her in my life has been a blessing and I will forever cherish every moment spent together.

I also would like to thank my longtime friend João, whose friendship and advice have been crucial throughout these difficult years.

A special thanks to Rafa, for always finding ways to uplift me and whose constant support and belief in me are the reason I am still standing.

Finally, my biggest thanks to my family for all the unconditional support and love. I thank Lia, Mandy and Miel for inspiring me every day to become a better person. To my parents for the financial and emotional support. I am forever thankful for always being there for me, no matter the distance or the time difference. Everything I am I owe it to you and I would not have been able to do this without you.

ABSTRACT

The preservation of water quality has become a priority due to the exponential increase of the population and the contamination caused by human activities. Improvements in the detection techniques of contaminants brought the attention to a new class of organic compounds, denominated emerging organic contaminants (EOCs), that have been proven to be harmful for humans and aquatic organisms. New technologies for the removal of these contaminants have emerged, such as Advanced Oxidation Processes (AOPs). In particular, UV/H_2O_2 AOP is capable of achieving the degradation of EOCs by generating hydroxyl radicals (OH•) from the UV photolysis of H_2O_2. In this research, the performance of a pilot-scale UV/H_2O_2 advanced oxidation reactor was evaluated with the use of Computation Fluid Dynamics (CFD) for the removal of EOCs present in wastewater and the influence of operating conditions, including the type of water matrix, on the performance of the reactor was assessed. The procedure for CFD modelling consisted of (i) reproducing reactor geometry and meshing, (ii) developing three sub-models for involved multi-physical phenomena, namely fluid dynamics, radiation transfer, and reaction kinetics. The modelling allowed to determine EOC concentrations at the outlet of the reactor operating at steady state. Fluid dynamics modelling results successfully reproduced experimental tracer test under various flowrate conditions. Radiation transfer simulations proved the strong influence of water matrix and reactor optical properties on the radiation distribution. Such effect was observed for UV dose distribution results, showing that particles entering water matrices with lower absorbance received higher UV dose than those in water matrices with higher absorbance. Lastly, kinetic modelling proved good applicability in the prediction of chemical degradation and the increase of reactor performance when H_2O_2 is added. Results also pointed to the negative influence of water absorbance as well as the presence of light absorbing species. Future investigations could be performed on the influence of the flow rates to degradation.

Keywords: Wastewater Treatment; Wastewater Reuse; Advanced Oxidation Processes; UV/H_2O_2; Emerging Contaminants, Computational Fluid Dynamics.

ABSTRACT

La conservazione della qualità dell'acqua è diventata una priorità a causa dell'aumento esponenziale della popolazione e della contaminazione causata dalle attività umane. I miglioramenti nelle tecniche di rilevamento dei contaminanti hanno portato l'attenzione su una nuova classe di composti organici, denominati contaminanti organici emergenti (EOC), che si sono rivelati dannosi per l'uomo e gli organismi acquatici. Sono emerse nuove tecnologie per la rimozione di questi contaminanti, come i processi di ossidazione avanzata (AOP). In particolare, UV/H_2O_2 AOP è in grado di ottenere la degradazione degli EOC generando radicali idrossilici (OH•) dalla fotolisi UV dell'H_2O_2. In questa ricerca sono state valutate le prestazioni di un reattore ad ossidazione avanzata UV/H_2O_2 su scala pilota con l'uso della Computation Fluid Dynamics (CFD) per la rimozione delle EOC presenti nelle acque reflue e l'influenza delle condizioni operative, compreso il tipo di matrice acquosa, è stata valutata la prestazione del reattore. La procedura per la modellazione CFD consisteva in (i) riprodurre la geometria e il meshing del reattore, (ii) sviluppare tre sottomodelli per i fenomeni multifisici coinvolti, vale a dire fluidodinamica, trasferimento di radiazioni e cinetica di reazione. La modellizzazione ha permesso di determinare le concentrazioni di EOC all'uscita del reattore funzionante a regime. I risultati della modellazione fluidodinamica hanno riprodotto con successo il test sperimentale del tracciante in varie condizioni di portata. Le simulazioni di trasferimento di radiazioni hanno dimostrato la forte influenza della matrice d'acqua e delle proprietà ottiche del reattore sulla distribuzione della radiazione. Tale effetto è stato osservato per i risultati della distribuzione della dose UV, mostrando che le particelle che entrano in matrici d'acqua con un'assorbanza inferiore hanno ricevuto una dose UV più elevata rispetto a quelle nelle matrici d'acqua con un'assorbanza più elevata. Infine, la modellazione cinetica ha dimostrato una buona applicabilità nella previsione della degradazione chimica e nell'aumento delle prestazioni del reattore quando viene aggiunta H2O2. I risultati hanno anche evidenziato l'influenza negativa dell'assorbimento d'acqua e la presenza di specie che assorbono la luce. Indagini future potrebbero essere eseguite sull'influenza delle portate sul degrado.

Parole chiave: Trattamento delle acque reflue; Riutilizzo delle acque reflue; Processi di ossidazione avanzata; UV/H_2O_2; Contaminanti emergenti, Computational Fluid Dynamics.

LIST OF FIGURES

LIST OF TABLES

TABLE OF CONTENTS

1
INTRODUCTION

The availability of high-quality water has been a primordial necessity for the human development since the very beginning. The exponential increase of the population and the contamination of water as a result of the diffusion of intensive agriculture and industrial practices, among others, resulted in the preservation of water quality becoming a priority. Not only water for drinking purposes, but around the twentieth century, attention had also turned to discarded waters. By the 1970s the concern with the presence of contaminants with chronic health impacts increased the complexity of the water treatments (Crittenden, 2012).

Improvements in the detection techniques of contaminants brought the attention of water professionals to a new class of organic compounds. They were denominated emerging organic contaminants (EOCs) and consist of pharmaceuticals, endocrine disruptors, personal care products, pesticides and surfactants, among others. EOCs are mainly produced by wastewater from domestic origin, hospital effluents and chemical manufacturing plants, and from the runoff of livestock and agriculture sites (Pal et al., 2010). Researchers have been able to relate health risks, on both humans and aquatic organisms, with the presence of EOCs. In addition, these compounds were found to be widely occurring in the aquatic environment making it urgent to further study their fate, toxicity, and treatment methods.

In recent years, Advanced Oxidation Processes (AOPs) became relevant as a solution to the wastewaters threatened by the increasing presence of EOCs. Specifically, technologies driven by UV have gained more popularity due to the decreasing prices on lamps and the continuous research on increasing the life of the lamp (Antonelli, 2015). AOPs rely on the generation of the hydroxyl radical (OH•), allowing for the oxidization of the contaminant of concern. Moreover, AOPs are capable of achieving disinfection and favor the removal of natural organic matter (NOM). These technologies have become a full-scale solution due to their capacity to generate hydroxyl radicals at ambient temperature and atmospheric pressure, which is not the case for others, such as the catalytic oxidation process (Glaze et al., 1987).

One of the consolidated AOPs technologies consists on combining the use of ultraviolet radiation, in particular UV-C, with the injection of hydrogen peroxide (H_2O_2) in what is known as the UV/H_2O_2 process. The hydroxyl radicals, that are responsible for the degradation of EOCs, are directly produced from the UV photolysis of H_2O_2. With the increasing presence of EOCs in wastewater, it became clear that new methodologies needed to be developed for the prediction of performance of these technologies, since evaluating the degradation of each new contaminant can be resource consuming. Mathematical models to facilitate the design and optimization of the process have been developed. However, there are still some major limitations that restrict the implementations of UV-driven AOPs. According to Montecchio (2018), the two major restrains are the lower performance in comparison with traditional technologies and the difficulty of taking results in a consistent way from lab to full-scale.

Computational fluid dynamic (CFD) has been established as a promising numerical method for solving fluid hydrodynamics. It is possible to achieve high resolution predictions of performance of the UV/H_2O_2 technology integrating CFD with kinetic equations, UV fluence rate and dose models. In this way, the methodology is capable of solving scale-up difficulties and reducing costs and time consumptions (Santoro et. al 2010; Wols et. al 2015).

The overall scope of this work was to evaluate the performance of a UV/H_2O_2 advanced oxidation reactor for the removal of EOCs present in wastewater and the influence of the operating conditions, including the type of water matrix, on the performance of the reactor. The approach used in this thesis work consisted of applying CFD modeling to reproduce the behavior of a pilot-scale UV/H_2O_2 reactor. The computational modeling was developed by improving state-of-the-art procedures reported in literature and it was validated using experimental data from a campaign performed on three different wastewater matrices.

The specific objectives were (i) to simulate the radiation transfer and fluid dynamics in the pilot-scale UV/H_2O_2 reactor, (ii) to analyze the influence of the different operating conditions on radiation transfer and fluid dynamics, (iii) to develop a tank-in-series conceptual model describing the fluid dynamics in the reactor and compare it to the computational one, (iv) to evaluate the UV dose distribution of radiation in the reactor for the different types of water matrices, and (v) to develop a kinetic model capable of predicting the final concentration of the different contaminants as a function of the UV dose.

2
LITERATURE REVIEW

2.1
UV/H_2O_2 Advanced Oxidation Process

Oxidation processes are used in water and wastewater treatment when dealing with the removal of organic and inorganic contaminants. Usually, the organic species are oxidized into less harmful compounds and the inorganic ones are converted into to insoluble forms for removal by precipitation. AOPs are a specific type of oxidation process that employ radicals, in particular hydroxyl radicals (OH•), as highly reactive agents to promote water and wastewater treatment by degrading toxic organic compounds and odorous species, removing color, and reducing natural organic matter and precursors of disinfection by-products (Crittenden et at., 2012).

In radical-based AOPs the hydroxyl radicals are generated at ambient temperature and atmospheric pressure. These radicals are highly reactive electrophiles that rapidly react, almost non-selectively, with organic compounds with rate constants in the order of magnitude of 10^8 to 10^{10} $M^{-1}s^{-1}$ (Buxton et al. 1988). This capacity makes AOPs a viable and competitive technology against conventional oxidants, like chlorine, that act with higher selectivity towards target contaminants. According to the UV/Oxidation handbook (1994), the OH• radicals interact with the organic pollutants by: undergoing addition reactions with double bonds, extracting hydrogen atoms, transferring electrons, and radical combination.

Over the years, although AOPs have expanded considerably, few technologies became commercially available for full-scale applications, these are: ozone (O_3) and hydrogen peroxide (H_2O_2), UV light and ozone, UV light and hydrogen peroxide, UV light and titanium dioxide (TiO_2), and combinations of these. The present work focuses on the UV/H_2O_2 AOP.

The overall scheme of a UV/H_2O_2 AOP usually consists in the H_2O_2 injection and mixing in wastewater undergoing treatment followed by the irradiation in a stainless-steel reactor equipped with mercury lamps at low or medium pressure (Figure 2.1). This technology benefits from the stability of the H_2O_2 and its capacity to be stored for long periods.

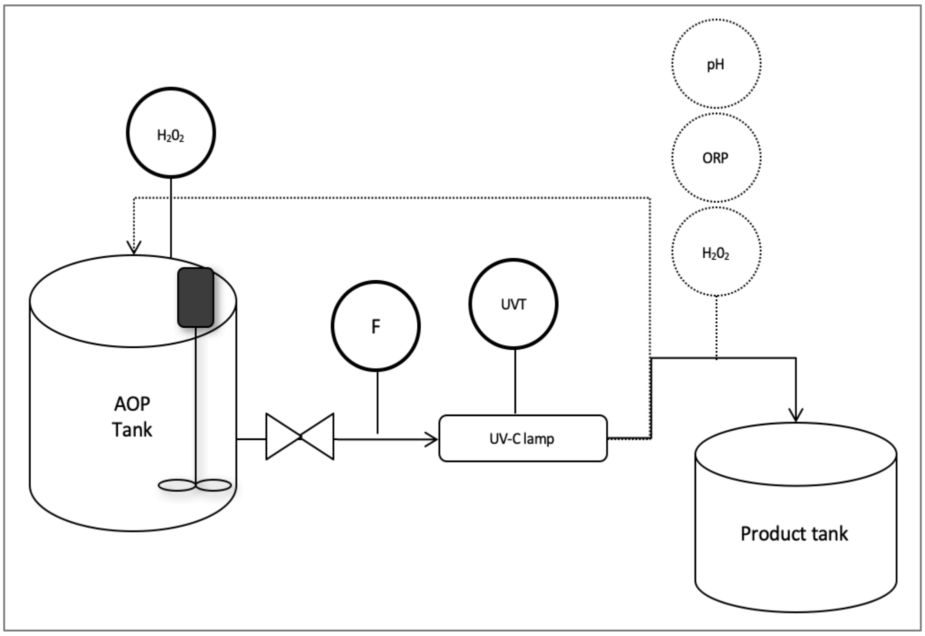

Figure 2.1: Diagram representative of a simplified UV/H_2O_2 AOP system. From left to right: H_2O_2 and wastewater mixing tank, throttling valve, UV-C photoreactor, and product tank. Measurements of H_2O_2 concentration, flow rate (F), UV water transmittance (UVT), pH and oxidation-reduction potential (ORP) are also indicated.

The decision on the number of lamps and their configuration relies on the application purpose. Researchers have studied the different combinations in an attempt to better understand the parameters affecting the efficiency of reactors. For instance, Mohajerani et al. (2010) modeled the degradation of metronidazole in two UV/H_2O_2 units, one with a single lamp and another one with a multi-lamp configuration, in distilled water as well as in alkaline water. The study showed the highest performance of multi-lamp configuration, since metronidazole degradation rate was approximately 5 times greater.

Moreover, lamp configuration inside reactors can be designed according to two main approaches: cross-flow or parallel, also known as annular configuration (Figure 2.2). A research carried out by Santoro et al. (2010) studied the degradation of tributyl phosphate (TBP) and tri(2chloroethtyl) phosphate (TCEP) in one parallel and one cross-flow UV/H_2O_2 reactors using CFD. The study was performed for both turbulent and laminar flow regimes and showcased the OH• radical distributions in the photoreactors. Modelling results confirmed that the annular reactor provided a better oxidation performance than the cross-flow configuration. According to the authors, this is due to the presence of recirculation zones in the cross-flow reactor caused by the accelerating flow near the quartz sleeve.

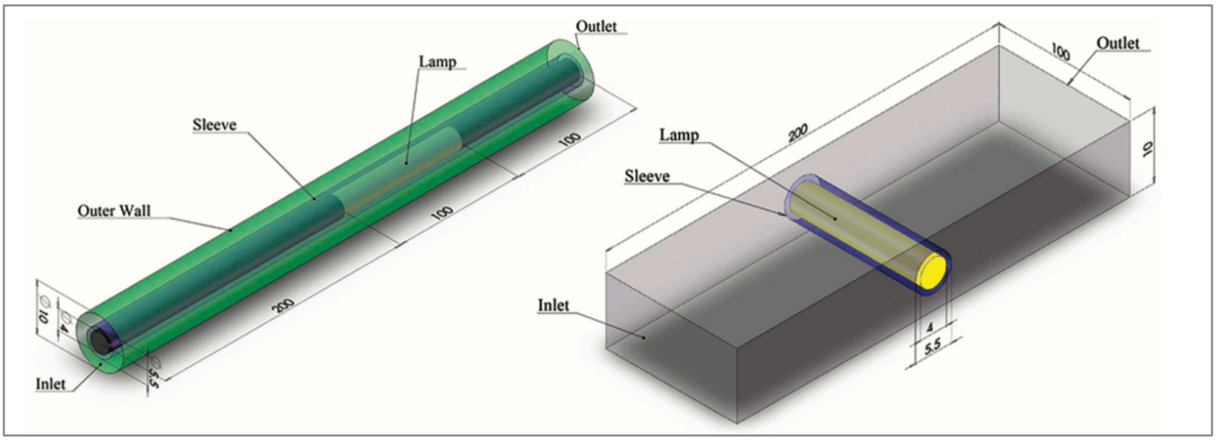

Figure 2.2: Examples of annular (left) and cross-flow (right) configurations of UV/H_2O_2 reactors. Dimensions are given in centimeters. Source: Santoro et al. (2010).

The UV/H_2O_2 AOP relies on the photolysis of H_2O_2 to directly generate OH•, as shown in the stoichiometric equation below, to oxidize the organic substances of concern. The non-uniform radiation distribution, also known as local UV-fluence rate, alongside the concentration of the species and the kinetic rate constants, will determine the local reaction rate.

$$H_2O_2 + hv \rightarrow 2OH \bullet \qquad (1)$$

The elementary reactions of H_2O_2 photolysis (Table 2.1) have already been investigated by several researchers and have been determined to be a series of chain reactions following an initiation (equation 1), a propagation (equations 2 to 5) and a termination (equations 6 to 10). Moreover, the following mechanisms must be taken into consideration: the oxidation of the target organic compound, the scavenging of OH• radicals by NOM, bicarbonate and carbonate, and the UV absorption by background components in the water matrix.

Table 2.1: Elementary reactions of the UV/H_2O_2 process with respective rate constants (K_i).

Reaction	Rate Constant 25˚C, M^{-1} s^{-1}	Reference
(2) $HO \bullet + HO_2^- \rightarrow OH^- + HO_2 \bullet$	$K_2 = 7.5 \times 10^9$	(Christensen et al.,1982)
(3) $HO \bullet + H_2O_2 \rightarrow H_2O + HO_2 \bullet$	$K_3 = 2.7 \times 10^7$	(Buxton et al., 1988)
(4) $H_2O_2 + HO_2 \bullet \rightarrow HO \bullet + O_2 + H_2O$	$K_4 = 3$	(Koppenol et al.,1978)
(5) $H_2O_2 + O_2 \bullet \rightarrow HO \bullet + O_2 + OH^-$	$K_5 = 0.13$	(Weinstein e Bielski,1979)
(6) $HO \bullet + HO \bullet \rightarrow H_2O_2$	$K_6 = 5.5 \times 10^9$	(Buxton et al., 1988)
(7) $HO \bullet + O_2 \bullet \rightarrow O_2 + OH^-$	$K_7 = 7 \times 10^9$	(Beck et al., 1969)

(8) $HO\bullet + HO_2\bullet \rightarrow O_2 + H_2O$	$K_8 = 6.6\times10^9$	(Sehested et al., 1968)
(9) $HO_2\bullet + HO_2\bullet \rightarrow O_2 + H_2O_2$	$K_9 = 8.3\times10^5$	(Bielski et al., 1985)
(10) $HO_2\bullet + O_2\bullet \rightarrow O_2 + HO_2^-$	$K_{10} = 6.6\times10^9$	(Bielski et al., 1985)

The fluid dynamics in the UV reactor is crucial for understanding the flow and concentration distribution of the different components present in the water through the reactor.

Several other factors affect the performance of this technology among which: the intensity of the lamp, the UV transmittance of the water matrix and the lamp configuration (Antonelli, 2015). One of the main disadvantages of this process is related to the poor absorption characteristics of H_2O_2. The molar absorptivity of hydrogen peroxide at 254 nm is around 20 $M^{-1}cm^{-1}$ resulting in 0.09 OH• formed per incident photon (Glaze et al., 1987). This can result in most of the radiation emitted by the lamp being wasted if the water matrix has low transmittance. Therefore, to produce the sufficient amount of OH• necessary for a successful oxidation a high concentration of H_2O_2 is required, representing a significant operational cost.

Another factor that must be taken into consideration is that a special reactor is required for this technology and, even though UV light does not generate byproducts, a significant residual H_2O_2 concentration remains in the effluent. Crittenden (2012) explains that high effluent concentrations of H_2O_2 are unavoidable and not only represent a health hazard but they also consume residual chlorine, thus possibly interfering with the disinfection processes.

2.2
Influence of water matrices

The UV/H_2O_2 process is critically affected by the physical and chemical properties of the water matrix. This section briefly discusses the properties considered by Crittenden (2012) to be of major impact on the overall AOPs.

One of the most relevant parameters is the absorbance of the matrix, since it determines the amount of light absorbed by the dissolved and suspended compounds in the water at a specified wavelength and thus, giving an indication of the remaining amount of light that will be available for the production of OH• radicals. The higher the absorbance of a water matrix, the lower the UV absorbed by H_2O_2 and, therefore, the lower the OH• generation. As stated by the Beer-Lambert law, the absorbance is proportional to the concentration of the light-absorbing molecules and the path length of the light thought the water. It is measured using a spectrophotometer with a path length of 1.0 cm and normally at 254 nm.

Another parameter of importance is the presence of OH• radical scavengers. These are a series of inorganic substances and organic matter that consume large amounts of OH• radicals reducing the oxidation efficiency of the UV/H_2O_2 system. Carbonate species, carbonate (CO_3^{2-}) and bicarbonate (HCO_3^-) are scavengers of OH• radicals that are capable of reducing the reaction rate significantly. In water matrices, the carbonate and bicarbonate concentrations are usually very high in comparison to that of the target pollutants, meaning that even low alkalinities will result in a drastic reduction of the degradation rates.

Moreover, Crittenden (2012) explains that at high pH the effect of the alkalinity becomes even worse as the second-order rate constant of OH• radicals with carbonate is much higher with respect to bicarbonate. Mohajerani et al. (2010) modeled the degradation of metronidazole in two UV/H_2O_2 units, single lamp and multi-lamp configurations, in distilled water as well as in alkaline waters. The interference of alkalinity resulted in an efficiency reduction because the alkalinity scavenges OH• radicals. In practice, this means that the higher the alkalinity concentrations the higher the required H_2O_2 dosage. Therefore, it becomes apparent the possible advantage coming from a pre-treatment to remove the alkalinity, such as softening.

The pH affects the concentration of the carbonate species, as explained in the paragraph above, as well as that of hydroperoxyl ions (HO_2^-). This can be an advantage when dealing with water matrices with high absorptivity because HO_2^- has a higher molar absorptivity than H_2O_2 at 254 nm (Crittenden, 2012). For these kinds of matrices, then, increasing the pH to favor the formation of HO_2^- will increase the efficiency of the process. Finally, pH affects the charge on the organic compounds present in the water.

NOM reacts with OH• radicals resulting in the quenching of the reaction using the radicals required for the oxidation of the pollutant of concern. Furthermore, Li et. al (2008) explained that NOM interferes with the absorption of UV light by H_2O_2 by acting as a UV light blocker preventing the formation of the OH• radicals. In their research, it was possible to prove that a dedicated NOM pre-treatment unit is essential to the performance of AOP systems, as it significantly reduces the number of reactors required.

In 2010, Alpert et al. evaluated the performance of CFD models for the degradation of methylene blue in a UV/H_2O_2 reactor. The study combined turbulence and fluence rate models with kinetic rate equations and examined the impact of different turbulence and fluence rate sub-models on CFD results. Overall, the CFD results tended to under predict the removal percentage of the indicator and the gap between results increased with increasing flow rates. Furthermore, the study indicated dissolved organic carbon (DOC) as a hydroxyl radical scavenger.

Reduced metal ions, such as iron and manganese, are also responsible for a significant consumption of the oxidant and scavenge OH• radicals.

Finally, for OH• radical-based AOPs an increase in temperature speeds up the reaction rates. A study carried out by Wols et al. (2015) simulated the degradation of pharmaceuticals in a UV/H_2O_2 reactor using CFD. A total of 35 pharmaceuticals were studied and the results showed that CFD was able to provide a good prediction for most of the compounds. Furthermore, the degradation of these pollutants displayed a dependency on temperature, showing the importance of this parameter for full-scale installations that will operate at different temperatures over the year.

2.3
CFD modeling

Research in recent years - such as the extensive work carried out by Elyasi and Taghipour (2010), Alpert et al. (2011), Ho et al. (2011), Casado et al. (2017) - has proven CFD to be a useful tool for the accurate prediction of the performance of UV disinfection and AOP reactors and has the potential to become a stand-alone validation method in the designing and implementation of these types of systems.

With the use of CFD it is possible to simulate the fluid dynamics inside the reactor and the pipes (transport and mixing), as well as the UV intensity distribution and the chemical kinetics. A typical procedure for CFD modeling, therefore, consists of creating a mesh of the photoreactor to be imported in the software, and performing a rigorous description of the mass and momentum conservation, radiant energy conservation and the species mass conservation. A schematic representation of the main passages in CFD modeling can be seen in Figure 2.3. Several software for performing CFD modeling are commercially available, such as ANSYS FLUENT, which is well-known for this type of application.

In the following sections, an overview of the theoretical models for hydrodynamics, radiation conservation and kinetic of the species that are behind the CFD simulation of a UV photoreactor for AOP processes are presented, as well as a brief discussion of the recent advancements in the field.

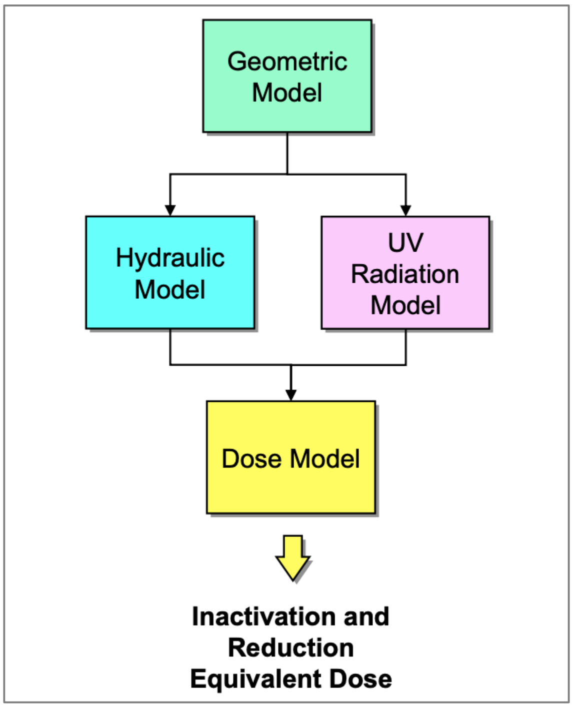

Figure 2.3: Overall scheme of a UV/H_2O_2 procedure for CFD modeling. Source: Ho (2009).

2.3.1
Fluid dynamics

The flow of incompressible fluids is described by the Navier-Stokes equations, a set of partial differential equations that consists of a continuity equation for the conservation of mass, the momentum conservation and the energy conservation equation. These equations describe the relationship between the velocity (u), pressure (p), temperature (t) and density (ρ) of a fluid in motion. The latter equation is solved only in particular cases, such as for fluids characterized by convective flows. When simulating the hydrodynamics of a UV photoreactor, the velocity field can be determined by solving the mass and momentum conservation equations, whose general forms expressed in tensor notation are shown below.

$$\frac{\partial u_i}{\partial x_i} = 0 \tag{11}$$

$$\rho\left(\frac{\partial u_i}{\partial t} + u_j\frac{\partial u_i}{\partial x_j}\right) = -\frac{\partial p}{\partial x_i} + \frac{\partial}{\partial x_j}\left(\mu\frac{\partial u_i}{\partial x_j}\right) \tag{12}$$

where μ is the molecular viscosity.

For a turbulent regime, these equations can be solved using the following methods: the Reynolds averaged Navier-Stokes (RANS) based models; Large Eddy Simulation (LES) model; Detached Eddy Simulation (DES); and the Direct Numerical Simulation (DNS). All of these models are available in ANSYS FLUENT except for DNS. In practice, the RANS model is the most widely used approach since both the DES and LES models require larger amounts of computational resources and efforts.

RANS method consists of defining any variable that is a function of time and space as the sum of a mean ($\bar{u}$) and a fluctuating (u') component. By definition, the average of the fluctuating component is zero. Therefore, expressing the Navier-Stokes equations 11 and 12 in Reynolds time-average results in the following equations.

$$\frac{\partial \bar{u}_i}{\partial x_i} = 0 \tag{13}$$

$$\rho\left(\frac{\partial \bar{u}_i}{\partial t} + \bar{u}_k \frac{\partial \bar{u}_i}{\partial x_k}\right) = -\frac{\partial \bar{p}}{\partial x_i} + \frac{\partial}{\partial x_j}\left(\mu \frac{\partial \bar{u}_i}{\partial x_j}\right) + \frac{\partial \tau_{ij}}{\partial x_j} \tag{14}$$

where $\tau_{ij} = -\rho \bar{u}_i \bar{u}_j$ is the Reynolds stress tensor.

As described by the manual on modeling turbulent flows in FLUENT (ANSYS FLUENT, 2013), the Reynolds stresses, introduced by the averaging method, are unknowns that must be modeled resulting in a closure problem. Modern models that give closure to the equations are divided into Eddy Viscosity Models, that are based on the Boussinesq hypothesis, or Reynolds-Stress Models (RSM), that require transport equations for Reynolds stresses thus resulting in a more complex and difficult to converge model.

Boussinesq (1877) introduced the concept of eddy viscosity (μ_T), also called turbulent viscosity, that assumes that the turbulent stresses are proportional to the gradient of the mean velocity field. In this way, using an analogy to the kinetic theory, turbulent eddies are carriers of thermal energy and momentum. Reynolds stresses are, therefore, modeled using the concept of eddy viscosity in a similar way that molecular viscosity is used for molecular stresses. For a general flow, the eddy viscosity model is presented in equation 15.

$$\tau_{ij} = -\rho \bar{u}_i \bar{u}_j = \mu_T\left(\frac{\partial \bar{u}_i}{\partial x_j} + \frac{\partial \bar{u}_j}{\partial x_i}\right) - \frac{2}{3}\mu_T \frac{\partial \bar{u}_k}{\partial x_k}\delta_{ij} - \frac{2}{3}\rho k \delta_{ij} \tag{15}$$

where k is the turbulent kinetic energy.

This approach was further elaborated by other researchers in later years and resulted in the development of one-equation (Spalart-Allmaras) and two-equation (*k*-ε and *k*-ω) turbulence models, each one computing the turbulent viscosity differently. The most commonly used in CFD for engineering applications are the k-ε models that can be Standard (SKE), Renormalization group (RNG) and Realizable (RKE). These models consider the turbulent flow to be determined by the turbulence kinetic energy, the mean velocity and the dissipation rate (ε). For the Standard k-ε turbulence model the turbulent viscosity is related to k and ε (equation 18), which are solved using transport equations and result in the k-equation (16) and ε-equation (17) (Celik, 1999).

$$\rho\frac{\partial k}{\partial t}+\rho\bar{u}_j\frac{\partial k}{\partial x_j}=\frac{\partial}{\partial x_j}\left(\left(\mu+\frac{\mu_T}{\sigma_k}\right)\frac{\partial k}{\partial x_j}\right)+\tau_{ij}\frac{\partial\bar{u}_i}{\partial x_j}-\rho\varepsilon \tag{16}$$

$$\rho\frac{\partial \varepsilon}{\partial t}+\rho\bar{u}_j\frac{\partial \varepsilon}{\partial x_j}=\frac{\partial}{\partial x_j}\left(\left(\mu+\frac{\mu_T}{\sigma_\varepsilon}\right)\frac{\partial \varepsilon}{\partial x_j}\right)+C_{\varepsilon 1}\frac{\varepsilon}{k}\tau_{ij}\frac{\partial\bar{u}_i}{\partial x_j}-C_{\varepsilon 2}\rho\frac{\varepsilon^2}{k} \tag{17}$$

$$\mu_T=\frac{\rho C_\mu k^2}{\varepsilon} \tag{18}$$

where $\sigma_k = 1$ and $\sigma_\varepsilon = 1.3$ correspond to the turbulent Prandtl number for k and ε, respectively; and $C_{\varepsilon 1} = 1.44$, $C_{\varepsilon 2} = 1.92$ and $C_\mu = 0.09$ to the closure coefficients (Rodi, 1993).

Major differences in the models are the method for determining the turbulent viscosity, the turbulent Prandtl numbers, and the generation of dissipation and destruction rate of the dissipation - caused by interactions between the mean flow and the products of the turbulent fluctuations (Celik, 1999) - in the ε-equation, which are not discusses in the present work.

When choosing a turbulence model to be applied in CFD, several factors must be taken into consideration: the flow physics, the established practice by the scientific community for a specific problem, the accuracy required, and the available computational and time resources. Thus, it is very important to know the possibilities and the limitations of the different models. In detail, the RKE model is better at predicting flows with rotation, boundary layers undergoing strong adverse pressure gradients, separation and recirculation, as well as providing more accurate predictions of the spreading rate of planar and round jets. It diverges from the SKE in two of the previously mentioned aspects: it presents a different formulation for the turbulent viscosity; and a different transport equation for the dissipation rate. The turbulent viscosity is given by equation 18, however, C_μ is no longer constant and it is given by the expression below.

$$C_\mu=\frac{1}{A_0+A_s\frac{kU^*}{\varepsilon}} \tag{19}$$

where $A_0 = 4.04$, $A_s = \sqrt{6}cos\phi$ with

$$\phi = \frac{1}{3}cos^{-1}\left(\sqrt{6}W\right);\; W = \frac{S_{ij}S_{jk}S_{ki}}{\tilde{S}^3};\; \tilde{S} = \sqrt{S_{ij}S_{ij}};\; S_{ij} = \frac{1}{2}\left(\frac{\partial u_j}{\partial x_i} + \frac{\partial u_i}{\partial x_j}\right);\; U^* = \sqrt{S_{ij}S_{ij} + \tilde{\Omega}_{ij}\tilde{\Omega}_{ij}}$$

with $\tilde{\Omega}_{ij} = \Omega_{ij} - 2\varepsilon_{ijk}\omega_k$ and $\Omega_{ij} = \overline{\Omega}_{ij} - \varepsilon_{ijk}\omega_k$, where $\overline{\Omega}_{ij}$ is the mean rate of rotation tensor viewed in a rotating reference frame with angular velocity, ω_k.

The transport equations for k (16) and ε (17) for the RKE model are shown next.

$$\rho\frac{\partial k}{\partial t} + \rho u_j\frac{\partial k}{\partial x_j} = \frac{\partial}{\partial x_j}\left(\left(\mu + \frac{\mu_T}{\sigma_k}\right)\frac{\partial k}{\partial x_j}\right) + G_k + G_b - \rho\varepsilon - Y_M + S_k \tag{20}$$

$$\rho\frac{\partial \varepsilon}{\partial t} + \rho u_j\frac{\partial \varepsilon}{\partial x_j} = \frac{\partial}{\partial x_j}\left(\left(\mu + \frac{\mu_T}{\sigma_\varepsilon}\right)\frac{\partial \varepsilon}{\partial x_j}\right) + \rho C_1 S_\varepsilon - \rho C_2\frac{\varepsilon^2}{k + \sqrt{\nu\varepsilon}} + C_{\varepsilon 1}\frac{\varepsilon}{k}C_{\varepsilon 3}G_b + S_\varepsilon \tag{21}$$

where

$$C_1 = max\left[0.43, \frac{\eta}{\eta + 5}\right], \qquad \eta = S\frac{k}{\varepsilon}, \qquad S = \sqrt{2S_{ij}S_{ij}}$$

and G_k is the generation of turbulence kinetic energy due to the mean velocity gradients; G_b is the generation of turbulence kinetic energy due to buoyancy; Y_M is the contribution of the fluctuating dilatation in compressible turbulence to the overall dissipation rate; S_k and S_ε are user-defined source terms; $\sigma_k = 1$ and $\sigma_\varepsilon = 1.2$; and $C_{\varepsilon 1} = 1.44$, $C_2 = 1.9$.

2.3.2
Radiation transfer

The radiative transfer equation (RTE) is used for describing the transfer of radiant energy in the reactor as a function of the position ($\vec{r}$), the direction ($\vec{s}$) and the wavelength (λ) (Viskanta and Mengüç, 1987). The radiative transfer equation for an absorbing, emitting and scattering medium is expressed in equation 22.

$$\nabla \cdot (I_\lambda(\vec{r},\vec{s})\vec{s}) + (a_\lambda + \sigma_s)I_\lambda(\vec{r},\vec{s}) = a_\lambda n^2 I_{b\lambda} + \frac{\sigma_s}{4\pi}\int_0^{4\pi} I_\lambda(\vec{r},\vec{s}')\,\phi(\vec{s}\cdot\vec{s}')d\Omega' \tag{22}$$

where I_λ is the radiation intensity; s the path length; a_λ the absorption coefficient; n the refractive index; $I_{b\lambda}$ intensity of the blackbody radiation; σ_s the scattering coefficient; $\vec{s}'$ the scattering direction vector; ϕ the scattering phase function and Ω' the solid angle.

Modest (2013) explained that the term on the left side of the equation corresponds to the emitted intensity gradient along the propagation direction, while the first term on the right side corresponds to the augmentation due to black-body emission, the second term to attenuation due to absorption and out-scattering and the last term to augmentation due to in-scattering. A representative diagram of these terms is presented in Figure 2.4.

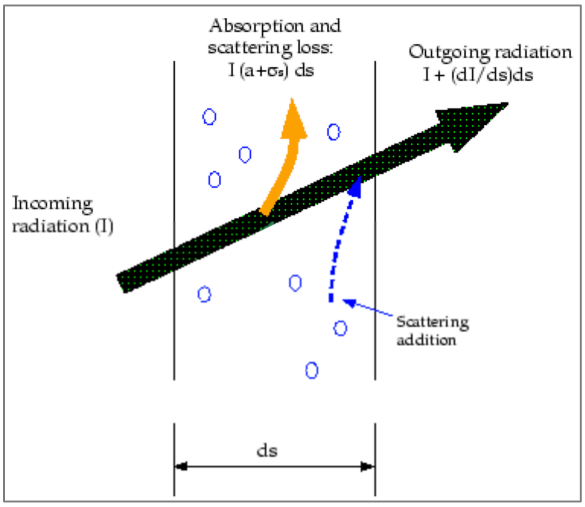

Figure 2.4: Diagram representing the terms of the radiative heat transfer equation. Font: Adapted from ANSYS manual.

Among the numerous approximate methods that have been developed over the years to solve the RTE, FLUENT offers five radiation models to choose from, which are: The Discrete Transfer Radiation Model (DTRM); P-1 Radiation Model; Rosseland Radiation Model; Surface-to-Surface (S2S) Radiation Model; and the Discrete Ordinates (DO) Radiation Model. Similar to the turbulence models, ANSYS manual provides a series of parameters to take into consideration when choosing the appropriate radiation model, such as the optical thickness, scattering and emissivity, the presence of semi-transparent walls, among others. FLUENT allows to set the rigor in which the angular discretization will be carried out, having an impact on the computational cost. For CFD modeling of reactor performances, the DO model is the most widely used.

The DO model consists of solving the radiative transfer equation for a finite number of ordinate directions ($\vec{s}_i, i = 1,2, \dots, n$) covering the total solid angle range of 4π. Without computational solutions Modest (2013) explained that for each ordinate, the RTE is written and the integrals over direction terms are replaced by a quadrature (w_i) summed over each ordinate (equation 23), transforming equation 22 in the expression 24. The author then points out that these are subject to the boundary conditions (equation 25), thus resulting in a set of n simultaneous, first-order, linear partial differential equations for $I_i(r) = I(r, \vec{s}_i)$.

$$\int_0^{4\pi} f(\vec{s})\, d\Omega' \cong \sum_{i=1}^{n} w_i\, f(\vec{s}_i) \tag{23}$$

$$\vec{s}_i \cdot \nabla I(\vec{r}, \vec{s}_i) = aI_b(\vec{r}) - (a + \sigma_s)I(\vec{r}, \vec{s}_i) + \frac{\sigma_s}{4\pi}\sum_{j=1}^{n} w_j I(\vec{r}, \vec{s}_j)\phi(r, \vec{s}_j, \vec{s}_i) \tag{24}$$

$$I(\vec{r}_w, \vec{s}_i) = \epsilon(\vec{r}_w)I_b(\vec{r}_w) + \frac{\rho \vec{r}_w}{\pi}\sum_{\vec{n}\cdot\vec{s}_j<0} w_j I(\vec{r}_w, \vec{s}_j)\left|\vec{n} \cdot \vec{s}_j\right|, \quad \vec{n} \cdot \vec{s}_j > 0 \tag{25}$$

Instead, ANSYS manual explains that FLUENT performs the integration of the RTE over each wavelength interval ($\Delta\lambda$), resulting in transport equations for the radiant energy contained in the wavelength band: $I_\lambda \Delta\lambda$. Therefore, the total intensity in each direction is obtained by the summation over the wavelength bands, as shown below.

$$I(\vec{r}, \vec{s}) = \sum_{\kappa} I_{\lambda\kappa}(\vec{r}, \vec{s})\, \Delta\lambda_\kappa \tag{26}$$

Overall, from the manual, it becomes evident that the DO model is suitable for most of the problems in radiation modeling. It is capable of accounting for scattering and exchange of radiation between gas and particulates. It is the only model, available on FLUENT, that allows to model semi-transparent walls and specular reflection for specular and partially-specular walls. With the DO model, it is possible to compute non-gray radiation and it is the best model for computing radiation from localized heat sources.

The influence of the reflection from the reactor inner-wall has gained particular interest, in recent years, as it has been proven that designing reactors with highly reflective materials, such as aluminium, can increase the average fluence rate of a UV reactor (Sommer et al, 1996). There are two types of reflection phenomena: specular reflection, where the UV light is reflected like in a mirror; and diffuse reflection, where the UV light is reflected from a surface in all directions. Over the years, however, researchers have debated the ability of the DO model to accurately predict the influence of the reflection from the reactor inner-wall. Liu et al, (2004) found that the DO model significantly overestimated the fluence rates near the lamp and underestimated them near the wall, while Ho (2009) found good agreement between the results provided by the DO model and the experimental data.

In a more recent research, Li et al. (2017) also found the DO model over predicted results. To account for these inaccuracies, they introduced individual calibrations factors (CF_i) into the Direct Irradiation (E_o) calculations, that reduced the overall input value in the boundary condition settings. The CF_i had different ranges depending on the water transmittance, since the influence of the inner wall reflection increases with the capacity of the water to transmit light. This means that a higher overestimation of results was expected for waters with higher transmittance and, therefore, required a higher reduction. The authors were able to prove CF_i a reliable tool for UV radiation modelling with reflective inner walls and applied them to evaluate the effect of the inner-wall reflection on the fluence rate and the reactor performance, with a special focus on diffuse reflection. The research proved that reactors with reflective inner walls increase the fluence rates and, for L-shape UV reactors, a higher diffuse reflection contributed to the fluence rate distribution uniformity, which resulted in a significant increment of the UV dose.

2.3.3
Kinetics

As stated by Peyton (1990), the purposes for modeling AOPs can be summarized into two main ones: as a research tool that allows for a better understanding of the various chemical processes that occur simultaneously in a system and as a design tool for adjusting AOPs to a specific application, by allowing to estimate the effects of changing operational variables.

Peyton (1990) also pointed out that process modeling can be done at different levels depending on the information available on the AOP and resources available. A kinetic model provides the most information and the best comparison of the model with laboratory data, when compared to other types of mathematical models. This is because the model considers all the reactions occurring in the system, as well as the rate equations of the main species in solution (Crittenden et al., 1999).

Over the years, researchers have developed several kinetic models that can be separated into two main categories: models that consider the pseudo-steady state approximation of the OH• radicals formation and models that release this assumption. Lay (1989) and Glaze et al. (1995) were the first ones to propose the pseudo-steady state approach, assuming the variation in time of the free radical species to be zero. Moreover, their kinetic model also considered no variations in the solution pH during the process. It did, however, consider the most important reactions occurring in a completely mixed batch reactor (CMBR). Later on, a kinetic model, employing the pseudo-steady state assumption, for a completely mixed flow reactor (CMFR) was developed by Liao (1993) and Liao and Gurol (1995). Stefan et al. (1996) developed the most comprehensive kinetic model employing the pseudo-steady state approximation to date.

A kinetic model that does not utilize the pseudo-steady state assumption was proposed by Yao et at. (1992). The software used by the author had, however, notable limitations, as it did not consider acid-base equilibrium and the variation of the photolysis rates. In fact, the software was not capable of modeling complex flow reactor kinetics. Crittenden et a. (1999) took the next step by developing the AdOx kinetic model, that solves a series of ordinary differential equations (ODE) to predict the degradation of parent organic compounds and the consumption of H_2O_2 in a CMBR. The model considers all of the photochemical and chemical reactions of the degradation of the parent organic compound, it allows for variations in pH and abandoned the pseudo-steady state assumption. It was verified using the experimental data from the study of Glaze et al. (1995).

Mazellier et al. (2002) further improved the AdOx kinetic model by adding the reactions of carbonate radicals. Sharpless and Linden (2003) included OH• radical scavenging by NOM that was further elaborated by Song et al. (2008) and Audenaert et al. (2011), the latter bringing application to wastewater. As mentioned before, Alpert et al. (2010) used CFD to evaluate the performance of a UV/H_2O_2 AOP system for the removal of methylene blue, combining turbulence, radiation and kinetic models including DOC as a hydroxyl radical scavenger. The Eulerian approach was used to solve the kinetic model in all the mentioned research, which consists on computing the concentrations of the main chemical species over the computational domain. More recently, researchers have used the Lagrangian method that uses particle tracks to predict compound degradation (Sozzi and Taghipour, 2006; Wols and Hofman-Caris, 2012; Wols et al., 2015). Wols et al. (2014) added nitrate reactions to the reaction scheme, to increase the applicability of the model on a wider range of water matrices. The model was validated using collimated beam experiments, that allow for an accurate verification since it is possible to control the conditions of the process and the hydraulics.

The mechanisms of the UV/H_2O_2 process considered in the AdOx model and presented by Crittenden et al. (1999) can be divided into the elementary reactions of H_2O_2 photolysis, the OH• radical reactions and the reactions with other species. As the solution containing H_2O_2 is irradiated with UV-light a series of chain reactions that describe the photolysis of H_2O_2 occur, these have been previously described in Table 2.1. The OH• radicals generated from the photolysis rapidly react with the organic compounds present in the solution. Superoxide, carbonate and phosphate radicals are also capable of oxidizing the organic contaminant. Moreover, organic pollutants can suffer direct photolysis when irradiated with UV-light. Finally, the model describes the interaction with other species, such as background organic matter (BOM) and carbonate and bicarbonate ions, that scavenge OH• radicals reducing the oxidation efficiency of the contaminant of concern. All of the reactions can be found in literature, such as in the work of Wols et al. 2014.

The photolysis of a compound *R* can be described by a first-order rate equation (Wols et al., 2014), shown below:

$$\frac{d[R]}{dt} = -\ln(10)\varphi_R \varepsilon_R [R] E_p(x) \quad (27)$$

where φ_R is the quantum yield in [mol/Einstein], which represents the fraction of photons that decompose the compound over the total number of photos absorbed by the compound. ε_R is the molar absorption [m^2/mol], $[R]$ is the concentration of the compound R in [mol/L] and $E_p(x)$ is the photon fluence rate in a small water volume [Einstein/m^2/s]. The average fluence rate along the particle track ($\overline{E_p}$) is used, since the photolysis follows a first-order rate equation (Wols et al., 2015), which is given by equation 28:

$$E_p(x) = \overline{E_p} = \frac{I_p}{U_f t_p} \quad (28)$$

where I_p is the UV dose received by a particle [J/m2], U_f the energy of a photon [J/Einstein] and t_p the residence time of the particle [s].

The rate equation for degradation by OH• radicals is presented in equation 29:

$$\frac{d[R]}{dt} = -k_R[\mathrm{OH}\,\bullet][R] \quad (29)$$

where k_R is the OH• radical rate constant of compound R [L/mol/s] and $[\mathrm{OH}\,\bullet]$ the concentration of OH• radicals in [mol/L]. The same equation can be applied for degradation by other radicals, such as $CO_3\,\bullet$.

The system of differential equations used to describe the formation and destruction of the species in solution can be divided into three types: first-order photolysis reactions, acid-base equilibrium reactions and second-order reactions. With the equilibrium reactions being written in the same way as the second-order reactions.

The generic photolysis reaction of compound R is written in equation 30 and the respective reaction rate in equation 31 (Wols et al., 2014):

$$n_i R_i + hv \rightarrow n_j R_j \quad (30)$$

$$v^{photo} = \ln(10)\varphi_R \varepsilon_R [R] E_p(x) \quad (31)$$

where n is the number of moles consumed (n_i) and produced (n_j). A general structure of the second-order reactions is presented in equation 32 and the respective reaction rate in equation 33 (Wols et al., 2014):

$$n_i R_i + n_j R_j \xrightarrow{k_{ij}} n_k R_k + n_l R_l \quad (32)$$

$$v^{reac} = k_{ij}[R_i]^{n_i}[R_j]^{nj} \tag{33}$$

where k_{ij} is the reaction rate constant.

3
MATERIALS AND METHODS

Experimental data for process modelling were obtained during a research activity previously carried out at the Catalan Institute for Water Research (ICRA), in Girona (Spain). Samples from three water matrices were collected, and experimental analysis were performed to characterize them. Tracer tests were carried out to assess the reactor behavior under different operating conditions. Finally, tests were performed to determine the reactor removal percentage of the contaminants of interest. All of the data collected and the specifics on the operating conditions for these tests are presented in the following chapters.

For the CFD model, the approach described in the literature review was followed, first creating the geometric model using Gambit and then applying the fluid dynamic, irradiance and UV dose models. These simulations were carried out using the commercial simulation software ANSYS FLUENT and were considered to have reached convergence at residual values smaller than 10^{-6}. After data processing, the kinetic model was elaborated using MATLAB. Details of the procedure are described in the following chapters together with the definition of the boundary conditions and the input data required for setting up all modelling.

3.1
Experimental reactor

The pilot experiments were conducted in a cylindrical stainless-steel UV reactor (Figure 3.1). The dimensions of the UV reactor were of approximately 9 cm in diameter and 93 cm in length, with a total volume of 5.92 L. The reactor was equipped with a low-pressure mercury lamp (Philips TUV 36T5 HE 4P SE UNP/32), positioned in the annular configuration, with an electrical power output of 40 W, of which about 15 W correspond to UV-C radiation, according to the technical datasheet. The inlet and outlet piping followed the L-shape configuration, as can be seen from Figure 3.1, with diameters of 2.5 cm and 1.905 cm, respectively.

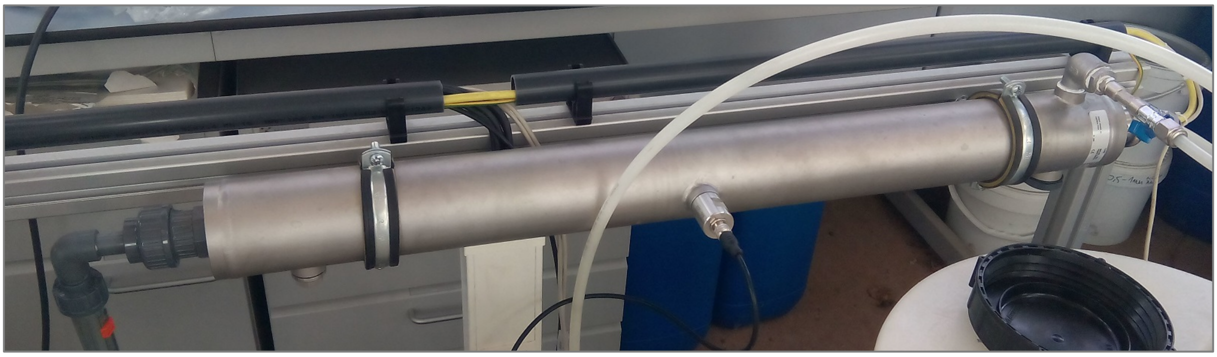

Figure 3.1: Annular photoreactor used to collect experimental data and positioning of the inlet and outlet pipes.

3.2
Residence time distribution

A tracer was used to study the fluid dynamic behavior of the reactor and compare it to an ideal theoretical model and later to that predicted by ANSYS FLUENT. The comparison was made by analyzing the residence time distribution (RTD) of the reactor at three different flow rates (low, medium and high) for three cases: experimental test, conceptual model and, after modeling the fluid dynamics of the reactor, ANSYS FLUENT simulation.

3.2.1
Tracer tests

The step input methodology was used to perform the tracer tests in the laboratory using sodium chloride (NaCl) as the tracer compound. A tap water solution containing NaCl was fed to the reactor, filled with tap water, from an upstream tank. The inlet concentration of the tracer was kept constant as the effluent conductivity (μS/cm) was measured at the outlet using a conductivity meter. Measurement continues until the effluent conductivity reached the same value of the loading tank. In parallel, a relationship between the conductivity and the NaCl concentration was obtained, in terms of a calibration line, by adding increasing amounts of NaCl into a known volume and measuring the conductivity. The non-reactivity of NaCl allowed to use the calibration line to calculate the values of the cumulative and non-cumulative concentration of NaCl over the duration of the experiment. Therefore, it was possible to assess the concentration exiting the reactor as a function of time, known as the C curve. This procedure was repeated for the following flow rates: 60 L/h (low), 120 L/h (medium) and 240 L/h (high).

It was then necessary to standardize the C curve with respect to the residence time and the output concentration to obtain the exit age distribution $E(\theta)$, or RTD, and the cumulative exit distribution $F(\theta)$. To do this, it is mandatory to obtain the mean residence time of the tracer in the reactor ($\bar{t}$) and the normalization concentration (C_N).

Ideally, the mean residence time for a reactor can be obtained by dividing the volume of the tank by the flow rate. However, it must be considered that reactors do not behave ideally, thus the measured mean residence time is lower than the theoretical one. Crittenden (2012) presents equation 27 for computing $\bar{t}$ and equation 28 for the normalized time θ.

$$\bar{t} = \int_0^\infty Ctdt / \int_0^\infty Cdt \approx \sum \overline{Ct}\Delta t / \sum \bar{C}\Delta t \qquad (27)$$

$$\theta = \frac{t}{\bar{t}} \qquad (28)$$

Similarly, the recovered concentration of the tracer is usually lower than the injected one, so the measured concentration must be used for the normalization concentration. The equation given by Crittenden (2012) for C_N is shown below.

$$C_N = \int_0^\infty Cd\left(\frac{t}{\bar{t}}\right) = \int_0^\infty Cdt/\bar{t} \approx \sum \bar{C}\Delta t/\bar{t} \qquad (29)$$

At this point, the $E(\theta)$ and $F(\theta)$ curves are obtained, knowing that:

$$E(\theta) = C/C_N \qquad (30)$$

$$E(\theta) = dF(\theta)/d\theta \qquad (31)$$

3.2.2
Tanks-in-series model

The theoretical prediction was performed using the tanks-in-series conceptual model, that aims to reproduce the fluid dynamic behavior of the reactor by choosing a hypothetical treatment line with N tanks and L lines, that satisfactorily fits the experimental data. In order to do this, the $E(\theta)$ and $F(\theta)$ curves were obtained from the expressions given by Levenspiel (1999) found below.

$$E(\theta) = N\frac{(N\theta)^{N-1}}{(N-1)!}e^{-N\theta} \qquad (32)$$

$$F(\theta) = 1 - e^{-N\theta}\left[1 + N\theta + \frac{(N\theta)^2}{2!} + \cdots + \frac{(N\theta)^{N-1}}{(N-1)!} + \cdots\right] \qquad (33)$$

The normalized time, θ, was calculated as previously using equation 28. However, in this case the mean residence time was assumed to be the total volume that goes into one line divided by the fraction of the total flow rate that enters the respective line. Therefore, firstly the number of lines and the corresponding fractions of flow (α_L) to obtain the flow rate that enters each line were assumed. Secondly, the number of tanks in each line and the corresponding fraction of volume (β_L) to obtain the volume of each tank were set. Lastly, the mean residence time was calculated. These steps were repeated until reaching a RTD that best approximated the experimental one.

3.2.3
ANSYS FLUENT simulations

The hydraulic efficiency of the reactor using CFD was assessed after modelling the fluid dynamics of the reactor using the particle tracking tool, embedded in ANSYS FLUENT. The particle tracking model consists of defining an inert injection of particles at the inlet surface of the reactor that can be monitored until each individual particle reaches the outlet of the reactor. In this way, the residence time of each particle is obtained in the form of the F curve, from which the E curve can be obtained. The Turbulent Dispersion was solved by stochastic tracking using the Discrete Random Walk Model. A brief study was performed on the ability of different turbulence models to predict the hydraulic behavior of the reactor for the medium and low flow rate conditions.

3.3
Characteristics of the water matrices

To study the influence of the water matrix on the performance of the reactor, which is the main objective of this work, three water matrices were used during the experiments: a spiked deionized water solution (SS), hotel greywater (GW) and secondary effluent from Girona WWTP (GR WWTP). Prior to the experimental procedures carried out in the reactor, the three different water matrices were characterized. The studied parameters and their respective quantitative values found are listed in Table 3.1, where, COD and BOD correspond to chemical and biological oxygen demand, TSS and VSS total suspended and volatile solids, IC inorganic carbon, TOC total organic carbon and TKN Total Kjeldahl Nitrogen.

Table 3.1: Characterization of the water matrices. Data were provided by ICRA researchers.

Parameter	Unit	SS	GW	GR WWTP
COD	mg/L	35.5	78	<LOQ
BOD	mg/L	<LOQ	61.9	1.7
Total alcalinity	mgCaCO$_3$/L	<LOQ	160.99	227.8
Conductivity	µS/cm	1.7	787.5	1067
pH	-	6.16	7.01	6.89
TSS	mg/L	<LOQ	17.1	<LOQ
VSS	mg/L	<LOQ	15.6	<LOQ

$N\text{-}NO_2$	mg/L	<LOQ	<LOQ	0.023
$N\text{-}NO_3$	mg/L	<LOQ	0.003	6.49
$P\text{-}PO_4$	mg/L	<LOQ	<LOQ	<LOQ
Cl	mg/L	0.11	101.92	133.79
$S\text{-}SO_4$	mg/L	0.03	18.01	23.38
Br	mg/L	<LOQ	0.182*	0.112*
F	mg/L	<LOQ	0.25	0.06
$Cl\text{-}ClO_2$	mg/L	<LOQ	<LOQ	<LOQ
$Cl\text{-}ClO_3$	mg/L	<LOQ	<LOQ	<LOQ
Na	mg/L	1.14	90.29	116.30
$N\text{-}NH_4$	mg/L	<LOQ	2.52	0.04
K	mg/L	0.04	5.20	22.83
Mg	mg/L	<LOQ	9.40	12.95
Ca	mg/L	0.01	23.21	65.79
Li	mg/L	<LOQ	0.01	0.03
IC	mg/L	0.26	42.23	58.67
TOC	mg/L	0.20	26.41	12.35
Total Nitrogen	mg/L	0.06	4.93	8.16
TKN	mg/L	<LOQ	6.06	2.14
Total Hardness	mg/L	0.07	96.65	217.61
Temporary Hardness	mg/L	n.d.*	55.93	188.01
Permanent Hardness	mg/L	8.581**	40.72	29.60

Following the characterization, the UV/H_2O_2 treatment was carried out. The two variables for the experiments were the flow rate, in L/h, and the H_2O_2 concentration, in mg/L. Low (60 L/h), medium (120 L/h) and high (240 L/h) flow rates were tested with no H_2O_2 addition and with 15 mg/L and 30 mg/L of H_2O_2. For each experiment, data on the absorbance at 254 nm and the radiation intensity (W/m^2) were collected. The latter was measured by a radiometer integrated in the reactor setup and positioned at the inner wall in central position along the reactor longitudinal axis. Experimental results are summarized in Table 3.2.

Table 3.2: Measures of absorbance (ABS) and Intensity (I), in W/m^2, for the UV/H_2O_2 experiments on the water matrices. Data were provided by ICRA researchers.

	Variables		**SS**		**GW**		**GR WWTP**	
EXP	**Q**	**H_2O_2**	**ABS**	**I**	**ABS**	**I**	**ABS**	**I**
1	240	0	0.005	55.8	0.32	26.25	0.24	18.45
2	240	15	0.08	53.8	0.32	26.17	0.25	18.45
3	240	30	0.01	54.17	0.32	25.67	0.25	18.27
4	120	0	0.005	54.6	0.35	24.03	0.25	18.90
5	120	15	0.01	55.15	0.30	27.23	0.24	19.23
6	120	30	0.01	54.95	0.30	27.00	0.25	19.20
7	60	0	0.004	49.3	0.35	24.33	0.19	20.47
8	60	15	0.01	54.15	0.35	23.45	0.20	19.90
9	60	30	0.01	54.55	0.35	23.67	0.25	24.90

The water absorbance is not expected to change with the addition of H_2O_2. Some of the values found for the spiked solution (0.08) and GR WWTP (0.19 and 0.20) were considerably higher or lower, respectively, than expected, due to experimental errors. To correct these deviations, those values were not considered when obtaining the average absorbance and thus the transmittance, as reported in Table 3.3.

Table 3.3: Average absorbance (ABS), standard deviation (σ), coefficient of variation (cv) and transmittance (T) for the UV/H_2O_2 experiments on the different water matrices.

Parameter	SS	GW	GR WWTP
ABS	0.010	0.33	0.25
σ	-	0.021	0.005
cv	-	6.5%	2.0%
T	97.7%	46.9%	56.6%

The UV/H_2O_2 treatment was performed to study the average removal of the contaminants of interest. The concentrations of Ibuprofen, Metoprolol, Sulfamethoxazole, Carbamazepine and Venlafaxine were evaluated for each water matrix before (t=0) and after the experiments (t=5 or t=10) variating the flow rate and the H_2O_2 concentration. The average concentrations of the substances measured before carrying out the experiments (t=0) are shown in Table 3.4. In case of the SS, the contaminants were previously spiked and all the experiments were performed. For the other water matrices only experiments 4 and 5 were carried out. A summary of results is presented in Table 3.5.

Table 3.4: Concentrations of contaminants at t=0 (Cin), in μg/l, calculated as the average of the experiments for three water matrices. Data were provided by ICRA researchers.

	Ibuprofen	Metoprolol	Sulfamethoxazole	Carbamazepine	Venlafaxine
SS	24.0	21.9	29.3	28.1	20.0
GW	37.7	31.1	39.0	22.8	28.7
GR WWTP	25.8	28.0	29.7	22.7	30.7

Table 3.5: Average concentration at outlet (Cout), in μg/l, and removal (%) of the contaminants obtained for experiments 1 to 9 for the SS and 4 and 5 for the GW and GR WWTP matrices.

		Ibuprofen		Metoprolol		Sulfamethoxazole		Carbamazepine		Venlafaxine	
	E	Cout	Removal	Cout	Removal	Cout	Removal	Cout	Removal	Cout	Removal
Spiked Solution	1	17.7	26.4%	17.0	22.5%	0.50	98.0%	21.3	24.2%	15.7	21.6%
	2	0.50	98.0%	0.50	97.7%	0.50	98.0%	0.50	98.2%	0.50	97.5%
	3	0.50	98.0%	0.50	97.7%	0.50	98.0%	0.50	98.2%	0.50	97.5%
	4	15.1	37.1%	15.7	28.4%	0.50	98.0%	19.6	30.3%	16.0	20.0%
	5	0.50	98.0%	0.50	97.7%	0.50	98.0%	0.50	98.2%	0.50	97.5%
	6	0.50	98.0%	0.50	97.7%	0.50	98.0%	0.50	98.2%	0.50	97.5%
	7	15.5	35.3%	17.5	20.3%	0.50	98.0%	20.5	27.2%	18.1	9.6%
	8	23.0	4.1%	0.50	97.7%	0.50	98.0%	0.50	98.2%	0.50	97.5%

	9	0.50	98.0%	0.50	98.0%	0.50	98.0%	0.50	98.2%	0.50	97.5%
GW	4	35.7	5.5%	33.0	-6.2%	2.50	93.6%	22.9	-0.3%	27.8	3.4%
	5	31.6	16.3%	26.9	13.5%	2.19	94.4%	22.6	1.2%	23.6	17.8%
GR	4	21.6	16.4%	23.9	14.8%	5.61	81.1%	21.5	5.2%	24.8	19.3%
	5	12.6	51.3%	13.7	50.9%	3.14	89.4%	11.3	50.3%	14.2	53.7%

3.4
CFD model setup

Using Gambit, a 3D model of the reactor was created, with a cell count of about 1.000.000, and later imported into the software ANSYS FLUENT. The elements included in the model are presented in Figures 3.2 to 3.4, namely the main constituents are the reactor, the UV lamp, and the inlet and outlet piping.

The 90º elbows of both the inlet and outlet piping were carefully reproduced in the 3D model to account for the possible velocity variations and swirling in the flow. The UV lamp consisted of the lamp itself, one plastic support on each extremity of the lamp and a protection tube made of quartz, referred to as the sleeve. In between the lamp and the sleeve an air medium was accounted for. All the elements of the lamp resulted in a radius of 1.5 cm.

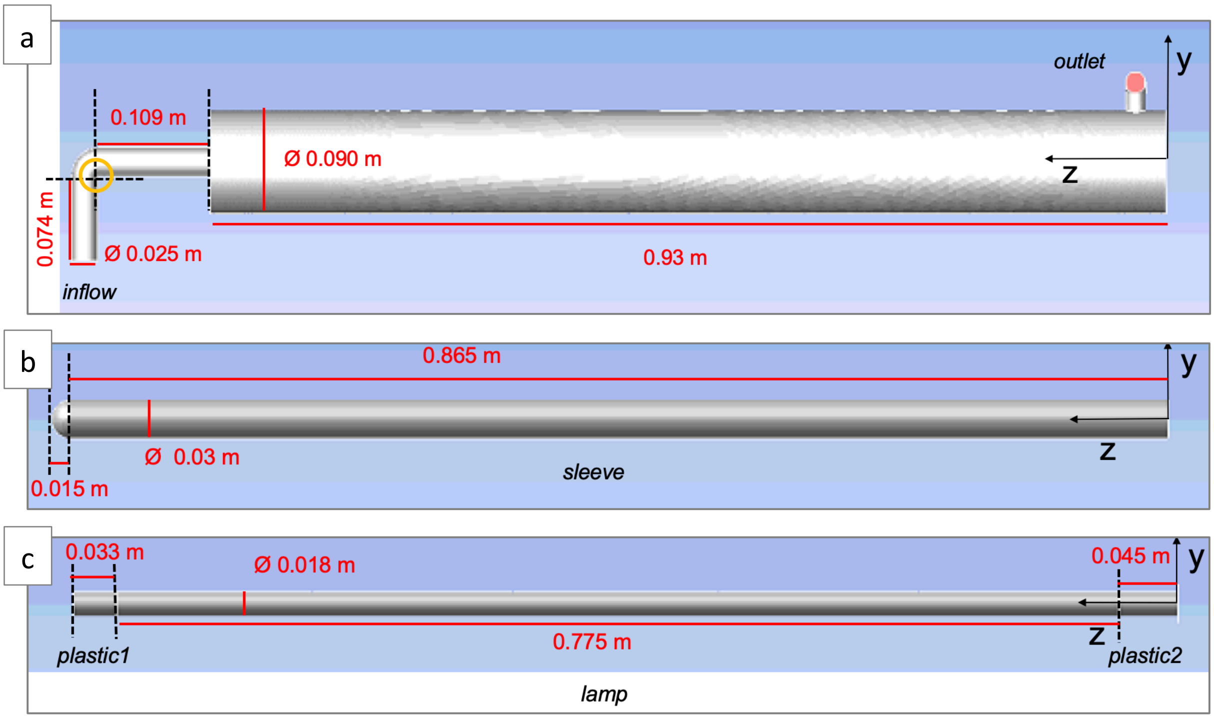

Figure 3.2: Side view of the modelled reactor (a), the lamp protection tube (b) and the lamp with its plastic supports (c).

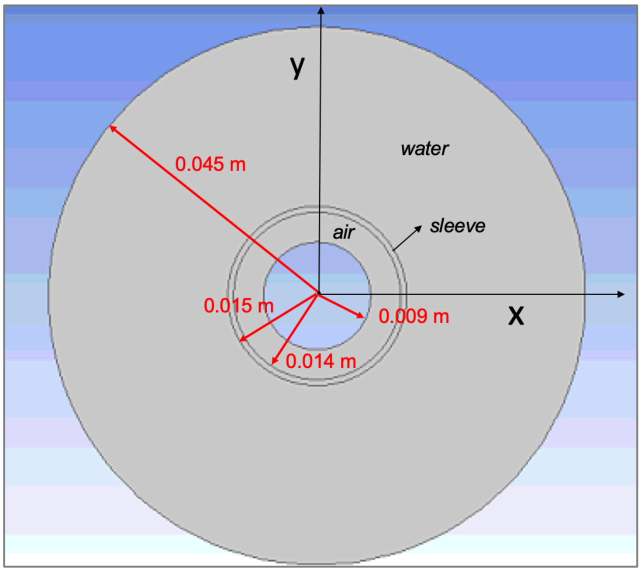

Figure 3.3: Cross section of the reactor specifying the thickness of the lamp, its protection tube and the distance between them.

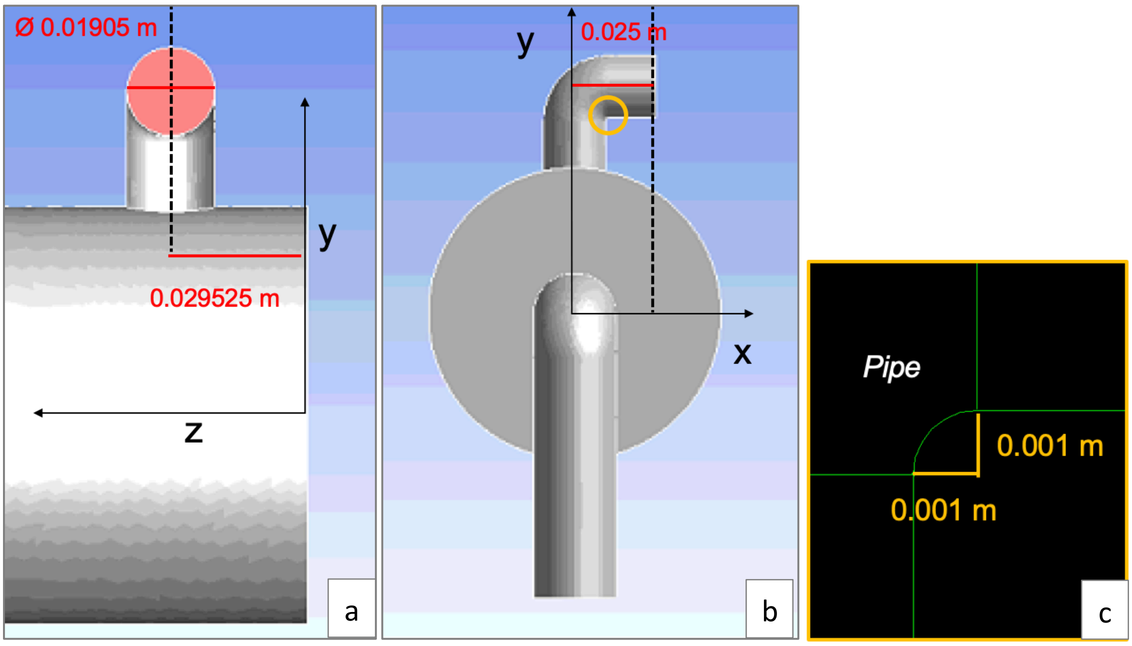

Figure 3.4: Outlet diameter and distance from the closest edge of the reactor (a), outlet pipe (b) and 90º detail of both inlet and outlet pipes (c).

3.4.1
Radiation transfer

This section is dedicated to describe the methodology used for simulating the UV radiation in the reactor by ANSYS FLUENT. The DO radiation model was applied and the scope was to evaluate the local values of irradiance (I), the Local Volumetric Rate of Photon Absorption (LVRPA) and the overall energy balance of the system, for the different water matrices. As well as, to simulate the effects of various inner-wall diffuse reflections.

3.4.1.1
Angular discretization

In order to determine the most efficient combination of divisions by pixels, known as angular discretization, it was necessary to simulate the irradiance behavior, in W/m^2, in a transversal section of the reactor for different combinations of angular discretization. The plots were compared at 1/3, 1/2 and 2/3 of the length of the reactor (z axis). The simulations were performed for 6, 8, 10 and 12 divisions and pixels and their respective permutations for the GW matrix.

A further confrontation was performed between the 8 pixels by 8 divisions and 12 pixels by 12 divisions. The computational time increases considerably from one to the other, but the visual differences obtained from the first simulations were not noticeable. To achieve a more accurate comparison 8 radiuses (x axis) were evaluated at 1/2 of the reactor (z axis), the disposition of these radius is shown in Figure 3.5. For each radius, an exponential function was estimated allowing to compare the irradiance values of the two combinations at 1/3 and 2/3 radial distance. Furthermore, two water matrices were considered: the one with the highest absorbance (GW) and the one with the lowest (SS).

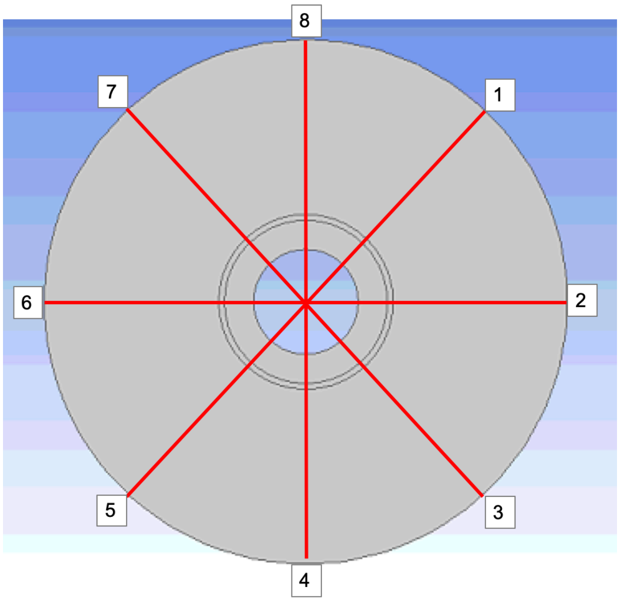

Figure 3.5: Cross section of the reactor specifying the number assigned to each radius.

3.4.1.2
Definition of the boundary conditions

The lamp dimensions allow for the calculation of the intensity in W/m^2. With a length of 77.5 cm and diameter of 1.8 cm, the lateral area is equal to 438 cm^2. Knowing that the UV-C corresponds to approximately 15 W, the emission intensity was estimated to be 342 W/m^2. The lamp was set to emit diffuse radiation and its walls were considered as semi-transparent so the radiation could pass through and be transmitted to the next surface. Because the DO equations are solved in the fluid zones it is important to specify the solid adjacent zones. The quartz sleeve was also considered as semi-transparent, thus allowing the radiation to be coupled, but not as emitting radiation.

The internal walls of the stainless-steel reactor typically result in a reflectivity (R) of 25%. Following equation 34, reported in the ANSYS FLUENT Manual (ANSYS, 2010), it was possible to find the internal emissivity (e) equal to 0.75.

$$R = 1 - e \tag{34}$$

3.4.1.3
Calibration of the DO radiation model

Initial simulations showed an overestimation of the irradiation values when compared to the experimental data. As a result, a series of individual calibration factors (CF_i) were introduced in the boundary conditions, following the procedure described by Li et al. (2017). The Direct Irradiation was, therefore, defined as:

$$E_o = CF_i \frac{P\eta}{A} \tag{35}$$

where, E_o is the Direct Irradiation (W/m^2), P is the lamp power (W), η is the lamp UV-C efficiency and A is the surface area of the lamp (m^2). Knowing from previous calculations that $\frac{P\eta}{A} = 342\ \mathrm{W}/m^2$.

For the water matrices with lower transmittance a higher CF_i was adopted, while for the spiked solution a lower one was chosen (Table 3.6). These values were selected based on the ranges of CF_i used by Li et al. (2017).

Table 3.6: Values of absorbance (ABS), transmittance (T), calibration factor (CF_i) and intensity (I) for the three water matrices.

	SS	GW	GW WWTP
ABS	0.01	0.33	0.25
T (%)	98	47	57
CF$_i$	0.8	0.95	0.95
I (W/m^2)	274	325	325

3.4.1.4
LVRPA and Energy Balance

The ANSYS FLUENT manual provides an expression (equation 36) for the diffuse reflectivity (Rd) that requires to set a diffuse fraction of inner-wall reflection (fd). Therefore, different scenarios of inner-wall diffuse reflections were simulated following Li et al. (2017) procedure and, thus, setting fd values at 0.1, 0.5 and 0.9 for low, moderate and high Rd, respectively. These scenarios were later compared using the LVRPA, that corresponds to the rate of energy absorbed per unit of volume by the particles in the water, thus allowing for a better understanding of the distribution of OH• radicals production in the reactor geometry and consequently, the interference of the fd parameter.

$$Rd = fd(1 - e)\ [-] \tag{36}$$

Once a simulation is done it is possible to obtain the LVRPA in W/m^2 by defining a custom function in ANSYS FLUENT following equation 36. The LVRPA alongside the radius of the reactor curves were plotted for the different fd. The evaluation of the influence of fd was done for the highest and lowest transmittance waters, SS and GW respectively.

$$LVRPA = I \times ABS\quad [\mathrm{J/m^2}] \tag{37}$$

The energy balance can be computed as described by equation 38, where Et corresponds to the total energy emitted by the lamp, or Direct Irradiation; Ew, Ea, Eq and Ei to the energy absorbed by the water, the air, the quartz sleeve and the reactor inner-wall. The terms on the right side of the equation are obtained from the simulation.

$$Et = Ew + Ea + Eq + Ei\ [W] \tag{38}$$

3.4.2
Fluid dynamics

In this section, the methodology used for simulating the hydrodynamic behavior of the reactor in ANSYS FLUENT is described. The model selected was the RKE model, based on the RANS approach, with the standard wall function. The scope was to evaluate the velocity profiles in the reactor for the different flow rates. In addition, the inlet profile velocities were obtained and compared to the analytical profiles for a laminar flow.

3.4.2.1
Definition of the boundary conditions

Inflow and outflow velocities were obtained for the low (60 L/h), medium (120 L/h) and high (240 L/h) flow rates to simulate the experiments carried out in the laboratory. Knowing that the diameter (d) of the inlet pipe is equal to 2.5 cm, the inflow area was estimated to be 4.91 cm^2, therefore the inlet velocities were calculated using equation 39. The same procedure was repeated for the outlet with a 1.905 cm diameter, hence finding an area of 2.850 cm^2. The results can be found Table 3.7.

$$v = Q/A \ \ [m/s] \tag{39}$$

Table 3.7: Inlet and outlet velocities (m/s) of the reactor for 60 L/h, 120 L/h and 240 L/h which represent low, medium and high flow rates, respectively.

			v (m/s)		
	d (m)	**A (m^2)**	**Low**	**Medium**	**High**
Inlet	0.025	4.91E-04	0.034	0.068	0.136
Outlet	0.019	2.85E-04	0.058	0.117	0.234

Another parameter required for the k-ε model is the Turbulence Intensity (I), which is defined by the ANSYS FLUENT manual as:

$$I = 0.16(Re_{DH})^{-1/8} \ \ [\%] \tag{40}$$

with Re_{DH} being the Reynolds Number obtained with:

$$Re_{DH} = \ \rho v d/\mu \tag{41}$$

where ρ is the flow density, 998.21 kg/m^3, and μ is the dynamic viscosity, 1.002E-03 kg/m/s. Results for all three operational conditions are presented in Table 3.8.

Table 3.8: Inlet and outlet Reynolds number (Re_{DH}) and turbulence Intensity (I), in percentage, of the reactor for 60 L/h, 120 L/h and 240 L/h which represent low, medium and high flow rates, respectively.

	Inlet			**Outlet**		
	Low	**Medium**	**High**	**Low**	**Medium**	**High**
Re_{DH}	845.62	1691.23	3382.46	1109.73	2219.46	4438.93
I (%)	6.9	6.3	5.8	6.7	6.1	5.6

When setting up the model in ANSYS FLUENT, it is required to specify two boundary conditions to the inlet and two for the outlet. The hydraulic diameters were set for both of the cases, while the velocity was only specified for the inflow and the turbulence intensity for the outflow. Lastly, the no-slip condition was set for all the inner-walls of the reactor.

3.4.2.2
Inlet velocity profiles

To understand if the computational calculations simulated the reactor properly, it was necessary to compare the results to the analytical solution. In order to do this a User Defined Function (UDF) was introduced to ANSYS FLUENT, that allowed to obtain the velocity profiles at the inlet pipe. The UDF is reported in Appendix A with the values of the parameters required for its usage.

The analytical profiles were obtained by calculating the velocity, following equation 42, for the same distances (r) from the radius of the pipe (R) as the FLUENT solution, with $v_m = 2v$.

$$v_r = v_m \left[1 - \left(\frac{r}{R}\right)^2\right] \quad [m/s] \tag{42}$$

3.4.3
Dose distribution

With the radiation transfer and fluid dynamics simulations solved it was possible to assess the UV dose distribution inside the photoreactor. This was performed combining a UDF, elaborated by Sandia National Laboratories (Appendix C), that computes the cumulative UV dose (J/m^2) received by a particle, with the particle tracking tool.

Previously to the particle tracking model setting, the UDF must be loaded into ANSYS FLUENT. After the definition of the injection, it is required from the software to report the UDF results for each particle from the inlet to the outlet of the reactor. ANSYS FLUENT provides, then, the cumulative product of the incident radiation and the time along each step of the particle path.

For the purposes of this work, a histogram of the dose distribution was found to be a better representation of the data. Therefore, all results obtained from the simulation were imported once again to ANSYS FLUENT and displayed in a histogram plot that correlates the fraction of flow (particles) with their respective amount of UV dose absorbed. This UV dose distribution, alongside the residence time of the particles was later used in the kinetic model. The overall UV dose absorbed by the particles is defined as the integral of the function, or the area under the curve, which can be approximated calculating the area of the rectangles.

3.4.4
Kinetic model

To investigate the chemical reactions leading to contaminant removal, a kinetic model was developed and applied to each set of particles (Lagrangian approach) absorbing a certain amount of UV dose, with a respective residence time, as obtained in the UV dose distribution. A selection of the most relevant reactions and species interaction (Table 3.9) was done following the work performed by Wols et al. (2015), with adaptations for the specific case in study. The system of differential equations was set up in MATLAB following the general structures introduced in chapter 2. The outlet concentration of the species was calculated as the weighted average of concentrations of all particles. The quantum yields and molar absorptions of the photolysis of H_2O_2, as well as the rate constants of the first-order and second-order reactions are reported in Table 3.9.

Table 3.9: Reaction scheme for the kinetic model, with respective rate constants. Data are adapted from Wols et al. (2015).

Reaction	Rate Constant 25˚C, M^{-1} s^{-1}	Reference
(1) $H_2O_2 + hv \rightarrow 2OH\bullet$	$\varepsilon = 18.6\ M^{-1}cm^{-1}, \varphi = 0.5\ mol/E$	(Volman and Chen, 1959)
(2) $HO_2^- + H_2O_2 + hv \rightarrow 2HO\bullet + OH^-$	$\varepsilon = 228\ M^{-1}cm^{-1}, \varphi = 0.5\ mol/E$	(Baxendel and Wilson, 1957)
(3) $R_i + hv \rightarrow ?$	ε_i, φ_i	
(1) $H_2O_2 \leftrightarrow HO_2{}^- + H^+\ (pKa = 11.6)$	$1.10\times10^{10}, 2.51\times10^{-2}$	(Perry et al., 1981)
(2) $HO_2\bullet \leftrightarrow O_2^-\bullet + H^+\ (pKa = 4.8)$	$1.10\times10^{10}, 1.58\times10^{5}$	(Perry et al., 1981)
(3) $H_2CO_3 \leftrightarrow HCO_3{}^- + H^+\ (pKa = 6.35)$	$1.10\times10^{10}, 4.5\times10^{3}$	(Mazellier et al., 2002)
(4) $HCO_3^- \leftrightarrow CO_3^{2-} + H^+\ (pKa = 10.35)$	$1.10\times10^{10}, 4.5\times10^{-1}$	(Mazellier et al., 2002)
(5) $H_2O \leftrightarrow OH^- + H^+\ (pKa = 16.0)$	$1.10\times10^{10}, 1.14\times10^{-6}$	
(1) $HO\bullet + HO_2^- \rightarrow OH^- + HO_2\bullet$	7.5×10^{9}	(Christensen et al.,1982)
(2) $HO\bullet + O_2\bullet \rightarrow O_2 + OH^-$	7×10^{9}	(Beck et al., 1969)
(3) $HO\bullet + HO_2\bullet \rightarrow O_2 + H_2O$	6.6×10^{9}	(Sehested et al., 1968)
(4) $HO\bullet + HO\bullet \rightarrow H_2O_2$	5.5×10^{9}	(Buxton et al., 1988)
(5) $HO\bullet + H_2O_2 \rightarrow H_2O + HO_2\bullet$	2.7×10^{7}	(Buxton et al., 1988)
(6) $HO_2\bullet + O_2^-\bullet \rightarrow HO_2{}^- + O_2$	9.7×10^{7}	(Bielski et al., 1985)
(7) $HO_2\bullet + HO_2\bullet \rightarrow O_2 + H_2O_2$	8.3×10^{5}	(Bielski et al., 1985)
(8) $H_2O_2 + HO_2\bullet \rightarrow HO\bullet + O_2 + H_2O$	3	(Koppenol et al.,1978)

(9) $H_2O_2 + O_2 \bullet \rightarrow HO \bullet + O_2 + OH^-$	0.13	(Weinstein e Bielski,1979)
(10) $HO \bullet + CO_3^{2-} \bullet \rightarrow CO_3^- \bullet + OH^-$	3.9×10^8	(Buxton et al., 1988)
(11) $HO \bullet + HCO_3^- \rightarrow CO_3^- \bullet + H_2O$	8.5×10^6	(Buxton et al., 1988)
(12) $CO_3^- \bullet + HO_2^- \rightarrow CO_3^{2-} + HO_2 \bullet$	3.0×10^7	(Draganic et al., 1991)
(13) $CO_3^- \bullet + H_2O_2 \rightarrow HCO_3^- + HO_2 \bullet$	8×10^5	(Neta et al., 1988)
(14) $CO_3^- \bullet + HO \bullet \rightarrow products$	3.0×10^9	(Crittenden et al., 1999)
(15) $CO_3^- \bullet + O_2^- \bullet \rightarrow CO_3^{2-} + O_2$	6.5×10^8	(Neta et al., 1988)
(16) $CO_3^- \bullet + CO_3^- \bullet \rightarrow products$	3.0×10^7	(Huie and Clifton et al., 1990)
(17) $HO \bullet + DOC \rightarrow H_2CO_3$	6.0×10^8	(Vione et al., 2006)
(18) $CO_3^- \bullet + DOC \rightarrow ?$	3.4×10^6	(Canonica et al., 2005)

Since one of the objectives of this study was to evaluate the outlet concentrations and removal percentages of the contaminants present in the three water matrices, the kinetic model was solved for all five pollutants. Their respective ε_i and φ_i together with the OH• and $CO_3 \bullet$ radicals rate constants are shown in Table 3.10 and were taken from Wols et al. (2014).

The function used for solving the series of stiff ODEs was ode15. All three water matrices were tested experimentally for the operational conditions of [H_2O_2] = 15 mg/L and medium flow rate (120 L/h). Therefore, the kinetic model was applied for these same operating conditions. Values of absorbance, pH, pollutant initial concentration and initial concentration of total inorganic carbon and DOC were set in agreement with the measured characteristics of each water matrix that can be found in section 3.3.

Table 3.10: Pharmaceuticals kinetic parameters. Data are adapted from Wols et al. (2014).

Pharmaceutical	**φ (10^{-2})** [mol/Eins]	**ε (10^3)** [L/mol/cm]	**kOH (10^9)** [L/mol/s]	**kCO$_3$ (10^7)** [L/mol/s]
Ibuprofen*	19.2	0.256	7.04	-
Metoprolol	6.6	0.33	8.1	0.51
Sulfamethoxazole	8.4	13	6.3	12
Carbamazepine	0.33	5.8	9.5	-
Venlafaxine	9.7	0.38	8.8	-

The kinetic model was solved under the assumption that (1) H_2O_2 consumption is low, (2) there are no significant changes in pH, (3) the DOC concentration does not suffer significant changes, and (4) the absorbance remains constant.

4
RESULTS AND DISCUSSIONS

In the following paragraph, results from irradiance, fluid dynamic, UV dose and kinetic models are presented. In particular, the first part contains the discussion on the angular discretization required for the DO model that best fitted the purposes of this research, the simulated effects of the inner-wall reflection in the fluence rate and the closure of the energy balance of the water matrices with the lower and highest absorbance. The second part is dedicated to presenting results on the input velocity profiles for the different operational conditions and the comparison between the experimental and the simulated RTD. The third part showcases the UV dose distributions of the water matrices of interest. Lastly, in the fourth section a comparison between experimental and modelled removal rates of the contaminants is presented.

4.1
Fluence Rate distribution

4.1.1
Angular discretization

The variables taken into consideration for the selection of the appropriate angular discretization (AD) were the visual differences in the radiation intensity profile along the radius of the reactor and the smoothness of the contour lines of the cross section of the reactor, altogether with the computational time of each combination. Two examples of results exported from the software for each simulation are presented in Figure 4.1.

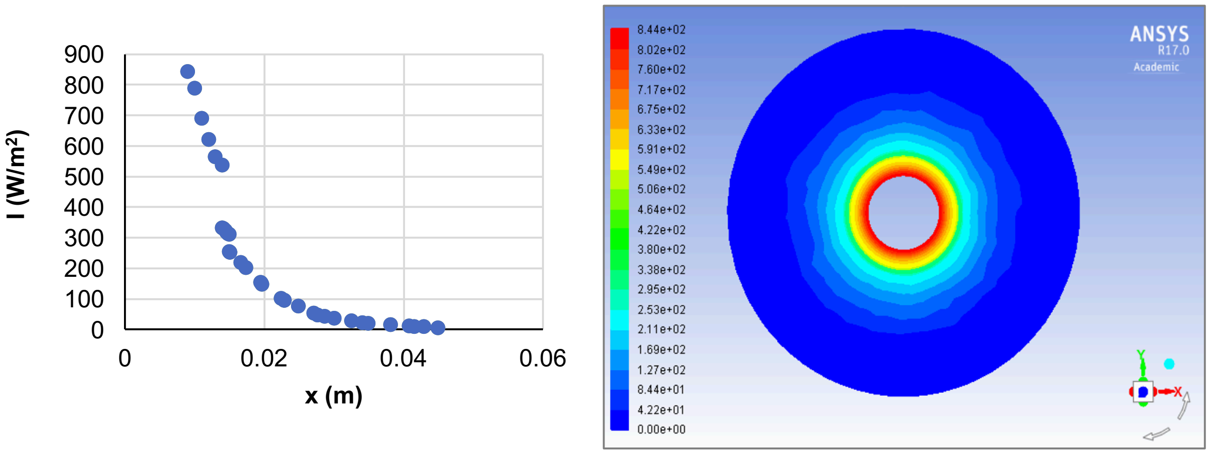

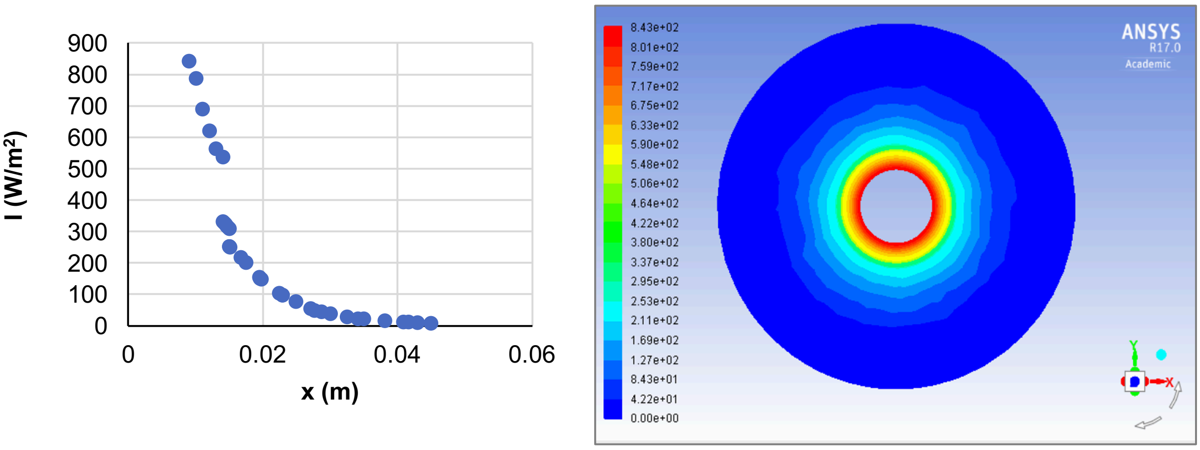

Figure 4.1: Left - plot of the radiation intensity, I (W/m^2), as the radial distance, x (m), to the lamp increases at 2/3 of the reactor (z axis). Right - surface view of intensity behavior at the same position. Results correspond to the 8 x 6 (top) and 10 x 10 (bottom) combinations that had a duration of 2 and 6.5 h, respectively.

From this initial analysis it was not possible to conclude which combination was the most efficient, since there were not many visible differences among the permutations, as it can be seen from Figure 4.1. However, it was possible to isolate the 8-by-8 AD as a possible candidate as it apparently maintained accuracy while having a relatively short duration of the simulation (3 h), when compared to other combinations. The 12-by-12 AD, for instance, was considered the most accurate but the most time consuming, with a single simulation extending for almost 13 h.

A more in detail comparison was, therefore, performed with the 12-by-12 combination, as it would allow to spot significant accuracy losses, if any, when opting for a lower AD. As described in chapter 3, for the two combinations the irradiation along the radial distance from the lamp was plotted at 1/2 of the reactor (z axis) for 8 different radius. The exponential curve for each irradiation profile, neglecting the lamp radius, was obtained (Figure 4.2) and from it the values of irradiance at 1/3 and 2/3 (x axis). An average that accounted for the 8 radius was calculated allowing to directly compare the irradiance of the 8-by-8 with the 12-by 12-AD.

Table 4.1: Average Irradiance (W/m^2), standard deviation (σ) and coefficient of variation (cv) for the 8-by-8 with the 12-by-12 combinations at 1/3 and 2/3 radial distance, x, for the GW and SS matrices.

		GW			SS		
x	**AD**	**I**	**σ**	**cv**	**I**	**σ**	**cv**
1/3	8 x 8	76.86	1.60	2.1%	107.27	2.61	2.4%
	12 x 12	76.67	1.61	2.1%	106.76	2.61	2.4%
		76.77	0.008	0.01%	107.01	0.003	0.003%
2/3	8 x 8	37.86	0.79	2.1%	74.44	0.95	1.3%
	12 x 12	37.88	0.80	2.1%	74.17	0.95	1.3%
		37.87	0.007	0.02%	74.31	0.003	0.004%

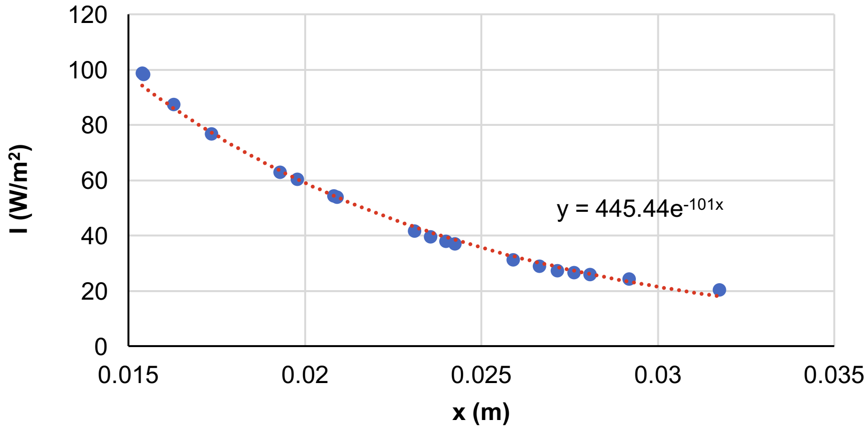

Figure 4.2: Example of the radiation intensity, I (W/m^2), as the radial distance, x (m), increases for radius 1 of the 8-by-8 combination in the GW matrix. The exponential function found was y=445.44e^{-101x}.

From the results, presented in Table 4.1, it is possible to conclude that no significant differences in the irradiation profile occur from lowering the AD. Specifically, the coefficient of variation at 1/3 was found to be 0.01% for the GW and 0.003% for the SS. Meanwhile, at 2/3 results showed 0.02% for the GW and 0.004% for the SS. Hence, the following simulations were performed using the 8-by-8 AD.

A further analysis was conducted to compare the individual simulated values of radiation of each of the 8 radius to identify possible differences not in the overall behavior but in specific points along the radial distance. In other words, the comparison was made with simulated values and not those obtained from the exponential regression. The points of comparison selected were 1/3, 1/2 and 2/3 from the radius and were plotted like shown in Figure 4.3.

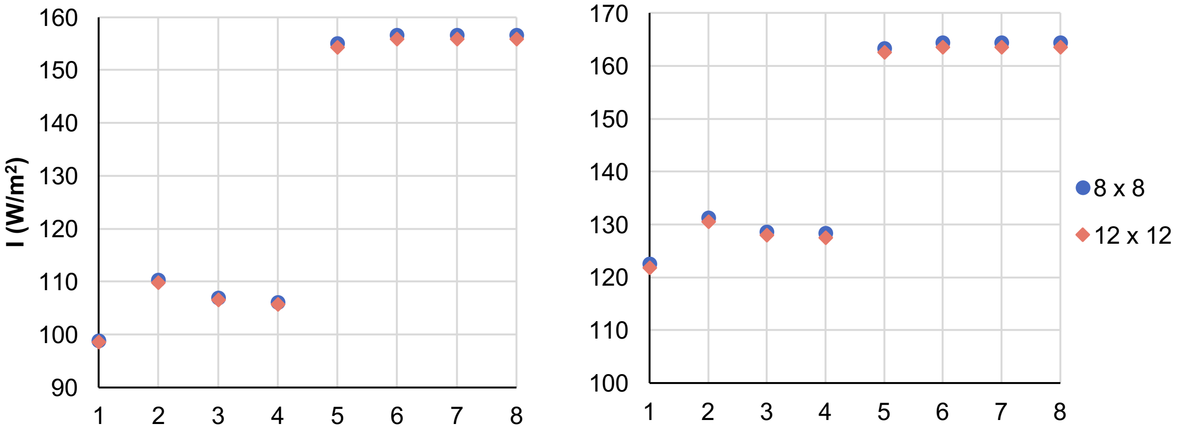

Figure 4.3: Simulated radiation intensities, I (W/m^2), for each radius at 1/3 radial distance in the 8-by-8 and 12-by-12 combinations for the GW (left) and SS (right) matrices.

All plots presented the same behavior with no major differences between the combinations. This analysis showed, however, that at a same cross section and radial distance the radiation intensities behaved slightly differently inside the reactor. Two groups can be identified, one from radius 1 to 4, with lower values, and another one from radius 5 to 8, with higher intensities. From looking at the location of the radius (Figure 3.5), the first group was mostly concentrated in the lower right of the reactor, while the second group at the top left side. This phenomena may be related to the reflection of the semi-transparent walls and the way FLUENT accounts for wall-shadowing of the inner-walls and the lamp constituents.

4.1.2
LVRPA and Energy Balance

The influence of the inner-wall diffuse reflections was simulated for the SS and GW matrices and results are presented in Figure 4.4. From the plots, it becomes evident that while for the SS there is a change in the behavior of the curve, the GW matrix suffers almost no interference. The higher the inner-wall diffuse reflection the flatter the curve becomes, meaning that the LVRPA distribution became more uniform as a result of the diffusely reflected UV light returning in all directions. Li et al. (1017) explained that in such case the optical path lengths were extended near the inner-wall but reduced near the lamp. This results in decreased LVRPA values closer to the lamp and increased ones at the inner-wall.

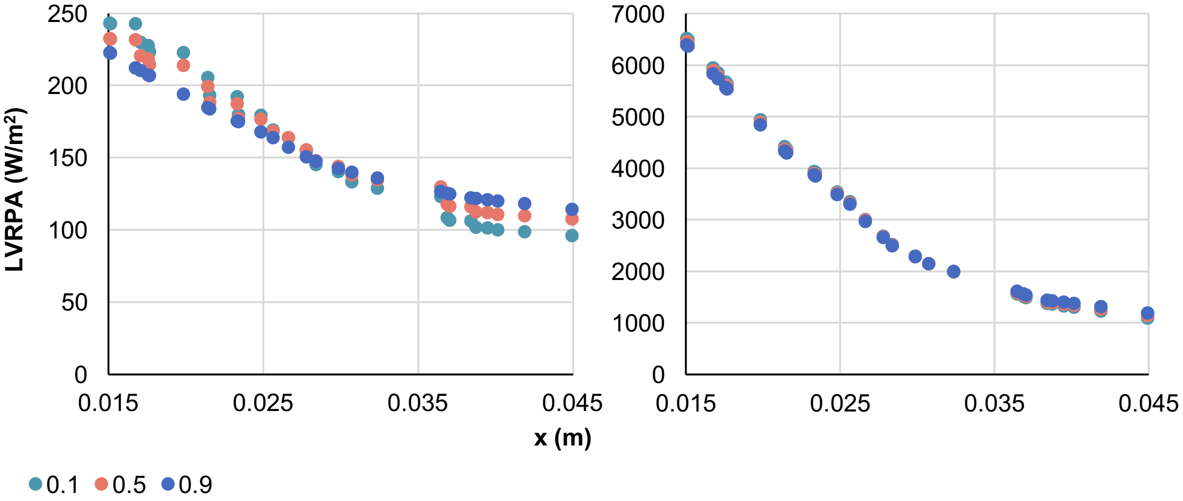

Figure 4.4: Plot of the LVRPA (W/m^2) as a function of the radial distance (m) for the three fd settings (0.1, 0.5 and 0.9) simulated on the SS (left) and GW (right) matrix.

These results are consistent with the effect of the water matrix absorbance and with those found in the literature review. The GW is characterized by a high absorbance that makes the transmittance of the intensity across the radius of the reactor more difficult. This results in no significant inner-wall interactions. On the other hand, the SS low absorbance allows for the intensity emitted by the lamp to reach the inner-wall and therefore being more affected by the material diffuse reflection. In fact, an example of the radiation profiles is presented in Figure 4.5, showing the reduction of the irradiation as the radial distance from the lamp increases to be more significant for the GW matrix. Since the influence of the diffuse reflection was only notable on the SS, the rest of the simulations were carried out considering the moderate value (fd = 0.5).

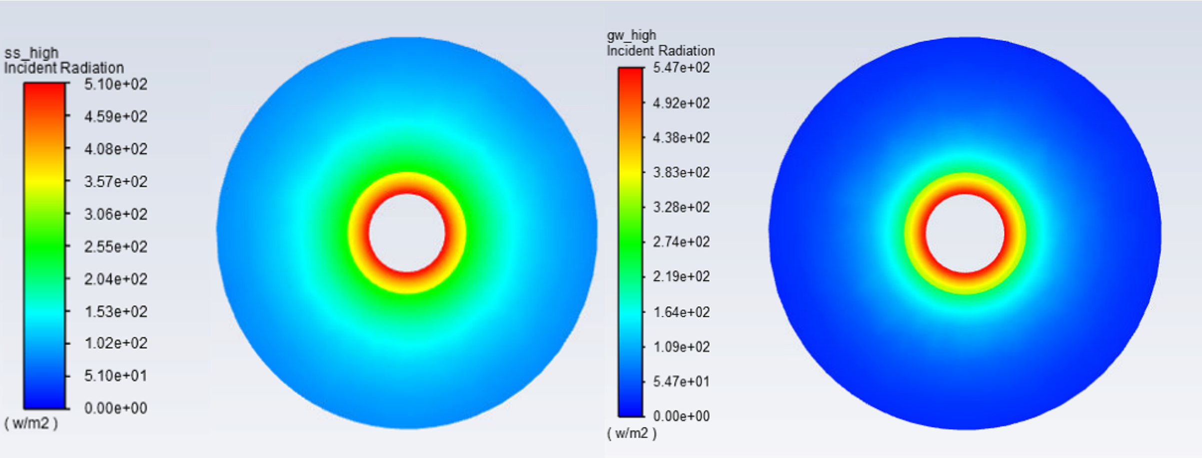

Figure 4.5: Irradiation profile (W/m^2) cross-section of the SS (left) and GW (right) matrices for high flow rate.

The results obtained from performing the energy balance are shown in Table 4.2. A small adjustment was done to the energy absorbed by the inner-wall of the reactor to close the balance, since the simulation overestimated this value. The simulation considered the energy not absorbed by the water matrix was absorbed by the inner-wall of the reactor.

Table 4.2: Values of calibration factor (CF_i); total energy (Et); energy absorbed by water matrix (Ew), by the air (Ea), by the quartz sleeve (Eq) and by the reactor inner-wall (Ei); and energy balance of the GW and SS.

	GW		**SS**	
Parameter	**W**	**%**	**W**	**%**
CFi	0.95	-	0.80	-
Et	14.22	100	11.98	100
Ew	9.66	67.9	0.55	4.6
Ea	0.00	0.00	0.00	0.0
Eq	0.13	0.90	0.15	1.3
Ei	4.40	31.2	11.27	94.1
Energy Balance	**0**		**0**	

Figure 4.6 presents a closer look at the distribution of the energy emitted by the lamp along the absorbing elements of the reactor. The low transmissivity of the GW matrix resulted in most of the energy being absorbed by the water with a smaller part reaching the inner-wall of the reactor. On the other hand, the SS is characterized by almost all of the energy reaching the inner-wall of the reactor due to the high transmissivity of the water matrix.

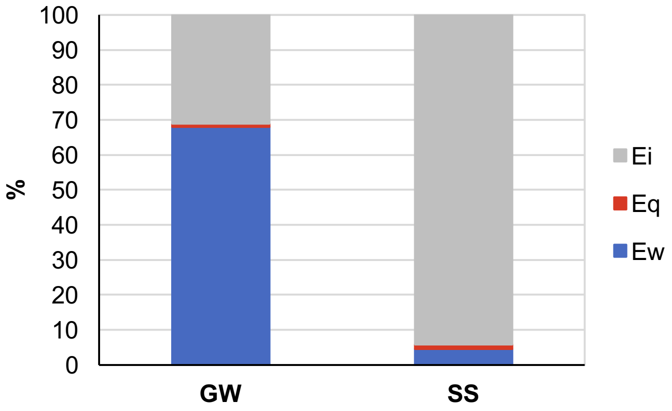

Figure 4.6: Distribution of the total energy (%) emitted by the lamp along the different absorbing elements inside the reactor.

4.2
Fluid dynamics

Figure 4.7 shows an example of the streamlines of the velocity magnitude profile starting at the inlet pipe (a), following through the inside of the reactor (b) until reaching the outlet pipe (c). From the flow pattern an initial recirculation zone can be identified in the feeding pipe, immediately after the 90º elbow. The stream enters the reactor at high speed and intercepts the lamp sleeve creating a diversion in the flow. A high gradient of momentum in different directions is created, resulting in a recirculation zone at both the top and bottom of the entrance of the photoreactor. As expected, greater vorticity was observed for higher inlet velocities. The velocity along the annular region maintains a uniform profile, with no recirculation zones. As the stream approaches the outlet there is a significant increase in velocity magnitude due to the flow being compressed in order to exit through the pipeline. Overall, the simulations proved satisfactory fluid dynamics inside the reactor with some observations on the extremities.

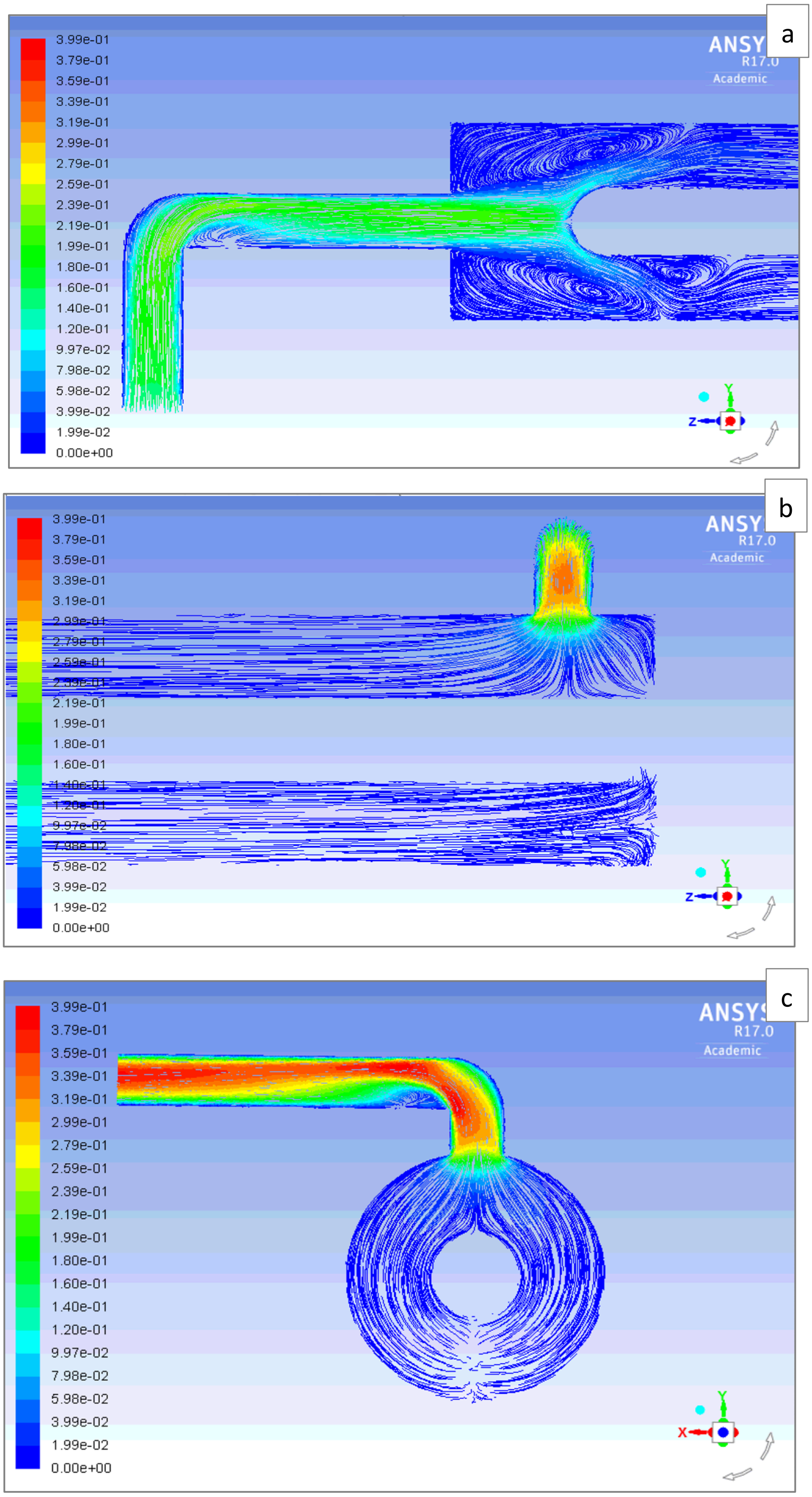

Figure 4.7: Streamlines of velocity magnitude (m/s) at the inlet pipe and entrance of the reactor (a); along the length of the photoreactor and outlet (b); and at the outlet cross-section of the reactor (c).

4.2.1
Inlet velocity profiles

The plots of the modelled and the analytical solution for the inlet velocity profiles in all three flow rate conditions are presented in Figure 4.8. The curves were obtained from the values that can be found in Appendix B. In general, the computational solution was capable of reproducing the velocity behavior with a slight underestimation that becomes more apparent closer to the pipe center.

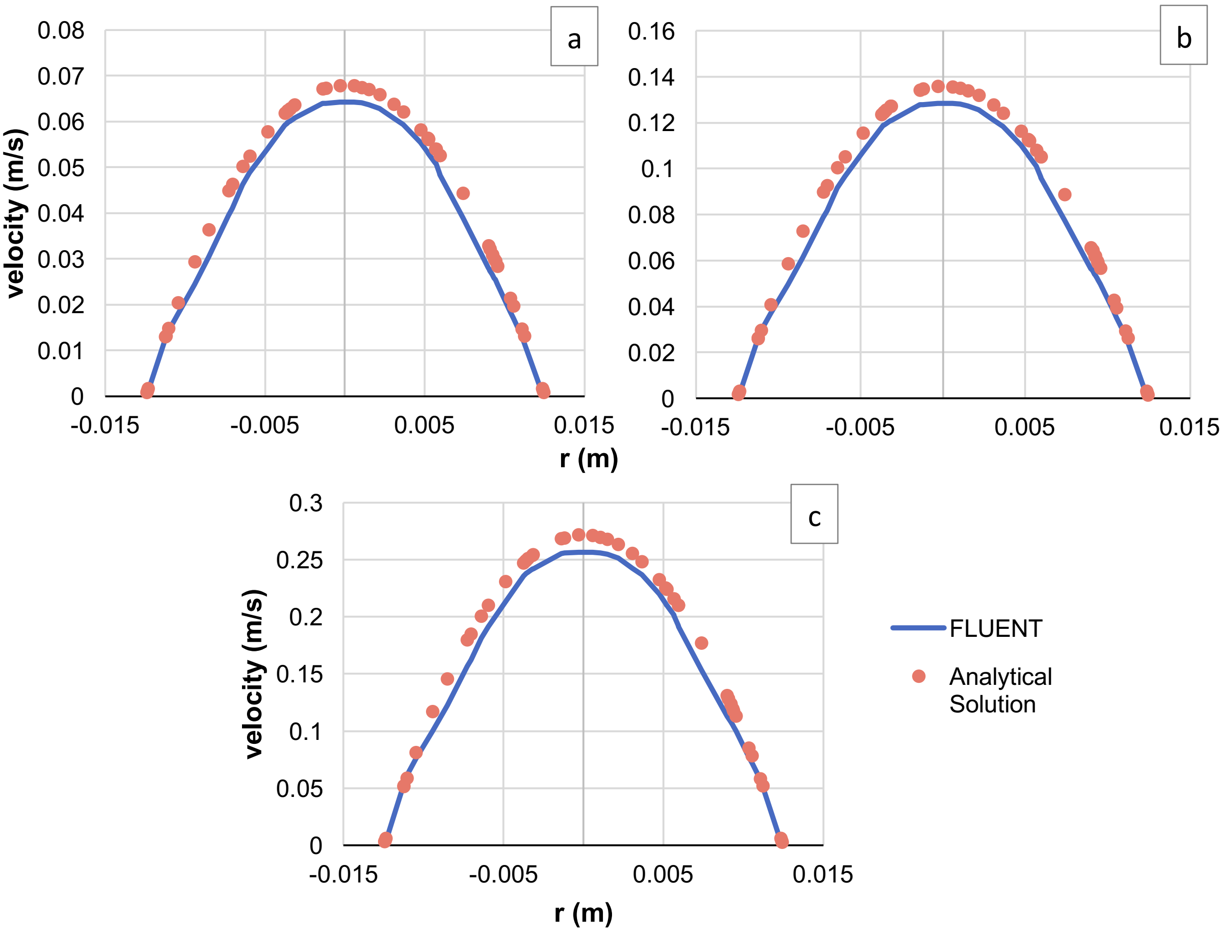

Figure 4.8: Plots of the velocity (m/s) as the radial distance (m) from the inlet pipe increases for both the modelled and the analytical solution in the low flow (a), medium (b) and high (c) scenarios.

From the Re_{DH} numbers presented in Table 3.8 the inlet flow regime of low and medium operational conditions was laminar ($Re_{DH} < 2300$), while the flow regime of the high flow rate fitted the transitional range ($2300 > Re_{DH} < 4000$). The velocity streamlines indicate that the maximum Re_{DH} number inside the reactor must be smaller than inlet Re_{DH}. Therefore, it is safe to conclude that, although the local Re_{DH} variates, the laminar regime is maintained throughout the length of the reactor for low and medium flow rates. In the case of the high flow operational condition, the entrance area can be considered to be in transitional regime and the annular region in laminar. In fact, since the analytical solution of the inlet velocity profile was found using the laminar flow model, the lack of major differences with the simulated curve proved that even for the high flow rate (Figure 4.8c) a laminar flow can be considered.

4.2.2
Residence time distribution

4.2.2.1
Tracer tests

Results from the initial experimental test to establish the relationship between the conductivity and the concentration of NaCl are presented in Table 4.3. From these results, a calibration line was plotted (Figure 4.9), that resulted in the linear expression $y=2.0103x+11.17$, with $R^2=0.9998$.

The tracer tests were then conducted for the three flow rate conditions and the calibration curve was used for computing the cumulative and non-cumulative concentrations of NaCl from the conductivity data collected. The non-cumulative concentration of NaCl was then used to plot the C curves shown in Figure 4.9.

Table 4.3: Values of conductivity (µS/cm), concentration (mg/L) and mass (mg) of NaCl from experimental test. Data were provided by ICRA researchers.

Conductivity (µS/cm)	Concentration (mg/L)	Mass (mg)
2.9	0	0.0
6.4	0	0.0
540	253	25.3
522	251	25.1
917	453	45.3
906	448	44.8
1332	651	65.1
1311	650	65.0
1712	854	85.4
1728	854	85.4
2110	1048	104.8
2130	1046	104.6

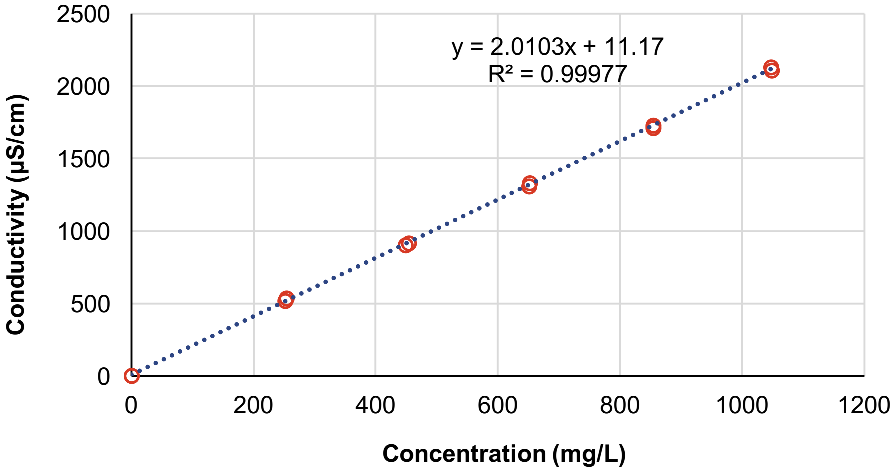

Figure 4.9: Calibration curve of conductivity (µS/cm) as a function of the concentration (mg/L) of NaCl.

In the first instance, the C curves show that no effluent concentration of NaCl was detected, corresponding to the time required for activating the pumping system and for the tracer to go through the inlet pipe and through the length of the reactor until reaching the measuring equipment, located at the outlet. The curves show that this time progressively increases with the reduction of the flow rate, as expected, with 40, 75 and 135 seconds for the high, medium and low flow rates, respectively. The abrupt increase in the outlet concentration of NaCl reached its maximum value, with the same increasing behavior at 50, 90 and 150 seconds for the high, medium and low flow rates, respectively. Immediately after, the concentration decreased gradually following an exponential until stabilizing at a minimum value for all three conditions.

The high flow rate (Figure 4.10a) reached this point quicker, at approximately 2.5 min, followed by the medium flow rate at 7 min and lastly the low flow rate at 12 min. This means that the lower the flow rate operational conditions the longer particles stay in the reactor before leaving, which can potentially result in a higher absorption of UV dose and, therefore, in a higher removal rate of the contaminants of interest. The influence of the flow rate in the UV dose absorption is analyzed in the following sections, however it is to be noted from the C curves that lowering the flow rate can result in a more complex hydraulic behavior of the reactor, which increases the difficulty and the accuracy of the modelling process.

The overall behavior of the curves, in particular the high and medium conditions (Figure 4.10a and b), resemble the response of a completely mixed flow reactor (CMFR) to the step input technique, with the outlet concentration of the tracer reaching a maximum instantly, as it is distributed uniformly in the reactor, to dissipate gradually in an exponential (Crittenden, 2012).

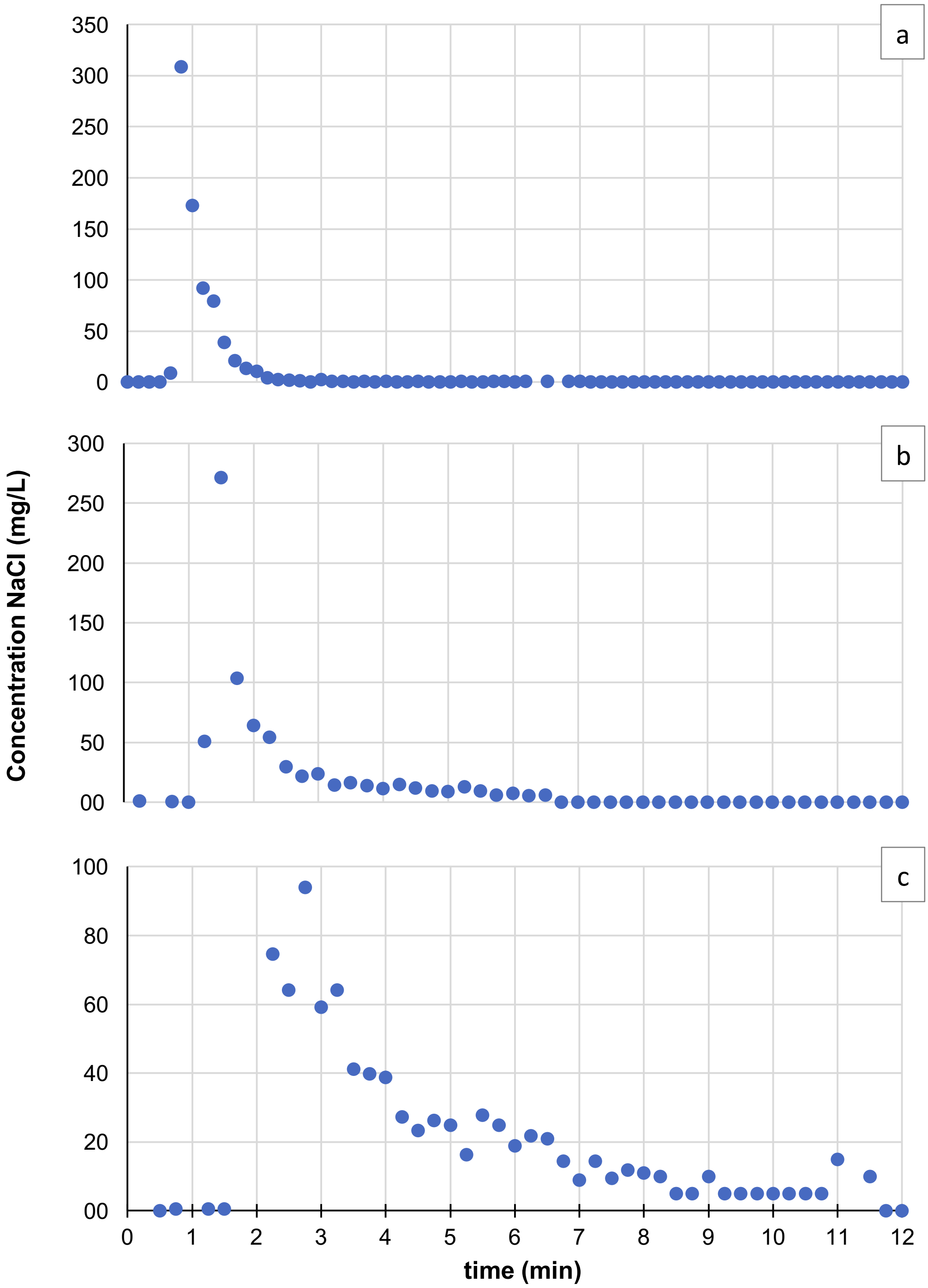

Figure 4.10: Experimental C curve for high (a), medium (b) and low (c) flow rate conditions obtained from tracer tests. The same time scale was used for all three plots.

Following the procedure described in chapter 3, the mean residence time was computed for all three experimental conditions: 1.11 min, 2.34 min and 4.64 min for high, medium and low flow rates, respectively. With these values, the normalized concentrations were obtained:115.0 mg/L, 81.87 mg/L and 45.76 mg/L for high, medium and low flow rates, respectively. The E and F curves were then plotted using the normalized times and concentrations, all computed values can be found in Appendix D together with the data collected from the tracer tests. The RTDs and F curves of each flow condition are reported in Figure 4.10.

4.2.2.2
Tanks-in-series conceptual model

Several attempts were made to obtain the E and F curves that better approximate the experimental curves by changing the parameters of the tank-in-series model, explained in chapter 3. Results of the many tested models are not reported in this work. Ultimately, a system with 2 parallel lines (L1 and L2) and a total of 8 tanks was chosen, taking into consideration the summation of the quadratic difference of the F values of the tracer test and the conceptual model. The specific characteristics of the system set-up for each flow rate are listed in Table 4.4. All values computed are reported in Appendix E and plots of the experimental and modelled E and F curves are shown in Figure 4.11.

The flow rate determined the fractions of flow (α) and volume (β) that go into each treatment line, but the repartition of these parameters followed the same concept, with L2 receiving a significantly higher amount of flow rate (83-94%) and 65% of the volume. In terms of the F curve, increasing the number of tanks (N) reproduced the initial part of the curve, where no concentrations of NaCl were detected, as well as the immediate increase and reaching of the maximum. Opting for a second line with one tank and much lower flow rate delayed reaching the maximum, resulting in a more gradual growth as the F curve approaches 1. Although relatively complex, the chosen configuration proved to be the better option when compared to simpler models. This was particularly true for the complicated hydrodynamics of the low flow rate condition.

Table 4.4: Parameters selected for the tank-in-series conceptual model for the three flow rate conditions.

	High		**Medium**		**Low**	
Parameter	**L1**	**L2**	**L1**	**L2**	**L1**	**L2**
α	0.06	0.94	0.17	0.83	0.17	0.83
β	0.35	0.65	0.35	0.65	0.35	0.65
N	1	7	1	7	1	7
Q (L/h)	14	226	21	99	10	50
V (L)	1.89	3.51	1.89	3.51	1.89	3.51
t (min)	7.88	0.93	5.45	2.12	11.22	4.22

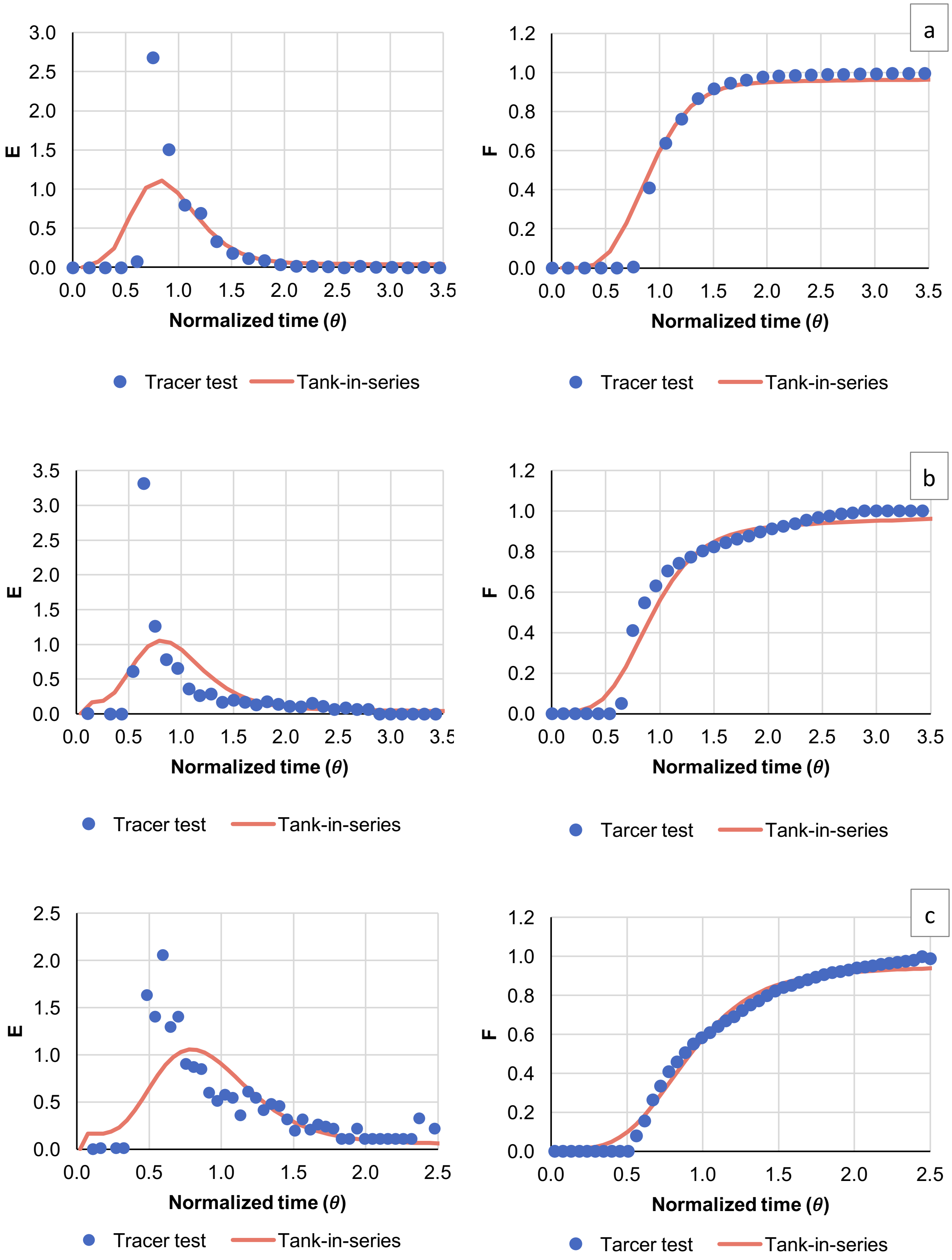

Figure 4.11: E(θ) curve (left) and F (θ) curve (right) for high (a). medium (b) and low (c) flow rate conditions of the tracer test results and tank-in-series conceptual model.

A lag time of 0.1 min was introduced to the modelled curves, to consider the time required for activating the pump and for the fluid to go through the inlet pipe, which are not accounted for by the analytical model. The same equipment was used to perform the experimental tests; therefore, the lag time was considered to be the same for the three flow rate conditions. In this way, the E and F curves are slightly shifted to the right and better resemble the tracer test curve.

The conceptual model showed good agreement with the tracer test curves for all three flow rates, however, resulting in better matching for the high flow rate condition (Figure 4.11a). It becomes apparent from the curves that the model is not capable of recreating the initial exponential growth with the steepness shown by the experimental results. Instead, the tank-in-series curve shows a more gradual increase of the concentration of NaCl, consequently reaching peak point later.

4.2.2.3
ANSYS FLUENT simulations

The particle tracking tool provides results in terms of F curve without time normalization. Modelling results are shown in Figure 4.12. For this reason, comparisons between the experimental tracer tests, the tank-in-series conceptual model and the simulation (FLUENT PT) were made considering the non-normalized F curve (Figure 4.13). The data used for the plots is reported in Appendix F. The F curves obtained by means of simulation with the RKE model, showed behavior consistent with that expected for the hydrodynamic of the reactor in study at the different operational conditions. As particles travel faster inside the reactor, the high flow rate curve reached maximum point earlier than for the other two conditions, in less than a minute, and with a much steeper angle. Meanwhile, the lower flow rate curve takes up to 11 min to reach maximum point with a softer growth. The medium curve shows a closer behavior to that of the high flow rate condition, with a slightly higher inclination.

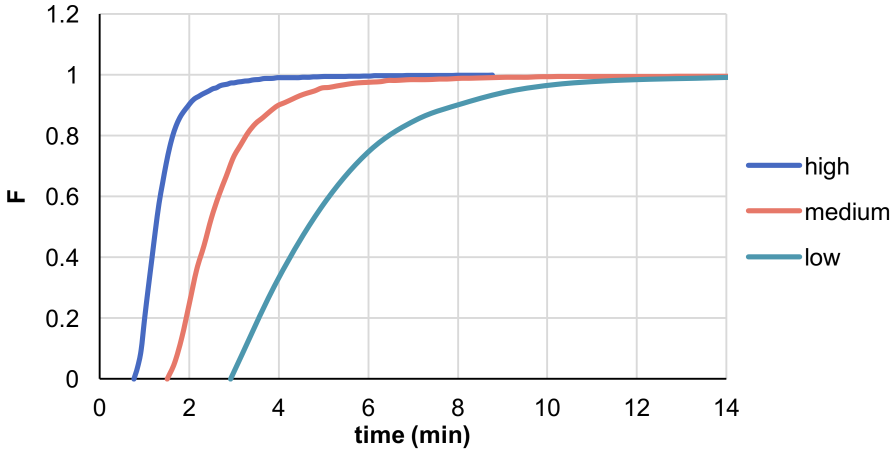

Figure 4.12: Simulated F curve for high, medium and low flow rate conditions using RKE turbulence model.

Unlike the conceptual model, an initial comparison with the experimental results showed that the simulated curves accurately predicted the time required for first particles to reach the outlet of the reactor. Therefore, no implementation of lag time was required. The steepness of the initial growth was, however, slightly underpredicted, increasing in difference with the decrease of the flow rate. This observation prompted a brief study of two additional turbulence models, RSM and Laminar, for the medium and low flow rates. The F curves obtained using the different models were plotted against the experimental F curve, the results can be seen in Figure 4.13.

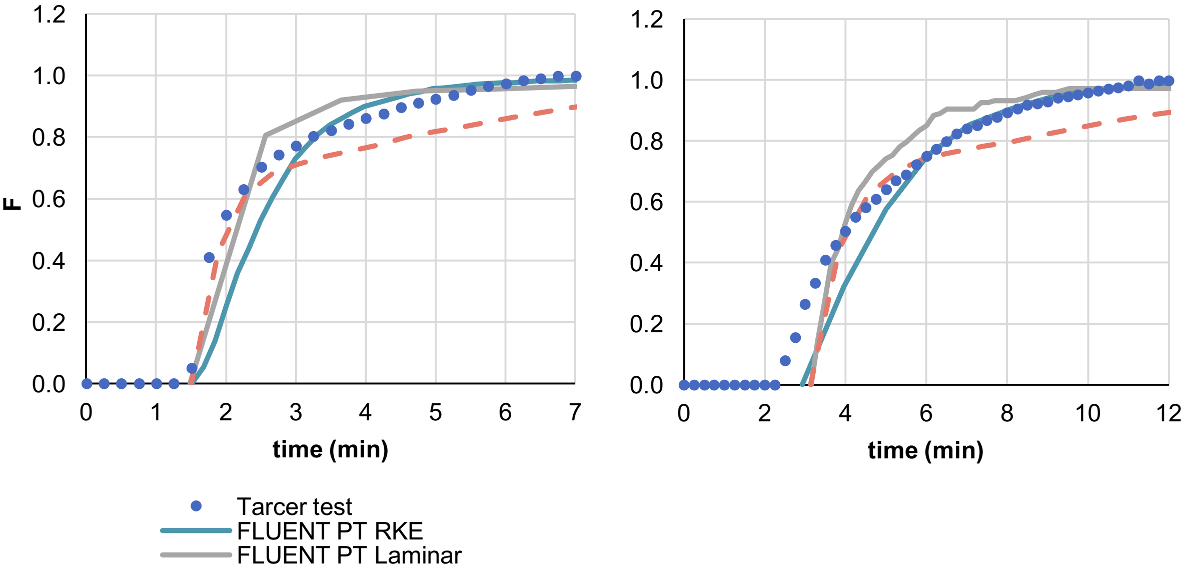

Figure 4.13: Simulated F curve for medium (left) and low (right) flow rate conditions with the use of the RKE, Laminar and RSM turbulence models.

The initial increase for the laminar curves was steeper even surpassing the experimental ones. The RSM model showed better agreement of results for the first 2.5 min, but the gradual decrease in growth rate was considerably faster. In the end, the RKE proved to show overall better approximations for all three operational conditions while maintaining a low computational cost. To account for the difference in steepness and achieve closer resemblance to the experimental curves, the RKE were displaced to the left by 15 s.

In the case of the high flow rate curves (Figure 4.14a), the simulated results satisfactorily approach the overall shape of the experimental solution. However, the FLUENT PT curve begins to increase the concentration of NaCl almost half a minute earlier. The 15 s displacement served to make the curves closer at the inflection point. At peak point the simulated curve slightly under predicts the experimental results. The tank-in-series model and the FLUENT PT simulation show very similar results, with some slight differences in the beginning and in the end of the curves. The conceptual curve has a flatter shape that results in an earlier initial growth and a later peak point reach.

For the medium flow rate (Figure 4.14b) both the FLUENT PT and the experimental curves begin to grow at around 1.5 minutes, after introducing the 15 s. However, the tracer test curve grows steeper than the simulated one. In this case, it was opted not to make the curves closer at the inflection point to maintain a more general proximity to the tracer test curve. The experimental curve shows a steeper growth from minute 1.5 to 2.5, approximately. While the FLUENT PT simulation has a smoother growth before reaching the peak point, in this way resembling better the behavior of the end of the experimental curve. Similar observations made for the high flow rate, when comparing the conceptual and the simulated curves, can be made for the medium condition, with differences in the middle section becoming apparent.

The low flow rate curves (Figure 4.14c) confirm the use of particle tracking as an accurate tool when simulating the hydrodynamic behavior of the reactor. The experimental curve begins to grow somewhat earlier even after the 15 s displacement. The FLUENT PT simulation shows a softer curve that yet approximates the behavior of tracer test curve correctly. The already mentioned differences between the tank-in-series model and the FLUENT PT continued to accentuate with the decrease of the flow rate.

Overall, the plots show that the high flow rate condition was better approximated by both the conceptual model and the simulation. As the flow rate decreases, the tank-in-series curves are not as satisfactory as the FLUENT simulation. These may be due to the incapacity of the conceptual model to reproduce the non-ideal behavior of the flow inside the reactor that become more relevant as the velocity of the flow decreases. Therefore, for the three flows the ANSYS FLUENT simulations show a more accurate representation of the experimental tracer test.

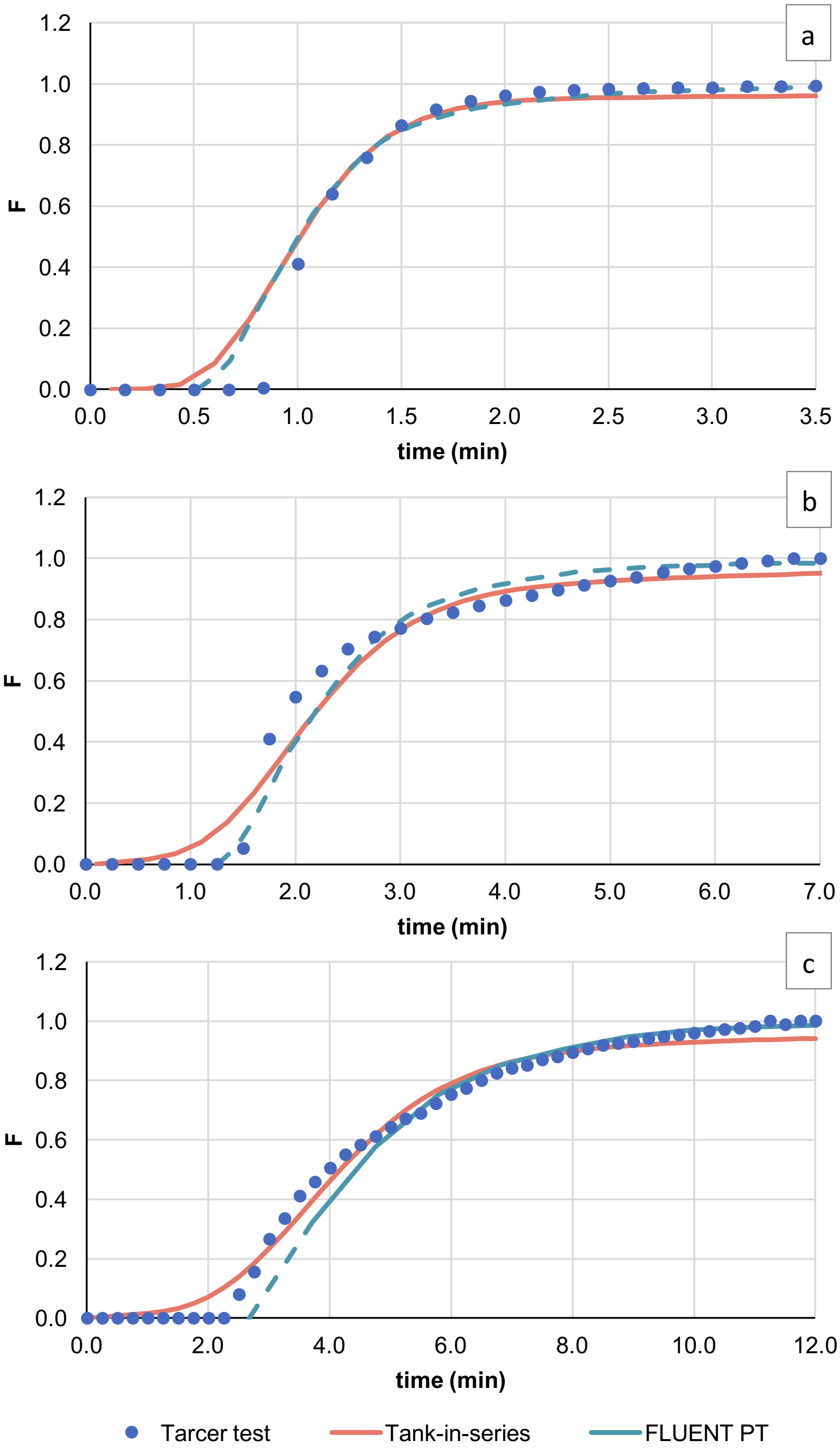

Figure 4.14: F curve for high (a), medium (b) and low (c) flow rate condition for tracer test results, tank-in-series conceptual model and FLUENT PT simulations.

4.3
UV dose distribution

The UV dose distribution of the GW, SS and GR WWTP are reported in Figure 4.15 for the three flow rates. GR WWTP results are plotted in a separate histogram together with GW to facilitate visualization and comparison. Each rectangle represents the percentage of the particles injected (y axis) during the simulation that received the corresponding UV intensity (x axis). These can be considered as single elements and their summation accounts for the overall UV dose absorbed by the water matrix.

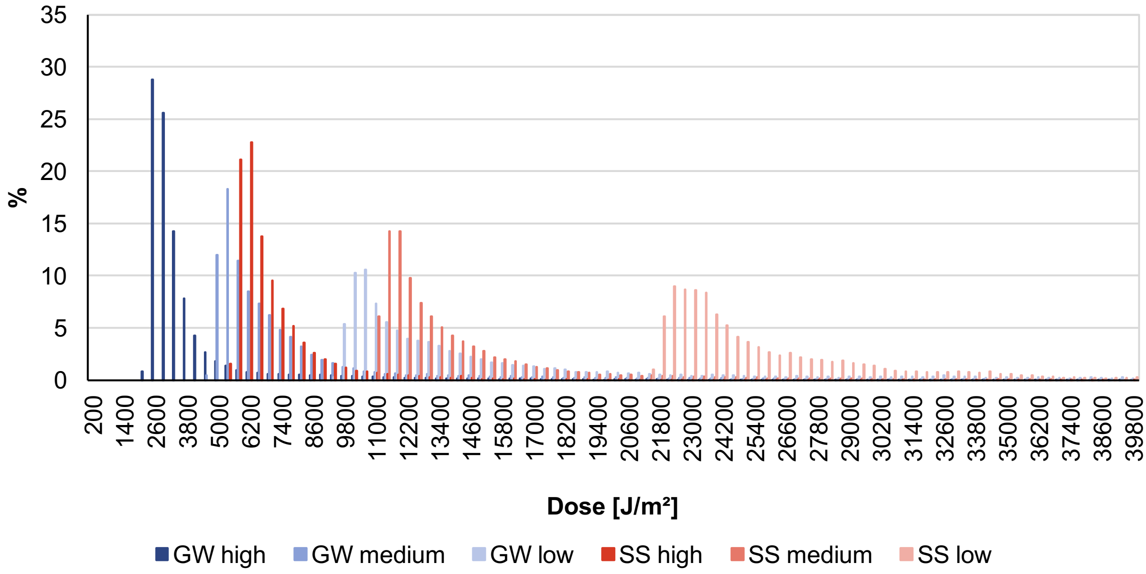

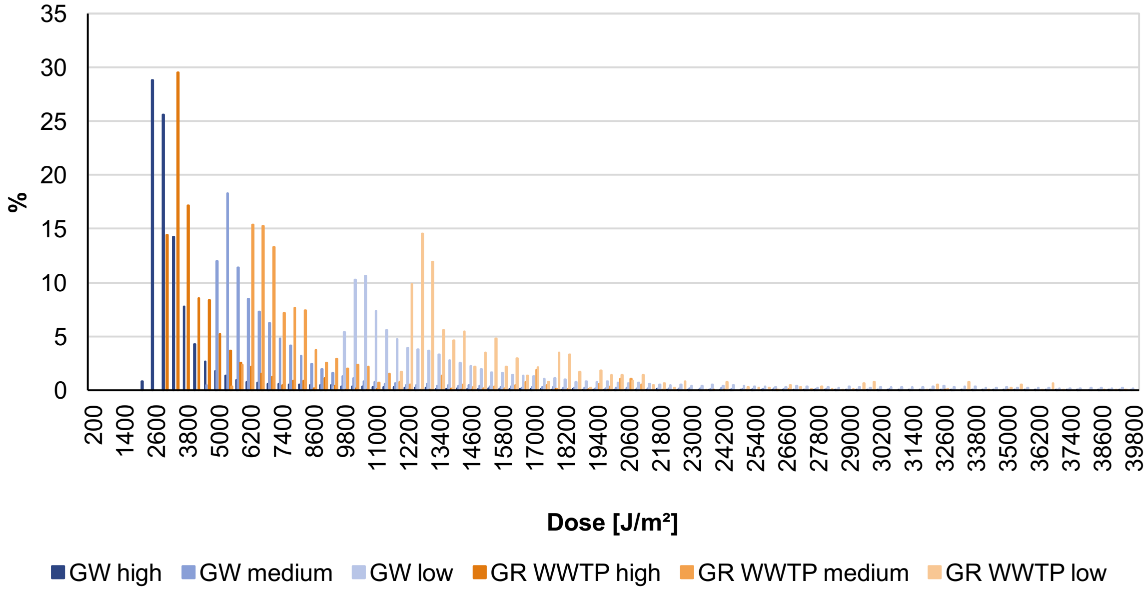

Figure 4.15: UV dose (J/ m^2) distributions for GW (top and bottom), SS matrices (top) and GR WWTP (bottom) in high, medium and low flow rate.

The distributions followed a left-modal bell-shaped curve with positive skewedness, meaning that only a small fraction of particles was exposed to the lower UV radiations and the average received the doses on the higher end. As the flow rate decreased, so did the peak of the curves and the left side of the tail slightly fattened. In other words, the distribution of the UV dose behaved more uniformly. This behavior is due to the increased residence time of the particles at lower flow rates, that resulted in (1) higher absolute values of UV radiation received and (2) particles having more time to interact with the UV light and absorb a more consistent UV dose.

The UV dose distributions of the GW are shifted to the left in comparison to the SS distributions. This means that when the photoreactor is filled with GW, particles going through receive lower values of UV radiation than for the SS. These results are in agreement with the radiation profiles presented in the fluence rate section of this chapter, where a significant reduction of the radiation along the reactor radius was observed for the GW compared to the SS. Likewise the radiation profiles, this is attributed to the higher water matrix absorbance of the GW, that results in overall less UV radiation available for the particles injected.

The same procedures of simulation were repeated for the GR WWTP matrix and the overall UV doses absorbed (Table 4.5) were computed following the procedure described in chapter 3. As expected, the total UV dose absorbed by the matrix decreases the higher the absorbance, with SS absorbing the most and GW the least. GR WWTP instead, absorbed more than GW but considerably less than SS. Proving conclusion (2), the difference between two water matrices with relatively similar absorbance is not significant for the high flow rate (4,284.04 J/m^2 for GW and 4,355.92 J/m^2 for GR), however, as the flow rate decreases the difference becomes more evident reaching a gap of 755 J/m^2 between the two matrices at low flow rate. Therefore, if we consider these particles to be H_2O_2, at lower flow rates there would be a significant increase of OH• radicals production, limited by the absorbance of the water. For instance, the number of particles that absorb this increase in the GW is less than that of GR.

Table 4.5: Overall UV dose absorbed by the particles in all water matrices for the three flow rate conditions.

Water matrix	High	Medium	Low	Unit	ABS
GW	4,284.04	8,213.99	15,308.59	[J/m²]	0.33
GR WWTP	4,355.92	8,783.84	16,064.02	[J/m²]	0.25
SS	7,366.43	14,256.60	25,571.16	[J/m²]	0.01

4.4
Kinetic model

Outlet concentration of the pharmaceuticals obtained from the experimental tests and with CDF modelling are reported in Table 4.6 As previously stated, only the operational condition of [H_2O_2] = 15 mg/L and Q = 120 L/h (experiment 5) was modelled with the kinetic model. For all five pharmaceuticals, results show overall good agreement between lab collected and modelled data in the three water matrices. The modelled tended to slightly underestimate the outlet concentration, resulting in higher removal percentages (Table 4.6), which were computed using the inlet concentrations found experimentally.

Table 4.6: Pharmaceutical outlet concentration (mol/L) and removal percentage for the GW, GR WWTP and SS water matrices at [H_2O_2] = 15 mg/L and Q = 120 L/h found experimentally (E) and modelled (M).

		GW		**GR WWTP**		**SS**	
Pharmaceutical		**Cout**	**Removal**	**Cout**	**Removal**	**Cout**	**Removal**
Ibuprofen (IBU)	E	1.53E-07	16.3%	6.10E-08	51.3%	2.42E-09	98.1%
	M	1.30E-07	28.9%	5.60E-08	55.2%	0.00E+00	100%
Metoprolol (MTP)	E	1.01E-07	13.5%	5.14E-08	50.9%	1.87E-09	97.8%
	M	8.65E-08	25.6%	4.86E-08	53.6%	0.00E+00	100%
Sulfamethoxazole (SMX)	E	8.66E-09	94.4%	1.24E-08	89.4%	1.97E-09	98.3%
	M	0.00E+00	100.0%	9.39E-09	92.0%	0.00E+00	100%
Carbamazepine (CBZ)	E	9.55E-08	1.20%	4.78E-08	50.3%	2.12E-09	98.2%
	M	8.67E-08	10.3%	4.81E-08	50.0%	0.00E+00	100%
Venlafaxine	E	8.51E-08	17.8%	5.12E-08	53.7%	1.80E-09	97.7%
	M	6.87E-08	33.6%	5.42E-08	51.0%	0.00E+00	100%

Figure 4.16 plots the difference of pharmaceutical removal between the experimental and modelled data. For GR WWTP and SS, removal percentages were more accurately predicted by the model, while for GW the overestimation becomes more significant reaching up to 15% difference. This can be attributed to the model not being able to consistently reproduce the influence of higher DOC concentrations. Another possible explanation is related to the UV radiation profiles and the CF_i introduced to account for FLUENT overall overestimation of the fluence rate. Due to their proximity in absorbance, GW (ABS = 0.33) and GR WWTP (ABS = 0.25) were attributed the same value of CF_i = 0.95 (Table 3.3). It is very likely the irradiation profile was more sensible to small changes of CF_i than considered, thus applying

the same CF_i for GW and GR WWTP, instead of using a greater one, resulted in a slight overestimation of the fluence rate of GW and, consequently, that of the UV dose distribution and dose. The higher UV dose ultimately caused an increase in the removal of the pharmaceuticals.

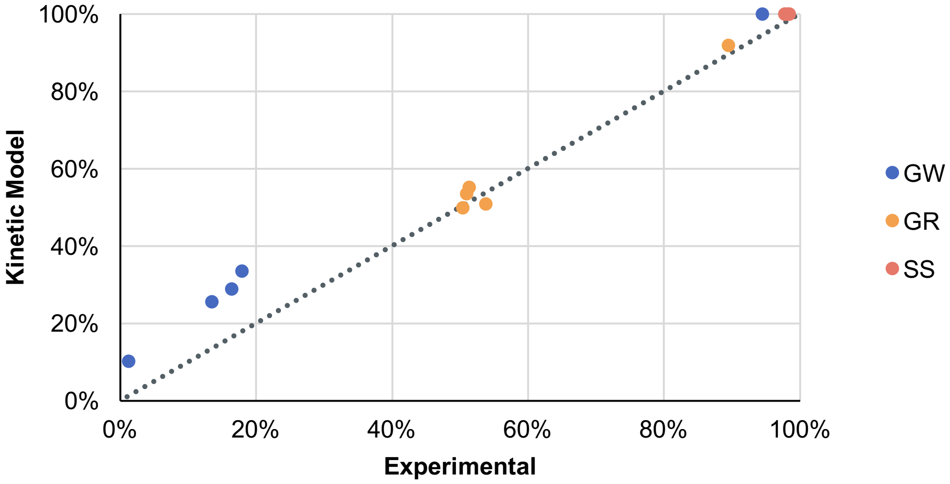

Figure 4.16: Removal percentage comparison between experimental and modelled data for the three water matrices at [H_2O_2] = 15 mg/L and Q = 120 L/h.

Figure 4.17 compiles lab collected results of experiments without H_2O_2 addition and with [H_2O_2] = 15 mg/L (experiments 4 and 5 of Table 3.5, respectively), together with the modelled data. Experimental data showed a significant increase in removal of contaminants with the addition of the H_2O_2. An exception was observed for SMX that achieved almost complete removal from the photolysis alone, this is consistent with the higher ε_i of SMX.

Even without H_2O_2 addition, removal fractions showed an increasing behavior from GW to GR and SS, proving once more the absorbance of the water as a significant parameter that influences the reactor performance. Moreover, the gap between the water matrices became more apparent with addition of H_2O_2, meaning that as less radiation is available due to the higher water absorbance the efficiency of OH• radicals production decreases. GW and GR WWTP were also characterized by higher concentration of carbonate species that are OH• radicals scavengers.

Lastly, Figure 4.17 ilustrates, once again, the satisfactory results yielded by the kinetic model, in particular, for GR WWTP and SS matrices. Taking into account the observations made on the influence of the CF_i for GW, the model can be considered to have good applicability with the predicted degradations within 5 to 15% of the measured removals.

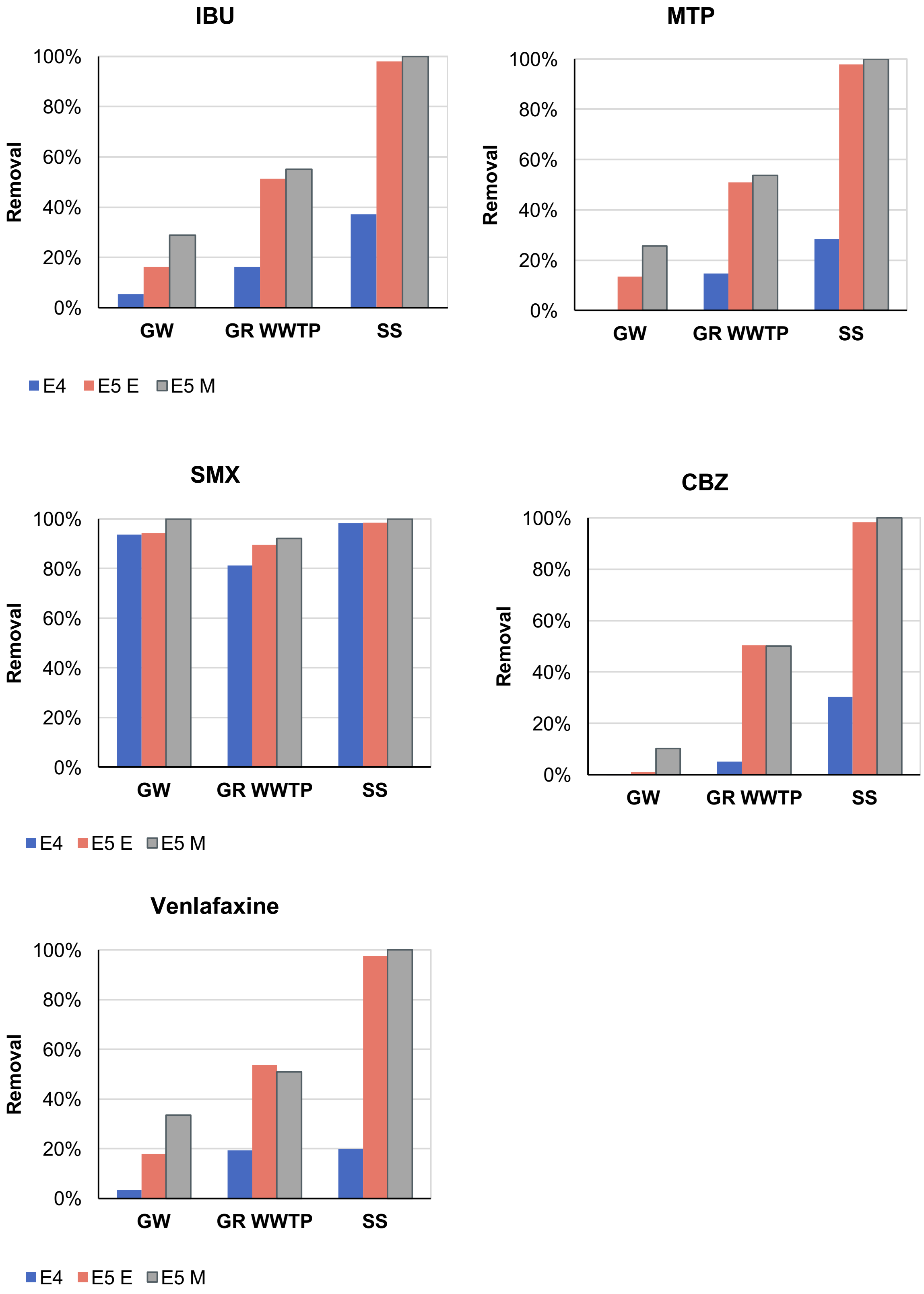

Figure 4.17: Removal percentage of the UV/H_2O_2 process collected experimentally for the three water matrices at $[H_2O_2] = 0$ mg/L (E4) and $[H_2O_2] = 15$ mg/L (E5) with Q = 120 L/h and modelled data with $[H_2O_2] = 15$ mg/L (E5 M).

5
CONCLUSION AND FUTURE DEVELOPMENT

AOP systems are becoming more relevant as new anthropic contaminants emerge. UV/H_2O_2 processes, in particular, are being studied for full scale applications thus bringing attention to the factors that affect the performance of this technology.

The present work aimed to assess the influence that physicochemical characteristics of the water matrices may present in UV/H_2O_2 AOPs for EOC removal using ANSYS FLUENT for CFD. Experimental data was collected from three water matrices of different origins. A model was developed to simulate the photoreactor that consisted of a geometric mesh of the reactor, a description of the fluid dynamic conditions, and a UV radiation model. These allowed to obtain a UV dose distribution using particle tracking that were imported into the kinetic model for evaluation of the contaminant removal.

Experimental data were used to validate the fluid dynamics of the reactor and results showed that the computational model was able to successfully reproduce the velocity fields. In the case of the residence time distributions, the simulations using RKE turbulence model yielded good results for all three flow rates, with small inconsistencies as the flow rate decreased. In fact, the simulated results were able to better reproduce the fluid dynamic behavior than the developed tank-in-series conceptual model.

The fluence rate distribution was predicted using a DO model embedded in the software. From the irradiation profiles, it became apparent that the absorbance of the water matrix presented a significant influence. Modelled and experimental data of irradiation were not compared in the present work because, according to the literature, the DO model tends to overestimate the irradiation values. Instead, calibration factors taken from the literature were used to obtain more accurate results. Moreover, the LVRPA of the GW and SS was studied for different inner wall diffuse reflection values and proved these to be relevant for lower absorbance matrices.

The UV dose distribution in a set of inert particles was simulated to deeper understand the influence of the water matrix absorbance. Results showed that particles entering water matrices with lower absorbance were capable of receiving a higher UV dose than those in water matrices with higher values. Moreover, lowering the flow rate in the reactor results in higher UV doses absorbed and a more uniform distribution of the UV dose. This behavior is explained by the increased residence time of the particles, meaning that particles have more time to interact with the UV light and absorb a more consistent UV dose.

The kinetic model elaborated for chemical degradation prediction resulted in good applicability to the case in study. Removal percentages significantly increased with the addition of H_2O_2, proving UV/H_2O_2 AOP a useful technology to increase the efficiency of contaminant removal. Results also pointed to the negative influence of water absorbance as well as the presence of light absorbing species. Future investigations could be performed on the influence of the flow rates to degradation.

Therefore, with the use of CFD it was possible to successfully assess the fluid dynamic and radiation behavior and predict contaminant removal of a UV/H_2O_2 reactor. The different models can be tailored to fit innumerous specifics of reactor configuration, operational conditions and water characteristics. In this way, allowing to optimize design and operation while reducing experimental labor, time consumption and costs.

6
REFERENCES

ALPERT, S.M.; KNAPPE, D.R.U.; DUCOSTE, J.J. **Modeling the uv/hydrogen peroxide advanced oxidation process using computational fluid dynamic**s. Water Research 44 (6), 1797-1808, 2010.

ALPERT, S.M.; KNAPPE, D.R.U.; DUCOSTE, J.J. **Evaluation of Computational Fluid Dynamics for Modeling UV-Initiated Advanced Oxidation Processes**. Water Research Foundation, Web Report #3176, 2011.

AUDENAERT, W.T.M.; VERMEERSCH, Y.; HULLE S.W.H.; DEJANS, P.; DUMOULIN, A.; NOPENS, I. **Application of a mechanistic UV/hydrogen peroxide model at full- scale: sensitivity analysis, calibration and performance evaluation**. Chem. Eng. J. 171 (1) 113–126, 2011.

ANSYS. **ANSYS FLUENT 15.0 Theory Guide**. ANSYS Inc., Canonsburg, PA, USA, 2013.

ANSYS. **ANSYS FLUENT 12.0 User's Guide**. Available at < https://www.afs.enea.it/project/neptunius/docs/fluent/html/ug/main_pre.htm>. ANSYS Inc., 2009.

ANTONELLI, M. **Trattamento delle acque di approvvigionamento.** Corso di Laurea Magistrale in Ingegneria per l'Ambiente e il Territorio, Politecnico di Milano, lecture notes, 2015.

BAXENDALE, J.H.; WILSON, J.A. **The photolysis of hydrogen peroxide at high light intensities**. Trans. Faraday Soc. 53, 344e356, 1957.

BECK. **Detection of charged intermediate of pulse radiolysis by electrical conductivity measurements**. Int. J. Radiat. Phys. Chem. 1(3), 361-371, 1969.

BIELSKI, H. J.; BENON, H. J.; CABELLI D. E.; RAVINDRA L. A. and ALBERTA A. B. **Reactivity of perhydroxyl/ superoxide radicals in aqueous solution**. J. Phys. Chem. Ref. Data 14(4), 1041-100, 1985.

BOUSSINESQ, J. **Essai sur la théorie des eaux courantes**. Mémoires présentés par divers savants à l'Académie des Sciences, XXIII (1) pp. 1-680, 1877.

BUXTON, G. V.; GREENSTOCK, C. L.; HELMAN, W. P.; ROSS, A. B. **Critical review of rate constants for reactions of hydrated electrons, hydrogen atoms and hydroxyl radicals (•OH/•O− in aqueous solution.** Journal of physical and chemical reference data, 17(2), 513-886, 1988.

CASADO, C.; MARUGÁN, J.; TIMMERS R.; MUÑOZ, M.; GRIEKEN R. **Comprehensive multiphysics modeling of photocatalytic processes by computational fluid dynamics based on intrinsic kinetic parameters determined in a differential photoreactor**. Chemical Engineering Journal 310, 368-380, 2017.

CANONICA, S.; KOHN, T.; MAC, M.; REAL, F.J.; WIRZ, J.; VON GUNTEN, U. **Photosensitizer method to determine rate constants for the reaction of carbonate radical with organic compounds.** Environ. Sci. Technol. 39 (23), 9182e9188, 2005.

CELIK, I. B. **Introductory Turbulence Modeling**. Mechanical & Aerospace Engineering Department, West Virginia University, lecture notes, 1999.

CHRISTENSEN, G. M.; OLSON, D.; RIEDEL, B. **Chemical effects on the activity of eight enzymes: A review and a discussion relevant to environmental monitoring**. Environmental research, 29(2), 247-255, 1982.

CRITTENDEN J. C.; HU, S.; HAND, D.W.; GREEN, S. A. **A kinetic model for H2O2/UV process in a completely mixed batch reactor.** Water Research 33 (10) 2315-2328, 1999.

CRITTENDEN J. C.; TRUSSELL, R. R.; HAND, D.W.; HOWE, K. J.; TCHOBANOGLOUS, G. **MWH's water treatment: principles and design, third edition.** John Wiley & Sons, Inc. Hoboken, New Jersey, 2012.

DRAGANIC, Z.D.; NEGRN-MENDOZA, A.; SEHESTED, K.; VUJOSEVIC, S.I.; NAVARRO-GONZALES, R.; ALBARRN-SANCHEZ, M.G.; DRAGANIC, I.G. **Radiolysis of aqueous solutions of ammonium bicarbonate over a large dose range**. Int. J. Radiat. Appl. Instrum. C. Radiat. Phys. Chem. 38 (3), 317e321, 1991.

ELYASI, S.; TAGHIPOUR, F. **Simulation of UV photoreactor for degradation of chemical contaminants: model development and evaluation**. Environ. Sci. Technol. 44 (6), 2056-2063, 2010.

EPA. **The history of drinking water treatment.** Environmental Protection Agency, Office of Water (4606), Fact Sheet EPA-816-F-00-006, United States, 2000.

GLAZE, W. H.; LAY, Y.; KANG, J. W. **Advanced oxidation processes. A kinetic model for the oxidation of 1,2 dibromo-3-chloropropane in water by the combination of hydrogen peroxide and UV radiation.** Ind. Eng. Chem. Res 34, 2314-2323, 1995.

HO, C. K.; KHALSA, S. S.; WRIGHT H. B.; WICKLEIN, E. **Computational Fluid Dynamics Based Models for Assessing UV Reactor Design and Installation.** Water Research Foundation, Web Report #4107, 2011.

HO, C. K. **Radiation Dose Modeling in FLUENT.** WEF Disinfection 2009 Workshop: Modeling UV Disinfection using CFD, Sandia National Laboratories, Albuquerque, NM, 2009.

HUIE, R.E.; CLIFTON, C.L. **Temperature dependence of the rate constants for reactions of the sulfate radical, SO_4 , with anions**. J. Phys. Chem. 94 (23), 8561e8567, 1990.

KOPPENOL, W. H.; BUTLER, J.; LEEUWEN, J. W. V. **The Haber-Weiss cycle**. Photochemistry and Photobiology, 28(4-5), 655-658, 1978.

LAY, Y. S. **Oxidation of 1,2-dibromo-3-chloropropane in groundwater using advanced oxidation processes**. Ph.D. dissertation, University of California, Los Angeles, 1989.

LEVENSPIEL, O. **Chemical reaction engineering third edition**. John Wiley & Sons, Inc., 1999.

LI, K.; HOKANSON, D. R.; CRITTENDEN, J. C.; TRUSSELL, R. R.; MINAKATA, D. **Evaluating UV/ H_2O_2 processes for methyl tert-butyl ether and tertiary butyl alcohol removal? Effect of pretreatment options and light sources**. Water Research 42, 5045-5053, 2008.

LI, W.; LI, M.; BOLTON, J. R.; QU, J.; QIANG, Z. **Impact of inner-wall reflection on UV reactor performance as evaluated by using computational fluid dynamics: The role of diffuse reflection**. Water Research 109, 382-388, 2017.

LIU, D.; DUCOSTE, J. J.; JIN, S.; LINDEN, K. **Evaluation of alternative fluence rate distribution models.** Aqua J. Water Supply Res. Technol. 53 (6), 391e408, 2004.

MAZELLIER, P.; LEROY, E.; LAAT, J.; LEGUBE, B. **Transformation of carbendazim induced by the H2O2/UV system in the presence of hydrogenocarbonate ions: Involvement of the carbonate radical**. New J. Chem. 26 (12) 1784–1790, 2002.

MODEST, M. F. **Radiative heat transfer (third edition)**. Academic Press, chapter 10 (279-302) and chapter 17 (541-548), 2013.

MOHAJERANI, M.; MEHRVAR, M.; EIN-MOZAFFARI, F. **CFD modeling of metronidazole degradation in water by the uv/ H2O2 process in single and multilamp photoreactors**. Ind. Eng. Chem. Res. 49 (11), 5367-5382, 2010.

MONTECCHIO, F. Process **Optimization of UV-Based Advanced Oxidation Processes in VOC Removal Applications.** KTH Royal Institute of Technology School of Engineering Sciences in Chemistry, Biotechnology and Health, Department of Chemical Engineering. Stockholm, Sweden, 2018.

NETA, P.; HUIE, R.E.; ROSS, A.B. **Rate constants for reactions of inorganic radicals in aqueous solution**. J. Phys. Chem. Ref. Data 17 (3), 1027e1284, 1988.

PAL, A.; GIN, K. Y. H.; LIN, A. Y. C.; REINHARD, M. **Impacts of emerging organic contaminants on freshwater resources: Review of recent occurrences, sources, fate and effects**. Science of the Total Environment 408, 6062-6069, 2010.

PERRY, R.; GREEN, D.; MALONEY, J. **Perry's Chemical Engineerings' Handbook, fifth ed.** McGraw-Hill, New York, 1981.

PEYTON, G. R. **Guidelines for the selection of a chemical model for advanced oxidation processes**. A symposium on advanced oxidation processes for the treatment of contaminated water and air (proceedings). Toronto 1990.

RODI, W. **Turbulence models and their application in hydraulics**. 3rd Ed., Balkema, Rotterdam, The Netherlands, 1993.

SANDIA NATIONAL LABORATORIES. **UV Disinfection**. Available at < https://www.sandia.gov/cfd-water/uvdisinfection.htm>. 2009.

SANTORO, D.; RAISEE, M.; MOGHADDAMI, M.; DUCOSTE, J.; SASGES, M.; LIBERTI, L.; NOTARNICOLA, M. **Modeling hydroxyl radical distribution and trialkyl phosphates oxidation in uv e H2O2 photoreactors using computational fluid dynamics.** Environ. Sci. Technol. 44 (16), 6233-6241, 2010.

SEHESTED, K.; RASMUSSEN, O. L.; FRICKE H. **Rate constants of OH with HO2,O2- and H2O+2 from hydrogen peroxide formation in pulse-irradiated oxygenated water**. J. Phys. Chem. 72, 626-631, 1968.

SHARPLESS, C.; LINDEN, K. **Experimental and model comparisons of low- and medium-pressure Hg lamps for the direct and H2O2 assisted UV photodegradation of N-Nitrosodimethylamine in simulated drinking water.** Environ. Sci. Technol. 37 (9) 1933–1940, 2003.

SOMMER, R.; CABAJ, A.; HAIDER, T. **Microbicidal effect of reflected UV radiation in devices for water disinfection**. Water Sci. Technol. 34 (7_8), 173e177, 1996.

SONG, W.; COOPER, W.J.; MEZYK S.P.; GREAVES, J.; PEAKE, B.M. **Free radical destruction of beta-blockers in aqueous solution**. Environ. Sci. Technol. 42 (4) 1256–1261, 2008.

SOZZI, D. A.; and TAGHIPOUR, F. **UV reactor performance modeling by Eulerian and Lagrangian methods**. Environ. Sci. Technol. 40 (5), 1609e1615, 2006.

STEFAN, M. I.; HOY, A. R; BOLTON, J. R. **Kinetics and mechanisms of the degradation and mineralization of acetone in dilute aqueous solution sensitized by the UV potolysis of hydrogen peroxide.** Environ. Sci. Technol. 30, 2382-2390, 1996.

SYSTEM SE. **The UV/oxidation handbook**. Markham, Ont. Canada; Las Vegas, Nev., 1994.

VIONE, D.; FALLETTI, G.; MAURINO, V.; MINERO, C.; PELIZZETTI, E.; MALANDRINO, M.; AJASSA, R.; OLARIU, R.I.; ARSENE, C. **Sources and sinks of hydroxyl radicals upon irradiation of natural water samples.** Environ. Sci. Technol. 40 (12), 3775e3781, 2006.

VISKANTA, R.; and MENGÜÇ, M. P. **Radiation heat transfer in combustion systems**. Progress in Energy and Combustion Science, vol. 13, 97–160, 1987.

VOLMAN, D.H.; CHEN, J.C. **The photochemical decomposition of hydrogen peroxide in aqueous solutions of allyl alcohol at 2537**. J. Am. Chem. Soc. 81 (16), 4141e4144, 1959.

WEINSTEIN, J., & BIELSKI, B. H. **Kinetics of the interaction of perhydroxyl and superoxide radicals with hydrogen peroxide**. **The Haber-Weiss reaction.** Journal of the American Chemical Society, 101(1), 58-62, 1979.

WOLS B. A.; HOFMAN-CARIS, C.H.M. **Modelling micropollutant degradation in uv/H2O2 systems: Lagrangian versus Eulerian method.** Chem. Eng. J. 210, 289-297, 2012.

WOLS B. A.; HARMSEN, D. J. H.; BEERENDONK, E.F.; HOFMAN-CARIS, C.H.M. **Predicting pharmaceutical degradation by uv (lp)/H2O2 processes: a kinetic model.** Chem. Eng. J. 255, 334-343, 2014.

WOLS B. A.; HARMSEN, D. J. H.; WANDERS-DIJK, J.; BEERENDONK, E.F.; HOFMAN-CARIS, C.H.M. **Degradation of pharmaceuticals in UV (LP)/H2O2 reactors simulated by means of kinetic modeling and computational fluid dynamics (CFD).** Water Research 75 11-24, 2015.

APPENDIX A – UDF for turbulent velocity profile

```
/**********************************************************************/
/*                    UDF for turbulent velocity profile              */
/**********************************************************************/

#include "udf.h"
#define ZC 1.051
#define R 0.0125
#define UMEAN 0.136

DEFINE_PROFILE(velocity_profile, t, i )
{
   real n[ ND_ND ];
   real x;
   real z;
   real r;
   face_t f;

   begin_f_loop( f, t )
   {
   F_CENTROID( n, f, t );
   y = n[1];
   z = n[2];
   r = sqrt( pow( ( y-YC ), DUE) + pow( ( z-ZC ), DUE ) );
   F_PROFILE( f, t, i ) = M*UMEAN*pow( ( ( R-r )/R ), B );
   }
   end_f_loop( f, t )
}
```

APPENDIX B – Inlet velocity profiles

	Low		Medium		High	
r	**FLUENT**	**Analytical**	**FLUENT**	**Analytical**	**FLUENT**	**Analytical**
-0.0124	0.0000	0.0009	0.0000	0.0017	0.0000	0.0034
-0.0124	0.0004	0.0013	0.0008	0.0025	0.0017	0.0051
-0.0123	0.0008	0.0017	0.0017	0.0034	0.0035	0.0067
-0.0112	0.0124	0.0130	0.0257	0.0260	0.0534	0.0521
-0.0112	0.0126	0.0132	0.0260	0.0263	0.0541	0.0527
-0.0111	0.0142	0.0148	0.0295	0.0297	0.0614	0.0594
-0.0105	0.0180	0.0204	0.0370	0.0408	0.0759	0.0816
-0.0094	0.0244	0.0294	0.0496	0.0588	0.1002	0.1176
-0.0085	0.0305	0.0365	0.0613	0.0730	0.1225	0.1459
-0.0073	0.0395	0.0450	0.0787	0.0900	0.1565	0.1800
-0.0071	0.0411	0.0464	0.0817	0.0927	0.1623	0.1855
-0.0064	0.0462	0.0502	0.0915	0.1004	0.1815	0.2008
-0.0060	0.0489	0.0526	0.0967	0.1051	0.1917	0.2102
-0.0049	0.0540	0.0578	0.1072	0.1155	0.2135	0.2310
-0.0037	0.0592	0.0619	0.1178	0.1238	0.2355	0.2476
-0.0036	0.0597	0.0623	0.1188	0.1246	0.2376	0.2492
-0.0036	0.0597	0.0624	0.1189	0.1248	0.2378	0.2495
-0.0035	0.0601	0.0628	0.1196	0.1256	0.2392	0.2513
-0.0032	0.0606	0.0636	0.1208	0.1272	0.2416	0.2543
-0.0032	0.0607	0.0637	0.1209	0.1273	0.2419	0.2547
-0.0014	0.0640	0.0672	0.1277	0.1343	0.2554	0.2686
-0.0012	0.0640	0.0674	0.1278	0.1347	0.2556	0.2695
-0.0003	0.0643	0.0680	0.1283	0.1359	0.2565	0.2718
0.0006	0.0643	0.0679	0.1283	0.1357	0.2565	0.2714
0.0010	0.0641	0.0675	0.1280	0.1351	0.2561	0.2701
0.0015	0.0637	0.0670	0.1273	0.1340	0.2548	0.2681
0.0022	0.0628	0.0660	0.1255	0.1319	0.2513	0.2638
0.0031	0.0607	0.0639	0.1211	0.1278	0.2425	0.2556
0.0037	0.0594	0.0622	0.1183	0.1243	0.2367	0.2487
0.0047	0.0554	0.0582	0.1102	0.1165	0.2202	0.2329
0.0052	0.0534	0.0564	0.1060	0.1128	0.2113	0.2257
0.0052	0.0532	0.0562	0.1056	0.1125	0.2107	0.2249
0.0052	0.0531	0.0561	0.1054	0.1122	0.2101	0.2244
0.0057	0.0510	0.0541	0.1011	0.1081	0.2012	0.2162
0.0057	0.0509	0.0540	0.1010	0.1080	0.2010	0.2160
0.0059	0.0486	0.0527	0.0964	0.1053	0.1920	0.2107
0.0060	0.0484	0.0526	0.0962	0.1052	0.1915	0.2104

0.0074	0.0390	0.0444	0.0776	0.0888	0.1535	0.1776
0.0090	0.0279	0.0328	0.0565	0.0657	0.1129	0.1314
0.0091	0.0275	0.0322	0.0557	0.0644	0.1114	0.1289
0.0091	0.0275	0.0322	0.0556	0.0643	0.1113	0.1287
0.0092	0.0266	0.0310	0.0539	0.0620	0.1079	0.1240
0.0092	0.0265	0.0310	0.0538	0.0619	0.1078	0.1238
0.0093	0.0258	0.0300	0.0524	0.0599	0.1052	0.1199
0.0094	0.0255	0.0296	0.0517	0.0591	0.1038	0.1182
0.0095	0.0245	0.0284	0.0497	0.0569	0.1000	0.1138
0.0104	0.0185	0.0214	0.0379	0.0427	0.0773	0.0855
0.0105	0.0171	0.0197	0.0353	0.0394	0.0723	0.0789
0.0111	0.0132	0.0147	0.0275	0.0294	0.0573	0.0587
0.0112	0.0117	0.0132	0.0243	0.0264	0.0507	0.0527
0.0123	0.0007	0.0017	0.0015	0.0033	0.0032	0.0066
0.0124	0.0004	0.0013	0.0008	0.0025	0.0017	0.0051
0.0124	0.0000	0.0008	0.0000	0.0017	0.0000	0.0034

APPENDIX C – UDF for UV dosage along a particle trajectory

```
/************************************************************************/
/*                  UDF for computing the UV dosage along a particle trajectory                 */
/************************************************************************/

#include "udf.h"
#include "dpm.h"
#include "sg_disco.h"

#define fileuv "output.dpm"
#define C_DO(c,t)C_STORAGE_R_XV(c,t,SV_DO_IRRAD,0)

static real uv_intensity_0;
static real x0, y00, z0;

FILE *fuv;

DEFINE_DPM_SCALAR_UPDATE(uv_dosage, cell, thread, initialize, p)
{
  cphase_state_t *c = &(p->cphase);
  if (initialize)
    {
     p->user[0] = 0.;
     uv_intensity_0 = C_DO(cell,thread);
     x0=p->state.pos[0];
     y00=p->state.pos[1];
     z0=p->state.pos[2];
    }

  else
    {
     p->user[0] += P_DT(p) * .5 * (uv_intensity_0 + C_DO(cell,thread));
     uv_intensity_0 = C_DO(cell,thread);
    }
}

DEFINE_DPM_OUTPUT(uv_output, header, fp, p, thread, plane)
{

char name[100];


if (header)
        {
    fuv = fopen(fileuv,"w");
        if (NNULLP(thread))
```

```
            {
            fprintf(fuv,"(%s %d)\n",thread->head->dpm_summary.sort_file_name,14);
            }
            else
        fprintf(fuv,"(%s %d)\n",plane->sort_file_name,14);
        fprintf(fuv,"(%10s %10s  %10s  %10s  %10s  %10s  %10s"
               " %10s  %10s  %10s  %10s %10s  %10s  %10s %s)\n",
                "X0","Y0","Z0",
                "X","Y","Z","U","V","W","diameter","T","mass-flow",
                "time","UV-Dosage","name");
     fclose(fuv);
        }
else
        {
      fuv = fopen(fileuv,"a");
         sprintf(name,"%s:%d",p->injection->name,p->part_id);
      fprintf(fuv,
            "((%10.6g  %10.6g  %10.6g  %10.6g  %10.6g  %10.6g  "
            "%10.6g  %10.6g  %10.6g  %10.6g %10.6g %10.6g  %10.6g %10.6g) %s)\n",
            x0,y00,z0,
            p->state.pos[0], p->state.pos[1], p->state.pos[2],
            p->state.V[0], p->state.V[1], p->state.V[2],
            p->state.diam, p->state.temp, p->flow_rate, p->state.time,
            p->user[0], name);
      fclose(fuv);
    }
}
```

APPENDIX D – Tracer tests results

Experimental conditions #1	
Flow (L/h)	240
NaCl mass (g)	60
Initial conductivity in storage tank (μS/cm)	1994
Background conductivity (μS/cm)	456

#	Time (s)	Measured conductivity (μS/cm)	NaCl conductivity (μS/cm)	NaCl concentration (mg/L)	θ	E(θ)	F
0	0	456	0	-5.56	0.00	0.00	-0.01
1	10	456	0	-5.56	0.15	0.00	-0.01
2	20	456	0	-5.56	0.30	0.00	-0.01
3	30	456	0	-5.56	0.45	0.00	-0.01
4	40	456	0	-5.56	0.60	0.08	-0.01
5	50	474	18	3.40	0.75	2.68	0.00
6	60	1094	638	311.80	0.90	1.51	0.41
7	70	1442	986	484.91	1.05	0.80	0.64
8	80	1627	1171	576.93	1.20	0.69	0.76
9	90	1787	1331	656.52	1.35	0.34	0.87
10	100	1865	1409	695.32	1.51	0.18	0.92
11	110	1907	1451	716.21	1.66	0.12	0.94
12	120	1934	1478	729.64	1.81	0.09	0.96
13	130	1955	1499	740.09	1.96	0.04	0.98
14	140	1964	1508	744.57	2.11	0.02	0.98
15	150	1969	1513	747.05	2.26	0.02	0.98
16	160	1973	1517	749.04	2.41	0.01	0.99
17	170	1976	1520	750.54	2.56	0.00	0.99
18	180	1976	1520	750.54	2.71	0.02	0.99
19	190	1981	1525	753.02	2.86	0.00	0.99
20	200	1982	1526	753.52	3.01	0.01	0.99
21	210	1984	1528	754.52	3.16	0.00	0.99
22	220	1984	1528	754.52	3.31	0.00	0.99
23	230	1985	1529	755.01	3.46	0.00	1.00
24	240	1985	1529	755.01	3.61	0.00	1.00
25	250	1986	1530	755.51	3.76	0.00	1.00
26	260	1986	1530	755.51	3.91	0.00	1.00
27	270	1986	1530	755.51	4.06	0.00	1.00
28	280	1987	1531	756.01	4.21	0.00	1.00
29	290	1987	1531	756.01	4.37	0.00	1.00
30	300	1987	1531	756.01	4.52	0.00	1.00

31	310	1987	1531	756.01	4.67	0.00	1.00
32	320	1988	1532	756.51	4.82	0.00	1.00
33	330	1988	1532	756.51	4.97	0.00	1.00
34	340	1988	1532	756.51	5.12	0.00	1.00
35	350	1989	1533	757.00	5.27	0.00	1.00
36	360	1990	1534	757.50	5.42	0.00	1.00
37	370	1990	1534	757.50	5.57	0.00	1.00
38	380	1991	1535	758.00	5.72	0.00	1.00
39	390	1990	1534	757.50	5.87	0.00	1.00
40	400	1991	1535	758.00	6.02	0.00	1.00
41	410	1990	1534	757.50	6.17	0.00	1.00
42	420	1991	1535	758.00	6.32	0.00	1.00
43	430	1992	1536	758.50	6.47	0.00	1.00
44	440	1992	1536	758.50	6.62	0.00	1.00
45	450	1992	1536	758.50	6.77	0.00	1.00
46	460	1992	1536	758.50	6.92	0.00	1.00
47	470	1992	1536	758.50	7.07	0.00	1.00
48	480	1992	1536	758.50	7.23	0.00	1.00

Experimental conditions #2	
Flow (L/h)	120
NaCl mass (g)	60
Initial conductivity in storage tank (µS/cm)	1992
Background conductivity (µS/cm)	467

#	**Time (s)**	**Measured conductivity (µS/cm)**	**NaCl conductivity (µS/cm)**	**NaCl concentration (mg/L)**	θ	**E(θ)**	**F**
0	0	467	0	-5.6	0.00	-0.07	-0.01
1	10	455	-12	-11.5	0.11	0.01	-0.02
2	20	457	-10	-10.5	0.21	-0.02	-0.01
3	30	454	-13	-12.0	0.32	0.01	-0.02
4	40	455	-12	-11.5	0.43	0.00	-0.02
5	50	455	-12	-11.5	0.53	0.62	-0.02
6	60	557	90	39.2	0.64	3.32	0.05
7	70	1103	636	310.8	0.75	1.26	0.41
8	80	1311	844	414.3	0.86	0.78	0.55
9	90	1440	973	478.4	0.96	0.66	0.63
10	100	1549	1082	532.7	1.07	0.36	0.70
11	110	1609	1142	562.5	1.18	0.27	0.74
12	120	1653	1186	584.4	1.28	0.29	0.77
13	130	1701	1234	608.3	1.39	0.18	0.80
14	140	1730	1263	622.7	1.50	0.20	0.82
15	150	1763	1296	639.1	1.60	0.17	0.84
16	160	1791	1324	653.0	1.71	0.14	0.86
17	170	1814	1347	664.5	1.82	0.18	0.88

18	180	1844	1377	679.4	1.92	0.15	0.90
19	190	1868	1401	691.3	2.03	0.12	0.91
20	200	1887	1420	700.8	2.14	0.11	0.93
21	210	1905	1438	709.7	2.25	0.16	0.94
22	220	1931	1464	722.7	2.35	0.12	0.95
23	230	1950	1483	732.1	2.46	0.07	0.97
24	240	1962	1495	738.1	2.57	0.09	0.98
25	250	1977	1510	745.6	2.67	0.07	0.98
26	260	1988	1521	751.0	2.78	0.07	0.99
27	270	2000	1533	757.0	2.89	0.00	1.00
28	280	2000	1533	757.0	2.99	0.00	1.00
29	290	2000	1533	757.0	3.10	0.00	1.00
30	300	2000	1533	757.0	3.21	0.00	1.00
31	310	2000	1533	757.0	3.32	0.00	1.00
32	320	2000	1533	757.0	3.42	0.00	1.00
33	330	2000	1533	757.0	3.53	0.00	1.00
34	340	2000	1533	757.0	3.64	0.00	1.00
35	350	2000	1533	757.0	3.74	0.00	1.00
36	360	2000	1533	757.0	3.85	0.00	1.00
37	370	2000	1533	757.0	3.96	0.00	1.00
38	380	2000	1533	757.0	4.06	0.00	1.00
39	390	2000	1533	757.0	4.17	0.00	1.00
40	400	2000	1533	757.0	4.28	0.00	1.00
41	410	2000	1533	757.0	4.38	0.00	1.00
42	420	2000	1533	757.0	4.49	0.00	1.00
43	430	2000	1533	757.0	4.60	0.00	1.00
44	440	2000	1533	757.0	4.71	0.00	1.00
45	450	2000	1533	757.0	4.81	0.00	1.00
46	460	2000	1533	757.0	4.92	0.00	1.00
47	470	2000	1533	757.0	5.03	0.00	1.00
48	480	2000	1533	757.0	5.13	0.00	1.00

Experimental conditions #3

Flow (L/h)	60
NaCl mass (g)	60
Initial conductivity in storage tank (µS/cm)	2230
Background conductivity (µS/cm)	456

#	Time (s)	Measured conductivity (µS/cm)	NaCl conductivity (µS/cm)	NaCl concentration (mg/L)	θ	E(θ)	F
0	0	486	30	9.4	0.0	-0.3	0.01
1	10	456	0	-5.6	0.1	0.0	-0.01
2	20	455	-1	-6.1	0.1	0.0	-0.01
3	30	455	-1	-6.1	0.2	0.0	-0.01
4	40	456	0	-5.6	0.2	0.0	-0.01

5	50	454	-2	-6.6	0.3	0.0	-0.01
6	60	455	-1	-6.1	0.3	0.0	-0.01
7	70	456	0	-5.6	0.4	0.0	-0.01
8	80	455	-1	-6.1	0.4	0.0	-0.01
9	90	454	-2	-6.6	0.5	1.6	-0.01
10	100	604	148	68.1	0.5	1.4	0.08
11	110	733	277	132.2	0.6	2.1	0.16
12	120	922	466	226.2	0.6	1.3	0.27
13	130	1041	585	285.4	0.7	1.4	0.34
14	140	1170	714	349.6	0.8	0.9	0.41
15	150	1253	797	390.9	0.8	0.9	0.46
16	160	1333	877	430.7	0.9	0.8	0.51
17	170	1411	955	469.5	0.9	0.6	0.55
18	180	1466	1010	496.8	1.0	0.5	0.58
19	190	1513	1057	520.2	1.0	0.6	0.61
20	200	1566	1110	546.6	1.1	0.5	0.64
21	210	1616	1160	571.5	1.1	0.4	0.67
22	220	1649	1193	587.9	1.2	0.6	0.69
23	230	1705	1249	615.7	1.2	0.5	0.72
24	240	1755	1299	640.6	1.3	0.4	0.75
25	250	1793	1337	659.5	1.3	0.5	0.77
26	260	1837	1381	681.4	1.4	0.5	0.80
27	270	1879	1423	702.3	1.5	0.3	0.82
28	280	1908	1452	716.7	1.5	0.2	0.84
29	290	1926	1470	725.7	1.6	0.3	0.85
30	300	1955	1499	740.1	1.6	0.2	0.87
31	310	1974	1518	749.5	1.7	0.3	0.88
32	320	1998	1542	761.5	1.7	0.2	0.89
33	330	2020	1564	772.4	1.8	0.2	0.91
34	340	2040	1584	782.4	1.8	0.1	0.92
35	350	2050	1594	787.3	1.9	0.1	0.92
36	360	2060	1604	792.3	1.9	0.2	0.93
37	370	2080	1624	802.3	2.0	0.1	0.94
38	380	2090	1634	807.2	2.0	0.1	0.95
39	390	2100	1644	812.2	2.1	0.1	0.95
40	400	2110	1654	817.2	2.2	0.1	0.96
41	410	2120	1664	822.2	2.2	0.1	0.96
42	420	2130	1674	827.1	2.3	0.1	0.97
43	430	2140	1684	832.1	2.3	0.1	0.98
44	440	2150	1694	837.1	2.4	0.3	0.98
45	450	2180	1724	852.0	2.4	-0.2	1.00
46	460	2160	1704	842.1	2.5	0.2	0.99
47	470	2180	1724	852.0	2.5	0.0	1.00
48	480	2180	1724	852.0	2.6	0.0	1.00

APPENDIX E – Tank-in-series calculations

High Flow Rate (240 L/h)

Line 1					Line 2					Total		
θ	E	E1	F	F1	θ	E	E2	F	F2	E	F	SSE
0	-	-	0	0	0	0	0	0	0	-	0	0
0.02	0.98	0.06	0.02	0.00	0.18	0.01	0.01	0.00	0.00	0.07	0.00	0.00
0.04	0.96	0.06	0.04	0.00	0.36	0.19	0.18	0.01	0.01	0.24	0.02	0.00
0.06	0.94	0.06	0.06	0.00	0.54	0.64	0.60	0.09	0.08	0.65	0.08	0.01
0.08	0.92	0.06	0.08	0.00	0.71	1.02	0.96	0.24	0.22	1.02	0.23	0.05
0.11	0.90	0.05	0.10	0.01	0.89	1.12	1.05	0.43	0.41	1.11	0.41	0.17
0.13	0.88	0.05	0.12	0.01	1.07	0.96	0.90	0.62	0.58	0.95	0.59	0.03
0.15	0.86	0.05	0.14	0.01	1.25	0.69	0.65	0.77	0.72	0.70	0.73	0.01
0.17	0.84	0.05	0.16	0.01	1.43	0.44	0.42	0.87	0.82	0.47	0.83	0.00
0.19	0.83	0.05	0.17	0.01	1.61	0.26	0.24	0.93	0.88	0.29	0.89	0.00
0.21	0.81	0.05	0.19	0.01	1.79	0.14	0.13	0.97	0.91	0.18	0.92	0.00
0.23	0.79	0.05	0.21	0.01	1.96	0.07	0.07	0.98	0.92	0.11	0.94	0.00
0.25	0.78	0.05	0.22	0.01	2.14	0.03	0.03	0.99	0.93	0.08	0.95	0.00
0.28	0.76	0.05	0.24	0.01	2.32	0.02	0.01	1.00	0.94	0.06	0.95	0.00
0.30	0.74	0.04	0.26	0.02	2.50	0.01	0.01	1.00	0.94	0.05	0.95	0.00
0.32	0.73	0.04	0.27	0.02	2.68	0.00	0.00	1.00	0.94	0.05	0.96	0.00
0.34	0.71	0.04	0.29	0.02	2.86	0.00	0.00	1.00	0.94	0.04	0.96	0.00
0.36	0.70	0.04	0.30	0.02	3.04	0.00	0.00	1.00	0.94	0.04	0.96	0.00
0.38	0.68	0.04	0.32	0.02	3.21	0.00	0.00	1.00	0.94	0.04	0.96	0.00
0.40	0.67	0.04	0.33	0.02	3.39	0.00	0.00	1.00	0.94	0.04	0.96	0.00
0.42	0.65	0.04	0.35	0.02	3.57	0.00	0.00	1.00	0.94	0.04	0.96	0.00
0.44	0.64	0.04	0.36	0.02	3.75	0.00	0.00	1.00	0.94	0.04	0.96	0.00
0.47	0.63	0.04	0.37	0.02	3.93	0.00	0.00	1.00	0.94	0.04	0.96	0.00
0.49	0.61	0.04	0.39	0.02	4.11	0.00	0.00	1.00	0.94	0.04	0.96	0.00
0.51	0.60	0.04	0.40	0.02	4.28	0.00	0.00	1.00	0.94	0.04	0.96	0.00
0.53	0.59	0.04	0.41	0.02	4.46	0.00	0.00	1.00	0.94	0.04	0.96	0.00
0.55	0.58	0.03	0.42	0.03	4.64	0.00	0.00	1.00	0.94	0.03	0.97	0.00
0.57	0.56	0.03	0.44	0.03	4.82	0.00	0.00	1.00	0.94	0.03	0.97	0.00
0.59	0.55	0.03	0.45	0.03	5.00	0.00	0.00	1.00	0.94	0.03	0.97	0.00
0.61	0.54	0.03	0.46	0.03	5.18	0.00	0.00	1.00	0.94	0.03	0.97	0.00
0.63	0.53	0.03	0.47	0.03	5.36	0.00	0.00	1.00	0.94	0.03	0.97	0.00
0.66	0.52	0.03	0.48	0.03	5.53	0.00	0.00	1.00	0.94	0.03	0.97	0.00
0.68	0.51	0.03	0.49	0.03	5.71	0.00	0.00	1.00	0.94	0.03	0.97	0.00
0.70	0.50	0.03	0.50	0.03	5.89	0.00	0.00	1.00	0.94	0.03	0.97	0.00
0.72	0.49	0.03	0.51	0.03	6.07	0.00	0.00	1.00	0.94	0.03	0.97	0.00
0.74	0.48	0.03	0.52	0.03	6.25	0.00	0.00	1.00	0.94	0.03	0.97	0.00
0.76	0.47	0.03	0.53	0.03	6.43	0.00	0.00	1.00	0.94	0.03	0.97	0.00
0.78	0.46	0.03	0.54	0.03	6.61	0.00	0.00	1.00	0.94	0.03	0.97	0.00

0.80	0.45	0.03	0.55	0.03	6.78	0.00	0.00	1.00	0.94	0.03	0.97	0.00
0.83	0.44	0.03	0.56	0.03	6.96	0.00	0.00	1.00	0.94	0.03	0.97	0.00
0.85	0.43	0.03	0.57	0.03	7.14	0.00	0.00	1.00	0.94	0.03	0.97	0.00
0.87	0.42	0.03	0.58	0.03	7.32	0.00	0.00	1.00	0.94	0.03	0.97	0.00
0.89	0.41	0.02	0.59	0.04	7.50	0.00	0.00	1.00	0.94	0.02	0.98	0.00
0.91	0.40	0.02	0.60	0.04	7.68	0.00	0.00	1.00	0.94	0.02	0.98	0.00
0.93	0.39	0.02	0.61	0.04	7.86	0.00	0.00	1.00	0.94	0.02	0.98	0.00
0.95	0.39	0.02	0.61	0.04	8.03	0.00	0.00	1.00	0.94	0.02	0.98	0.00
0.97	0.38	0.02	0.62	0.04	8.21	0.00	0.00	1.00	0.94	0.02	0.98	0.00
0.99	0.37	0.02	0.63	0.04	8.39	0.00	0.00	1.00	0.94	0.02	0.98	0.00
1.02	0.36	0.02	0.64	0.04	8.57	0.00	0.00	1.00	0.94	0.02	0.98	0.00

Medium Flow Rate (120 L/h)

Line 1					**Line 2**					**Total**		
θ	E	E1	F	F1	θ	E	E2	F	F2	E	F	SSE
0.00	-	-	0.00	0.00	0.00	0.00	0.00	0.00	0.00	-	0.00	0.00
0.05	0.96	0.17	0.04	0.01	0.12	0.00	0.00	0.00	0.00	0.17	0.01	0.00
0.09	0.91	0.16	0.09	0.02	0.24	0.04	0.03	0.00	0.00	0.19	0.02	0.00
0.14	0.87	0.15	0.13	0.02	0.35	0.19	0.16	0.01	0.01	0.31	0.03	0.00
0.18	0.83	0.14	0.17	0.03	0.47	0.46	0.38	0.05	0.04	0.53	0.07	0.01
0.23	0.80	0.14	0.20	0.04	0.59	0.77	0.64	0.12	0.10	0.78	0.14	0.02
0.28	0.76	0.13	0.24	0.04	0.71	1.01	0.84	0.23	0.19	0.97	0.23	0.03
0.32	0.73	0.13	0.27	0.05	0.82	1.12	0.93	0.36	0.30	1.05	0.34	0.00
0.37	0.69	0.12	0.31	0.05	0.94	1.09	0.90	0.49	0.40	1.02	0.46	0.01
0.41	0.66	0.11	0.34	0.06	1.06	0.97	0.80	0.61	0.50	0.92	0.56	0.00
0.46	0.63	0.11	0.37	0.06	1.18	0.80	0.66	0.72	0.59	0.77	0.66	0.00
0.50	0.60	0.10	0.40	0.07	1.30	0.62	0.52	0.80	0.66	0.62	0.73	0.00
0.55	0.58	0.10	0.42	0.07	1.41	0.46	0.38	0.86	0.71	0.48	0.79	0.00
0.60	0.55	0.10	0.45	0.08	1.53	0.33	0.27	0.91	0.75	0.37	0.83	0.00
0.64	0.53	0.09	0.47	0.08	1.65	0.22	0.18	0.94	0.78	0.28	0.86	0.00
0.69	0.50	0.09	0.50	0.09	1.77	0.15	0.12	0.96	0.80	0.21	0.88	0.00
0.73	0.48	0.08	0.52	0.09	1.88	0.10	0.08	0.98	0.81	0.16	0.90	0.00
0.78	0.46	0.08	0.54	0.09	2.00	0.06	0.05	0.99	0.82	0.13	0.91	0.00
0.83	0.44	0.08	0.56	0.10	2.12	0.04	0.03	0.99	0.82	0.11	0.92	0.00
0.87	0.42	0.07	0.58	0.10	2.24	0.02	0.02	1.00	0.82	0.09	0.92	0.00
0.92	0.40	0.07	0.60	0.10	2.36	0.01	0.01	1.00	0.82	0.08	0.93	0.00
0.96	0.38	0.07	0.62	0.11	2.47	0.01	0.01	1.00	0.83	0.07	0.93	0.00
1.01	0.36	0.06	0.64	0.11	2.59	0.00	0.00	1.00	0.83	0.07	0.94	0.00
1.05	0.35	0.06	0.65	0.11	2.71	0.00	0.00	1.00	0.83	0.06	0.94	0.00
1.10	0.33	0.06	0.67	0.12	2.83	0.00	0.00	1.00	0.83	0.06	0.94	0.00
1.15	0.32	0.06	0.68	0.12	2.94	0.00	0.00	1.00	0.83	0.06	0.94	0.00
1.19	0.30	0.05	0.70	0.12	3.06	0.00	0.00	1.00	0.83	0.05	0.95	0.00
1.24	0.29	0.05	0.71	0.12	3.18	0.00	0.00	1.00	0.83	0.05	0.95	0.00
1.28	0.28	0.05	0.72	0.13	3.30	0.00	0.00	1.00	0.83	0.05	0.95	0.00
1.33	0.26	0.05	0.74	0.13	3.42	0.00	0.00	1.00	0.83	0.05	0.95	0.00
1.38	0.25	0.04	0.75	0.13	3.53	0.00	0.00	1.00	0.83	0.04	0.96	0.00
1.42	0.24	0.04	0.76	0.13	3.65	0.00	0.00	1.00	0.83	0.04	0.96	0.00
1.47	0.23	0.04	0.77	0.13	3.77	0.00	0.00	1.00	0.83	0.04	0.96	0.00

1.51	0.22	0.04	0.78	0.14	3.89	0.00	0.00	1.00	0.83	0.04	0.96	0.00
1.56	0.21	0.04	0.79	0.14	4.00	0.00	0.00	1.00	0.83	0.04	0.96	0.00
1.60	0.20	0.03	0.80	0.14	4.12	0.00	0.00	1.00	0.83	0.03	0.97	0.00
1.65	0.19	0.03	0.81	0.14	4.24	0.00	0.00	1.00	0.83	0.03	0.97	0.00
1.70	0.18	0.03	0.82	0.14	4.36	0.00	0.00	1.00	0.83	0.03	0.97	0.00
1.74	0.18	0.03	0.82	0.14	4.48	0.00	0.00	1.00	0.83	0.03	0.97	0.00
1.79	0.17	0.03	0.83	0.14	4.59	0.00	0.00	1.00	0.83	0.03	0.97	0.00
1.83	0.16	0.03	0.84	0.15	4.71	0.00	0.00	1.00	0.83	0.03	0.97	0.00
1.88	0.15	0.03	0.85	0.15	4.83	0.00	0.00	1.00	0.83	0.03	0.97	0.00
1.93	0.15	0.03	0.85	0.15	4.95	0.00	0.00	1.00	0.83	0.03	0.97	0.00
1.97	0.14	0.02	0.86	0.15	5.06	0.00	0.00	1.00	0.83	0.02	0.98	0.00
2.02	0.13	0.02	0.87	0.15	5.18	0.00	0.00	1.00	0.83	0.02	0.98	0.00
2.06	0.13	0.02	0.87	0.15	5.30	0.00	0.00	1.00	0.83	0.02	0.98	0.00
2.11	0.12	0.02	0.88	0.15	5.42	0.00	0.00	1.00	0.83	0.02	0.98	0.00
2.15	0.12	0.02	0.88	0.15	5.54	0.00	0.00	1.00	0.83	0.02	0.98	0.00
2.20	0.11	0.02	0.89	0.15	5.65	0.00	0.00	1.00	0.83	0.02	0.98	0.00

Low Flow Rate (60 L/h)

		Line 1					**Line 2**				**Total**	
θ	E	E1	F	F1	θ	E	E2	F	F2	E	F	SSE
0.00	-	-	0.00	0.00	0.00	0.00	0.00	0.00	0.00	-	0.00	0.00
0.02	0.98	0.16	0.02	0.00	0.06	0.00	0.00	0.00	0.00	0.16	0.00	0.00
0.04	0.96	0.16	0.04	0.01	0.12	0.00	0.00	0.00	0.00	0.16	0.01	0.00
0.07	0.94	0.16	0.06	0.01	0.18	0.01	0.01	0.00	0.00	0.17	0.01	0.00
0.09	0.91	0.15	0.09	0.01	0.24	0.04	0.03	0.00	0.00	0.19	0.02	0.00
0.11	0.89	0.15	0.11	0.02	0.30	0.10	0.08	0.01	0.00	0.23	0.02	0.00
0.13	0.87	0.15	0.13	0.02	0.36	0.19	0.16	0.01	0.01	0.31	0.03	0.00
0.16	0.86	0.14	0.14	0.02	0.41	0.32	0.27	0.03	0.02	0.41	0.05	0.00
0.18	0.84	0.14	0.16	0.03	0.47	0.47	0.39	0.05	0.04	0.53	0.07	0.01
0.20	0.82	0.14	0.18	0.03	0.53	0.63	0.52	0.08	0.07	0.66	0.10	0.01
0.22	0.80	0.13	0.20	0.03	0.59	0.78	0.65	0.13	0.11	0.78	0.14	0.00
0.25	0.78	0.13	0.22	0.04	0.65	0.91	0.76	0.18	0.15	0.89	0.18	0.00
0.27	0.77	0.13	0.23	0.04	0.71	1.02	0.85	0.23	0.19	0.98	0.23	0.00
0.29	0.75	0.13	0.25	0.04	0.77	1.09	0.90	0.30	0.25	1.03	0.29	0.00
0.31	0.73	0.12	0.27	0.05	0.83	1.12	0.93	0.36	0.30	1.06	0.35	0.00
0.33	0.72	0.12	0.28	0.05	0.89	1.12	0.93	0.43	0.36	1.05	0.40	0.00
0.36	0.70	0.12	0.30	0.05	0.95	1.09	0.91	0.49	0.41	1.02	0.46	0.00
0.38	0.68	0.12	0.32	0.05	1.01	1.04	0.86	0.56	0.46	0.98	0.52	0.00
0.40	0.67	0.11	0.33	0.06	1.07	0.96	0.80	0.62	0.51	0.91	0.57	0.00
0.42	0.65	0.11	0.35	0.06	1.13	0.88	0.73	0.67	0.56	0.84	0.62	0.00
0.45	0.64	0.11	0.36	0.06	1.18	0.79	0.66	0.72	0.60	0.77	0.66	0.00
0.47	0.63	0.11	0.37	0.06	1.24	0.70	0.58	0.77	0.64	0.69	0.70	0.00
0.49	0.61	0.10	0.39	0.07	1.30	0.61	0.51	0.80	0.67	0.61	0.73	0.00
0.51	0.60	0.10	0.40	0.07	1.36	0.53	0.44	0.84	0.70	0.54	0.76	0.00
0.53	0.59	0.10	0.41	0.07	1.42	0.45	0.37	0.87	0.72	0.47	0.79	0.00
0.56	0.57	0.10	0.43	0.07	1.48	0.38	0.32	0.89	0.74	0.41	0.81	0.00
0.58	0.56	0.09	0.44	0.07	1.54	0.32	0.26	0.91	0.76	0.36	0.83	0.00
0.60	0.55	0.09	0.45	0.08	1.60	0.26	0.22	0.93	0.77	0.31	0.85	0.00

0.62	0.54	0.09	0.46	0.08	1.66	0.22	0.18	0.94	0.78	0.27	0.86	0.00
0.65	0.52	0.09	0.48	0.08	1.72	0.18	0.15	0.95	0.79	0.23	0.87	0.00
0.67	0.51	0.09	0.49	0.08	1.78	0.14	0.12	0.96	0.80	0.21	0.88	0.00
0.69	0.50	0.08	0.50	0.08	1.84	0.11	0.10	0.97	0.81	0.18	0.89	0.00
0.71	0.49	0.08	0.51	0.09	1.90	0.09	0.08	0.98	0.81	0.16	0.90	0.00
0.74	0.48	0.08	0.52	0.09	1.95	0.07	0.06	0.98	0.82	0.14	0.90	0.00
0.76	0.47	0.08	0.53	0.09	2.01	0.06	0.05	0.99	0.82	0.13	0.91	0.00
0.78	0.46	0.08	0.54	0.09	2.07	0.05	0.04	0.99	0.82	0.11	0.91	0.00
0.80	0.45	0.08	0.55	0.09	2.13	0.04	0.03	0.99	0.82	0.11	0.92	0.00
0.82	0.44	0.07	0.56	0.09	2.19	0.03	0.02	0.99	0.83	0.10	0.92	0.00
0.85	0.43	0.07	0.57	0.10	2.25	0.02	0.02	1.00	0.83	0.09	0.92	0.00
0.87	0.42	0.07	0.58	0.10	2.31	0.02	0.01	1.00	0.83	0.08	0.93	0.00
0.89	0.41	0.07	0.59	0.10	2.37	0.01	0.01	1.00	0.83	0.08	0.93	0.00
0.91	0.40	0.07	0.60	0.10	2.43	0.01	0.01	1.00	0.83	0.08	0.93	0.00
0.94	0.39	0.07	0.61	0.10	2.49	0.01	0.01	1.00	0.83	0.07	0.93	0.00
0.96	0.38	0.06	0.62	0.10	2.55	0.01	0.00	1.00	0.83	0.07	0.93	0.00
0.98	0.38	0.06	0.62	0.11	2.61	0.00	0.00	1.00	0.83	0.07	0.94	0.00
1.00	0.37	0.06	0.63	0.11	2.67	0.00	0.00	1.00	0.83	0.06	0.94	0.00
1.03	0.36	0.06	0.64	0.11	2.72	0.00	0.00	1.00	0.83	0.06	0.94	0.00
1.05	0.35	0.06	0.65	0.11	2.78	0.00	0.00	1.00	0.83	0.06	0.94	0.00
1.07	0.34	0.06	0.66	0.11	2.84	0.00	0.00	1.00	0.83	0.06	0.94	0.00

APPENDIX F – ANSYS FLUENT F curve simulation

FLUENT								
High			Medium			Low		
t (min)	t' (min)	F	t (min)	t' (min)	F	t (min)	t' (min)	F
0.0	-0.3	0.00E+00	0.0	-0.3	0.00E+00	0.0	-0.3	0.00E+00
0.2	-0.1	1.22E-13	0.3	0.0	2.08E-18	0.3	0.0	0.00E+00
0.3	0.1	3.46E-09	0.5	0.3	4.49E-18	0.5	0.3	0.00E+00
0.5	0.3	7.23E-06	0.8	0.5	1.04E-12	0.8	0.5	0.00E+00
0.7	0.4	8.67E-04	1.0	0.8	1.31E-08	1.0	0.8	2.05E-29
0.8	0.6	1.68E-02	1.3	1.0	8.26E-06	1.3	1.0	1.01E-23
1.0	0.8	9.95E-02	1.5	1.3	6.27E-04	1.5	1.3	4.37E-19
1.2	0.9	2.80E-01	1.8	1.5	1.09E-02	1.8	1.5	2.55E-15
1.3	1.1	5.05E-01	2.0	1.8	6.41E-02	2.0	1.8	2.91E-12
1.5	1.3	6.97E-01	2.3	2.0	1.92E-01	2.3	2.0	8.68E-10
1.7	1.4	8.27E-01	2.5	2.3	3.75E-01	2.5	2.3	8.58E-08
1.8	1.6	9.03E-01	2.8	2.5	5.61E-01	2.8	2.5	3.39E-06
2.0	1.8	9.46E-01	3.0	2.8	7.12E-01	3.0	2.8	6.11E-05
2.2	1.9	9.69E-01	3.3	3.0	8.17E-01	3.3	3.0	6.09E-04
2.3	2.1	9.83E-01	3.5	3.3	8.85E-01	3.5	3.3	3.72E-03
2.5	2.3	9.90E-01	3.8	3.5	9.27E-01	3.8	3.5	1.47E-02
2.7	2.4	9.95E-01	4.0	3.8	9.53E-01	4.0	3.8	4.12E-02
2.8	2.6	9.98E-01	4.3	4.0	9.69E-01	4.3	4.0	9.03E-02
3.0	2.8	1.00E+00	4.5	4.3	9.79E-01	4.5	4.3	1.64E-01
3.2	3.0	1.00E+00	4.8	4.5	9.86E-01	4.8	4.5	2.58E-01
3.3	3.1	1.00E+00	5.0	4.8	9.90E-01	5.0	4.8	3.62E-01
3.5	3.3	1.00E+00	5.3	5.0	9.93E-01	5.3	5.0	4.68E-01
3.7	3.5	1.00E+00	5.5	5.3	9.95E-01	5.5	5.3	5.66E-01
			5.8	5.5	9.97E-01	5.8	5.5	6.53E-01
			6.0	5.8	9.98E-01	6.0	5.8	7.25E-01
			6.3	6.0	9.99E-01	6.3	6.0	7.84E-01
			6.5	6.3	9.99E-01	6.5	6.3	8.31E-01
			6.8	6.5	1.00E+00	6.8	6.5	8.67E-01
			7.0	6.8	1.00E+00	7.0	6.8	8.96E-01
			7.3	7.1	1.00E+00	7.3	7.0	9.18E-01
			7.5	7.3	1.00E+00	7.5	7.3	9.35E-01
			7.8	7.6	1.00E+00	7.8	7.5	9.49E-01
			8.0	7.8	1.00E+00	8.0	7.8	9.60E-01
						8.3	8.0	9.68E-01
						8.5	8.3	9.74E-01
						8.8	8.5	9.80E-01

9.0	8.8	9.84E-01
9.3	9.0	9.87E-01
9.5	9.3	9.90E-01
9.8	9.5	9.92E-01
10.0	9.8	9.94E-01
10.3	10.0	9.95E-01
10.5	10.3	9.97E-01
10.8	10.5	9.98E-01
11.0	10.8	9.98E-01
11.3	11.0	9.99E-01
11.5	11.3	9.99E-01
11.8	11.5	1.00E+00
12.0	11.8	1.00E+00
12.3	12.1	1.00E+00
12.5	12.3	1.00E+00
12.8	12.6	1.00E+00
13.0	12.8	1.00E+00
13.3	13.1	1.00E+00
13.5	13.3	1.00E+00
13.8	13.6	1.00E+00

FLUENT PT

	High			**Medium**			**Low**	
t (min)	**t’ (min)**	**F**	**t (min)**	**t’ (min)**	**F**	**t (min)**	**t’ (min)**	**F**
0.77	0.52	0.00E+00	1.51	1.26	0.00E+00	2.92	2.67	0.00E+00
0.85	0.60	3.79E-02	1.67	1.42	5.29E-02	3.96	3.71	3.23E-01
0.93	0.68	9.41E-02	1.84	1.59	1.38E-01	5.00	4.75	5.76E-01
1.01	0.76	2.01E-01	2.00	1.75	2.48E-01	6.04	5.79	7.53E-01
1.09	0.84	2.99E-01	2.17	1.92	3.59E-01	7.08	6.83	8.54E-01
1.17	0.92	3.94E-01	2.33	2.08	4.39E-01	8.12	7.87	9.07E-01
1.25	1.00	4.90E-01	2.50	2.25	5.29E-01	9.16	8.91	9.47E-01
1.33	1.08	5.77E-01	2.66	2.41	6.03E-01	10.20	9.95	9.69E-01
1.41	1.16	6.44E-01	2.83	2.58	6.66E-01	11.24	10.99	9.80E-01
1.49	1.24	7.08E-01	2.99	2.74	7.29E-01	12.28	12.03	9.86E-01
1.57	1.32	7.63E-01	3.15	2.90	7.71E-01	13.32	13.07	9.90E-01
1.65	1.40	8.07E-01	3.32	3.07	8.11E-01	14.36	14.11	9.93E-01
1.73	1.48	8.40E-01	3.48	3.23	8.41E-01	15.40	15.15	9.95E-01
1.81	1.56	8.64E-01	3.65	3.40	8.60E-01	16.44	16.19	9.95E-01
1.89	1.64	8.82E-01	3.81	3.56	8.81E-01	17.48	17.23	9.95E-01
1.97	1.72	8.97E-01	3.98	3.73	8.99E-01	18.52	18.27	9.95E-01
2.05	1.80	9.12E-01	4.14	3.89	9.10E-01	19.55	19.30	9.96E-01
2.13	1.88	9.23E-01	4.31	4.06	9.21E-01	20.59	20.34	9.96E-01
2.21	1.96	9.29E-01	4.47	4.22	9.32E-01	21.63	21.38	9.97E-01
2.29	2.04	9.37E-01	4.63	4.38	9.41E-01	22.67	22.42	9.97E-01
2.37	2.12	9.42E-01	4.80	4.55	9.48E-01	23.71	23.46	9.97E-01
2.45	2.20	9.48E-01	4.96	4.71	9.58E-01	24.75	24.50	9.97E-01
2.53	2.28	9.55E-01	5.13	4.88	9.59E-01	25.79	25.54	9.97E-01
2.61	2.36	9.58E-01	5.29	5.04	9.64E-01	26.83	26.58	9.97E-01
2.69	2.44	9.65E-01	5.46	5.21	9.68E-01	27.87	27.62	9.97E-01
2.77	2.52	9.68E-01	5.62	5.37	9.72E-01	28.91	28.66	9.97E-01
2.85	2.60	9.70E-01	5.78	5.53	9.75E-01	29.95	29.70	9.97E-01
2.93	2.68	9.74E-01	5.95	5.70	9.76E-01	30.99	30.74	9.97E-01

3.01	2.76	9.75E-01	6.11	5.86	9.77E-01	32.03	31.78	9.97E-01
3.09	2.84	9.77E-01	6.28	6.03	9.78E-01	33.07	32.82	9.97E-01
3.17	2.92	9.78E-01	6.44	6.19	9.82E-01	34.11	33.86	9.97E-01
3.25	3.00	9.80E-01	6.61	6.36	9.82E-01	35.15	34.90	9.97E-01
3.33	3.08	9.81E-01	6.77	6.52	9.84E-01	36.19	35.94	9.97E-01
3.41	3.16	9.84E-01	6.94	6.69	9.85E-01	37.22	36.97	9.97E-01
3.49	3.24	9.85E-01	7.10	6.85	9.85E-01	38.26	38.01	9.97E-01
3.57	3.32	9.86E-01	7.26	7.01	9.85E-01	39.30	39.05	9.98E-01
3.65	3.40	9.88E-01	7.43	7.18	9.86E-01	40.34	40.09	9.99E-01
3.73	3.48	9.89E-01	7.59	7.34	9.87E-01	41.38	41.13	9.99E-01
3.81	3.56	9.89E-01	7.76	7.51	9.87E-01	42.42	42.17	9.99E-01
3.89	3.64	9.90E-01	7.92	7.67	9.88E-01	43.46	43.21	9.99E-01
3.97	3.72	9.92E-01	8.09	7.84	9.90E-01	44.50	44.25	9.99E-01
4.05	3.80	9.92E-01	8.25	8.00	9.90E-01	45.54	45.29	9.99E-01
4.13	3.88	9.92E-01	8.41	8.16	9.90E-01	46.58	46.33	9.99E-01
4.21	3.96	9.92E-01	8.58	8.33	9.91E-01	47.62	47.37	9.99E-01
4.29	4.04	9.92E-01	8.74	8.49	9.92E-01	48.66	48.41	9.99E-01
4.37	4.12	9.92E-01	8.91	8.66	9.92E-01	49.70	49.45	9.99E-01
4.45	4.20	9.92E-01	9.07	8.82	9.93E-01	50.74	50.49	9.99E-01
4.53	4.28	9.93E-01	9.24	8.99	9.93E-01	51.78	51.53	9.99E-01
4.61	4.36	9.93E-01	9.40	9.15	9.93E-01	52.82	52.57	9.99E-01
4.69	4.44	9.93E-01	9.57	9.32	9.93E-01	53.86	53.61	9.99E-01
4.77	4.52	9.94E-01	9.73	9.48	9.94E-01	54.89	54.64	9.99E-01
4.85	4.60	9.94E-01	9.89	9.64	9.95E-01	55.93	55.68	9.99E-01
4.93	4.68	9.95E-01	10.06	9.81	9.95E-01	56.97	56.72	9.99E-01
5.01	4.76	9.95E-01	10.22	9.97	9.95E-01	58.01	57.76	9.99E-01
5.09	4.84	9.95E-01	10.39	10.14	9.95E-01	59.05	58.80	9.99E-01
5.17	4.92	9.95E-01	10.55	10.30	9.95E-01	60.09	59.84	9.99E-01
5.25	5.00	9.95E-01	10.72	10.47	9.95E-01	61.13	60.88	9.99E-01
5.33	5.08	9.95E-01	10.88	10.63	9.95E-01	62.17	61.92	9.99E-01
5.41	5.16	9.95E-01	11.04	10.79	9.95E-01	63.21	62.96	9.99E-01
5.49	5.24	9.95E-01	11.21	10.96	9.95E-01	64.25	64.00	9.99E-01
5.57	5.32	9.96E-01	11.37	11.12	9.95E-01	65.29	65.04	9.99E-01
5.65	5.40	9.96E-01	11.54	11.29	9.95E-01	66.33	66.08	9.99E-01
5.73	5.48	9.96E-01	11.70	11.45	9.95E-01	67.37	67.12	9.99E-01
5.81	5.56	9.96E-01	11.87	11.62	9.95E-01	68.41	68.16	9.99E-01
5.89	5.64	9.97E-01	12.03	11.78	9.95E-01	69.45	69.20	9.99E-01
5.97	5.72	9.97E-01	12.20	11.95	9.95E-01	70.49	70.24	9.99E-01
6.05	5.80	9.97E-01	12.36	12.11	9.95E-01	71.52	71.27	9.99E-01
6.13	5.88	9.98E-01	12.52	12.27	9.95E-01	72.56	72.31	9.99E-01
6.21	5.96	9.98E-01	12.69	12.44	9.95E-01	73.60	73.35	9.99E-01
6.29	6.04	9.98E-01	12.85	12.60	9.96E-01	74.64	74.39	9.99E-01
6.37	6.12	9.98E-01	13.02	12.77	9.96E-01	75.68	75.43	9.99E-01
6.45	6.20	9.98E-01	13.18	12.93	9.96E-01	76.72	76.47	9.99E-01
6.53	6.28	9.98E-01	13.35	13.10	9.96E-01	77.76	77.51	9.99E-01
6.61	6.36	9.98E-01	13.51	13.26	9.96E-01	78.80	78.55	9.99E-01
6.69	6.44	9.98E-01	13.67	13.42	9.96E-01	79.84	79.59	9.99E-01
6.77	6.52	9.98E-01	13.84	13.59	9.96E-01	80.88	80.63	9.99E-01
6.85	6.60	9.99E-01	14.00	13.75	9.96E-01	81.92	81.67	9.99E-01
6.93	6.68	9.99E-01	14.17	13.92	9.96E-01	82.96	82.71	9.99E-01
7.01	6.76	9.99E-01	14.33	14.08	9.97E-01	84.00	83.75	9.99E-01
7.09	6.84	9.99E-01	14.50	14.25	9.97E-01	85.04	84.79	9.99E-01
7.17	6.92	9.99E-01	14.66	14.41	9.97E-01	86.08	85.83	9.99E-01
7.25	7.00	9.99E-01	14.83	14.58	9.97E-01	87.12	86.87	9.99E-01
7.33	7.08	9.99E-01	14.99	14.74	9.97E-01	88.16	87.91	9.99E-01
7.41	7.16	9.99E-01	15.15	14.90	9.97E-01	89.19	88.94	9.99E-01
7.49	7.24	9.99E-01	15.32	15.07	9.97E-01	90.23	89.98	9.99E-01

7.57	7.32	9.99E-01	15.48	15.23	9.97E-01	91.27	91.02	9.99E-01
7.65	7.40	9.99E-01	15.65	15.40	9.98E-01	92.31	92.06	9.99E-01
7.73	7.48	9.99E-01	15.81	15.56	9.98E-01	93.35	93.10	9.99E-01
7.81	7.56	9.99E-01	15.98	15.73	9.99E-01	94.39	94.14	9.99E-01
7.89	7.64	9.99E-01	16.14	15.89	9.99E-01	95.43	95.18	9.99E-01
7.97	7.72	9.99E-01	16.30	16.05	9.99E-01	96.47	96.22	9.99E-01
8.05	7.80	9.99E-01	16.47	16.22	9.99E-01	97.51	97.26	9.99E-01
8.13	7.88	9.99E-01	16.63	16.38	9.99E-01	98.55	98.30	9.99E-01
8.21	7.96	9.99E-01	16.80	16.55	9.99E-01	99.59	99.34	9.99E-01
8.29	8.04	9.99E-01	16.96	16.71	9.99E-01	100.63	100.38	9.99E-01
8.37	8.12	9.99E-01	17.13	16.88	9.99E-01	101.67	101.42	9.99E-01
8.45	8.20	9.99E-01	17.29	17.04	9.99E-01	102.71	102.46	9.99E-01
8.53	8.28	9.99E-01	17.46	17.21	9.99E-01	103.75	103.50	9.99E-01
8.61	8.36	9.99E-01	17.62	17.37	9.99E-01	104.79	104.54	9.99E-01
8.69	8.44	9.99E-01	17.78	17.53	9.99E-01	105.82	105.57	9.99E-01
8.77	8.52	1.00E+00	17.95	17.70	1.00E+00	106.86	106.61	1.00E+00